Addis Ababa University
አዲስ፡አበባ፡ዩኒቨርሲቲ
Seek Wisdom, Elevate your Intellect and Serve Humanity

SCHOOL OF GRADUTE STUDIES

COLLEGE OF NATURAL AND COMPUTATIONAL SCIENCES

SCHOOL OF EARTH SCIENCES

Structure of the crust beneath the Gedemsa Tectono-Magmatic Segment and its environs perceived from geologically constrained geophysical studies: an implication for geothermal heat source assessment, Central Main Ethiopian Rift, Ethiopia

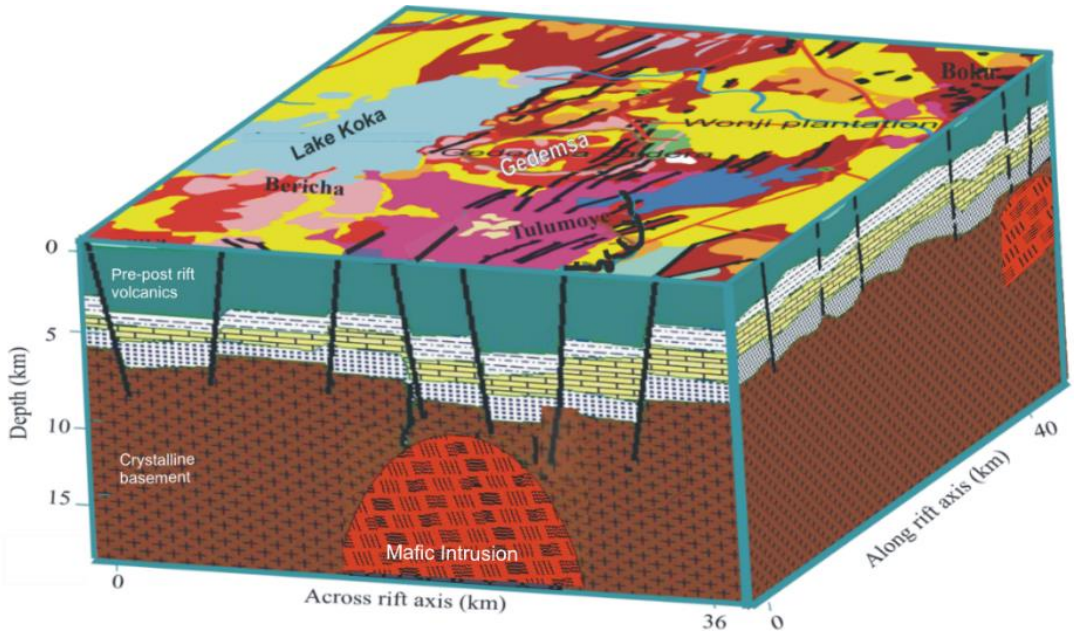

A thesis submitted to

The school of graduate studies of Addis Ababa University in partial fulfillment of the requirements for the degree of master of science in Applied Geophysics

By

Wubamlak Nigussie

Addis Ababa University

Addis Ababa-Ethiopia

August, 2020

ADDIS ABABA UNIVERSITY

SCHOOL OF GRADUATE STUDIES

SCHOOL OF EARTH SCEINCES

This is to certify that the thesis prepared by Wubamlak Nigussie, entitled: " **Structure of the crust beneath the Gedemsa tectono-magmatic segment and its environs perceived from geologically constrained geophysical studies: an implication for geothermal heat source assessment, Central Main Ethiopian Rift, Ethiopia** " and submitted in partial fulfillment of the requirements for the degree of Master of Science in Applied Geophysics complies with the regulations of the university and meets the accepted standards with respect to originality and quality.

Approved by examining committee:	Signature	Date
Dr. Balemwal Atnafu (Head, School of Earth Sciences)	_____	_____
Dr. Abera Alemu (Advisor)	_____	_____
Prof. Dereje Ayalew (Co - Advisor)	_____	_____
Prof. Tilahun Mammo (Examiner)	_____	_____
Dr. Ameha Atnafu (Examiner)	_____	_____

DECLARATION

I, the undersigned, hereby declare that the thesis entitled with "**Structure of the crust beneath the Gedemsa tectono-magmatic segment and its environs perceived from geologically constrained geophysical studies: an implication for geothermal heat source assessment, Central Main Ethiopian Rift, Ethiopia**" is my original work carried out under the supervision of Dr. Abera Alemu and Prof. Dereje Ayalew and has not been presented to any university or institution for the award of any degree or diploma program and all sources of materials used for the thesis are duly acknowledged.

Name of the candidate	Signature	Date
Wubamlak Nigussie	_____	_____

This is to certify that the above declaration made by the candidate is correct to the best of our knowledge and it has been submitted for examination with our approval as university advisors.

Advisors name	Signature	Date
Dr. Abera Alemu (Advisor)	_____	_____
Prof. Dereje Ayalew (Co-Advisor)	_____	_____

ABSTRACT

The Main Ethiopian Rift is in a stage of tectono-magmatic segmentation where the mechanism of rifting is primarily enhanced by a magmatic addition to the crust. However, the extent, nature and structure of the crust beneath each magmatic segment and occurrence of the associated geothermal resources remain unclear. Geologically constrained gravity and magnetic studies have been conducted in the Gedemsa tectono-magmatic segment and its environs.

Interpretation of combined potential field data in this study have provided important contributions regarding the geodynamic setting, crustal structure and geothermal resources of the study area. 2D gravity modelling of the entire crust across and along the Gedemsa tectono-magmatic segment reveals three density layers (upper volcanics/sediments, upper crust with intrusion, and lower crust) overlying the upper mantle with underplating beneath the Ethiopian plateau. The along axis tectono-magmatic segmentation and the bilateral off rift volcanic zones revealed by gravity data show the distribution of deformation beyond the rift axis and the complex geodynamic setting of the central to northern Main Ethiopian Rift transition zone.

Gravity modelling of the upper crust show the occurrence of intrusions with an estimated depth range of 10-20 km and 5-10 km beneath the Tulumoye-Gedemsa and Boku Volcanic complexes respectively. This magmatic addition to the crust is attributed to be an ongoing dyke intrusion which induces surface fracturing/faulting. The gravity data reveals that at deeper depths the Gedemsa tectono-magmatic segment (25 km wide and 60 km long) is elongated parallel to the Main Ethiopian Rift axis and changes its orientation oblique to the rift axis at the near surface.

A detailed investigation of the structure of the shallow crust based on 2D gravity models, 3D geologic interpretation and gravity/magnetic maps offer the presence of promiceable thermal heat sources (as shallow magma chambers at the Boku, Gedemsa and Tulumoye volcano). Quaternary faults/fractures of the Wonji Fault Belt play a triple fold role regarding the geothermal system of the area: 1) Transporting melt from the deep intrusion to shallow magma chambers. 2) Acting as pathways for the surface/groundwater migrating to the shallow magma chambers. 3) Transporting thermal fluid to the surface to be detected as thermal manifestation.

Key words: Tectono-magmatic segment, Gravity/Magnetic anomaly, Crustal structure, 2D gravity model, Geothermal heat source

ACKNOWLEDGMENT

Basically, MSc thesis is something unique in the life of academia of which one can't carry out alone. In this regard, I want to acknowledge the individuals, institutions and organizations which contributed to the completion of this thesis.

First of all, I would like to express my sincere gratitude to my supervisor Dr. Abera Alemu who makes this project possible with his fatherly approach and scientific guidance. His constructive comments, endless suggestions, and immense knowledge when writing the thesis have made me confident to independently carry out my future research (in geophysics). I do not do justice here to how important his support has been. My special thanks goes to prof. Dereje Ayalew for his advice and constructive comments.

I am very much grateful to Lingerew Nebere for his endless commitment to assist me throughout the completion of the thesis. I am also very thankful to Aklilu Teka, staff member of Reykjavik geothermal company, who coordinated and assisted my fieldwork.

How can I forget the time I spent with Professor Tilahun Mammo and Professor Tigistu Haile? Their encouragement and suggestion is invaluable for the completion of this thesis. My deepest gratitude also goes to geophysics PhD candidates of AAU specifically Kassaye Bewketu and Muluken Kassa who helped me in extracting the gravity data of BGI using MATLAB software.

Heartfelt thanks goes to my family particularly Tihunie Lamesginew for her unfailing financial and moral support throughout my academic life. I would also like to take this opportunity to thank my friends Yoseph Muhabaw, Abebe Mihret, Esubalew Yehualaw, Mahider Mulugeta and graduate geophysics students at AAU.

Finally, I am grateful in acknowledging the following institutions and organizations: Addis Ababa University (for funding the project), Reykjavik geothermal company (for suppling magnetometer, transport and camp services), International Gravimetric Bureau (for providing gravity data) and the Geological survey of Ethiopia particularly Mr. Kassahn Dander and Mr. Berhanu Bekele (for providing secondary magnetic data).

TABLE OF CONTENTS

LIST OF FIGURES

LIST OF TABLES

LIST OF ACRONYMS

AS	Analytical Signal
CMER	Central Main Ethiopian Rift
EAGLE	Ethio-Afar Geoscientific Lithospheric Experiment
EARS	East African Rift System
ED	Euler Deconvolution
GPS	Geographic positioning system
GSE	Geological survey of Ethiopia
HDR	Horizontal Derivative
IGB	International Gravimetric Bureau
IGRF	International Geomagnetic Reference Field
IGSN	International Gravity Standardization Network
IUGG	International Union of Geodesists and Geophysicists
LAB	Lithosphere-Asthenosphere Boundary
Ma	Million years ago (million)
MER	Main Ethiopian Rift
mGal	milliGal
MSL	Mean Sea Level
nT	Nano Tesla
NE–SW	North East–South West
N-E	North–East
NMER	Northern Main Ethiopian Rift
NNE	North North East

NW	North West
NW-SE	North West–South East
NNE–SSW	North North East–South South West
NNW	North–North–West
N–S	North–South
RTP	Reduction to Pole
SDZFZ	Siliti Debre Zeit Fault Zone
SE	South East
SI	Structural Index
SMER	Southern Main Ethiopian Rift
SSW	South South West
S –W	South–West
TDR	Tilt Derivative
TMS	Tectono-Magmatic Segment
WFB	Wonji Fault Belt
YTVTL	Yerer Tuluwelel Volcano-tectonic Lineament
2D	Two dimensional
3D	Three dimensional

CHAPTER ONE

INTRODUCTION

1.1 General Background

The Main Ethiopian rift (MER), an ideal natural laboratory providing an opportunity to study magmatism related to rifting, is one of the few areas worldwide where one can capture the ongoing process of continental breakup (Giday Woldegebrel et al., 1990; Wolfenden, et.al., 2004; Ebinger and Casey, 2001). It is magmatically segmented (Ebinger and Casey, 2001; Kurtz et al., 2007), seismically active (Keranen et. al., 2004) with uplifted flanks and steep border faults which attracts geoscientists with its excellent location to study how continental rifts develop into oceanic ridges. Rifting along the MER begun in Miocene (15-18 Ma) (Wolfenden et al., 2004). Its floor is characterized by well-developed Quaternary faulting mostly related to the Wonji Fault Belt (WFB) (Acocella et al., 2003; Boccaletti et al., 1999), NNE-SSW trending faults and chain of quaternary eruptive centers (Casey et al., 2006).

Previous findings from the MER help to distinguish two competing scenarios of continental rifting: Fault-driven magmatism (extension accommodated by faulting) and Magma-enhanced rifting (strain accommodated by magmatism) (Rooney, 2006 and references therein). Recent studies suggest that continental–oceanic transition in Ethiopia is manifested by a shift from broad-based to focused strain, the Quaternary division of the MER into discrete magmatic segments (Ebinger and Casey, 2001). Furthermore, Kurtz et al., 2007) propose these segments not only represent magmatic but also tectono-magmatic segmentation of the MER as a whole. Kurtz et al. (2007) reported four tectono-magmatic segments (TMSs) (Gedemsa, Boseti, Kone and Fantale) along the MER (Fig. 1.1).

Furthermore, Tomographic images (Bastow et al., 2005) reveal an along-axis segmentation in the crust and upper mantle that follows the same right-stepping pattern as that of the magmatic segments of the WFB which they interpret as discrete zones of enhanced melt production in the mantle. The role of magma intrusion and diking rather than large offset faults in the MER is manifested by elongation of eruptive centers, localization of seismicity and magmatic activity (Casey et al., 2006). There are two end member scenarios on the formation of TMSs; According to Boccaletti et al. (1999), segmentation results from change in the direction of

extension, NW-SE/orthogonal to E-W/oblique movement, of Nubia-Somalia kinematics (Fig. 1.1). However, Ebinger and Casey (2001) suggest that segments result from and are mainly controlled by the magmatic activity in a manner similar to oceanic rift processes.

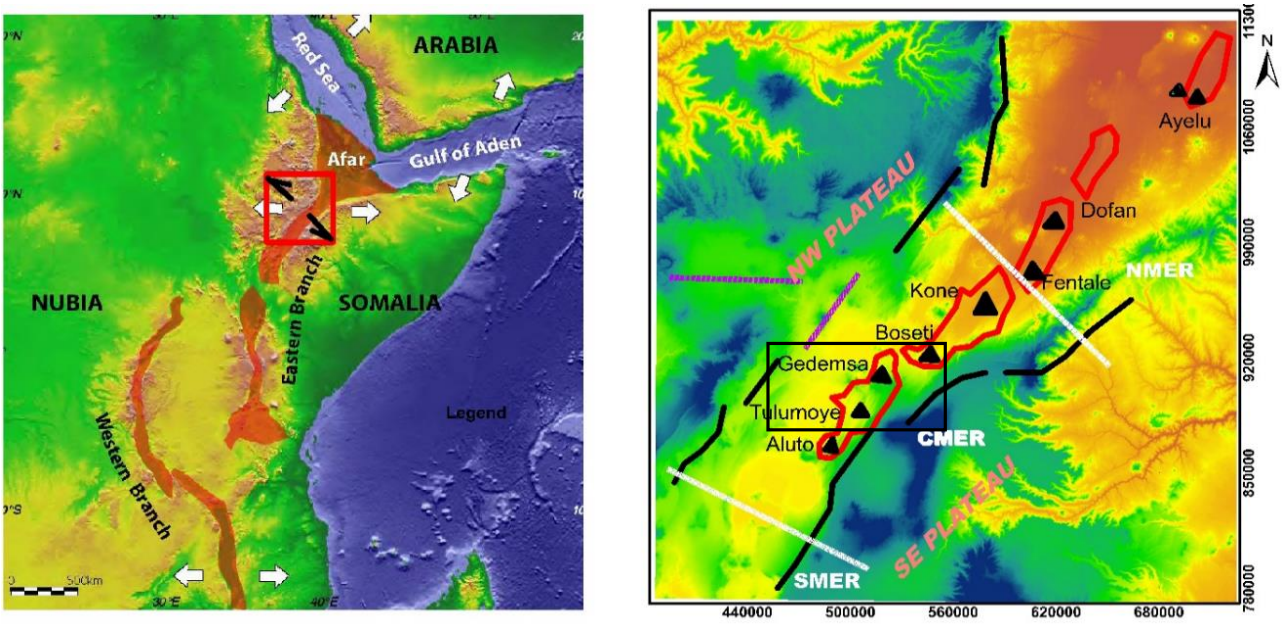

Figure 1.1 Evolution of the MER within the frame of EARS. The left panel shows a change in Nubia-Somalia kinematics from orthogonal (white arrows) to oblique extension (black arrows) (Boccaletti et al., 1998; Wolfenden et al., 2004). The right panel shows the en echelon arrangements of TMS in the MER (Ebinger and Casey, 2001). The rectangle in black line is the Gedemsa TMS and its environs (the study area).

It is apparent that magmatism and magmatic intrusion control the crustal structure in the MER (Ebinger and Casey, 2001; Casey et al., 2006). Geodetic data show that TMSs formed above or near the locus of maximum extension, accommodate 80% of the strain across the rift, indicating that border faults are no longer the locus of extension (Ebinger and Casey, 2001; Corti, 2009). Comparisons with mid ocean ridges suggests that TMSs rather than detachment faults mark the ocean-continent boundary in rifts with a ready magma supply (Bastow et al., 2005; Ebinger and Casey, 2001; Kurtz et al., 2007).

Despite numerous efforts on the evolution of the MER, "What is the role of magmatism in continental rifting"? And "What is the crustal structure in the central-northern MER"? Are the framing questions facing the 21th century geoscientists (Rooney, 2006). In this regard,

delineating Arctechiture of the subsurface beneath individual TMSs aimed at in this work is anticipated to provide a vital additional information to the existing debate.

Volcanism in these TMSs commenced about 1.6 Ma (Giday Woldegebrel et al., 1990; Boccaletti et al., 1999). More than 31 volcanoes hosting hydrothermal systems with a potential to generate large amounts of geothermal power have been reported along the MER (Greenfield et al., 2019 and references therein). A temperature of 300 ℃ within a depth of 2 km in the Gedemsa TMS reveal the presence of shallow crustal reservoir (Ebinger and Casey, 2001) and researchers and exploration companies give an attention to it. Although regional scale geophysical surveys have been reported on the overall structure of the MER, the detailed structure and magmatism of the individual TMSs remain unclear. Within this context understanding the subsurface structure using geophysical methods, which is aimed in this work, is thought to provide a scientific trend for utilization of these resources.

Geophysical techniques such as seismology, gravity and magnetics (among others) can yield much more detailed information about subsurface structures (faults, dike swarms, magma chambers and intrusions) (Telford et al., 1990). Seismic tomography arguably gives the best resolution and depth coverage. However, potential field surveys can also yield reasonably detailed structural data at typically a fraction of cost and time (Hinze et al., 2013).

In this work gravity and magnetic data from the Gedemsa TMS and adjacent areas has been processed, analyzed and interpreted to analyze the architecture of the crust beneath the TMS and its environs.

1.2 Description of the study area

1.2.1 Location, areal extent and accessibility of the study area

The study area, the Gedemsa tectono-magmatic segment and its environs, is located in Oromia regional state (Fig. 1.2) with in the central sector of the Main Ethiopian Rift about 175 km south of Addis Ababa. Geographically, it is bounded within the limit 470000-550000 E and 898000-935000 N with perimeter and areal extent of 377.05 km and 8190.06 km^2 respectively. The area can be accessed through an asphalt road along the Addis Ababa-Nazareth-Asella highway. Apart from this, minor gravel roads are available to access different part of the study area (Fig. 1.2).

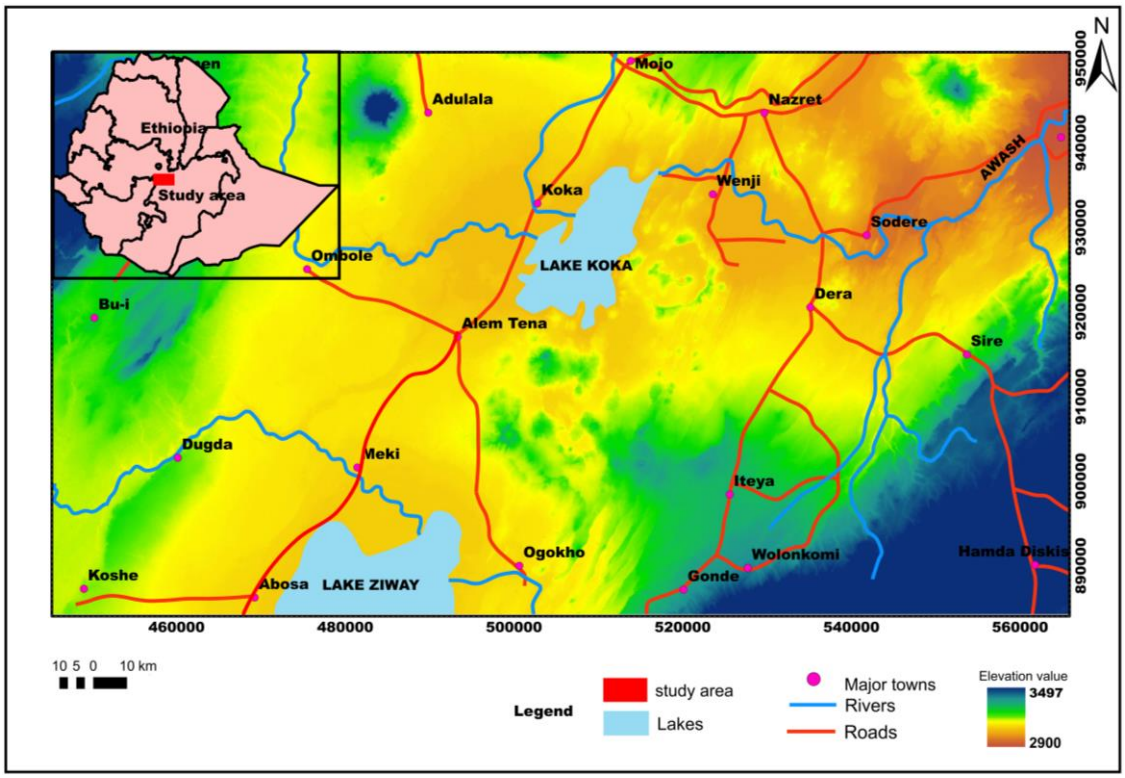

Figure 1.2 Location map of the study area (red panel in the inset map).

1.2.2 Physiography of the area

Situated within the central sector of the MER, the area is characterized by active tectonism and related volcanism (Engdawork Admasu and Selamawit Worku, 2015). The area consists of

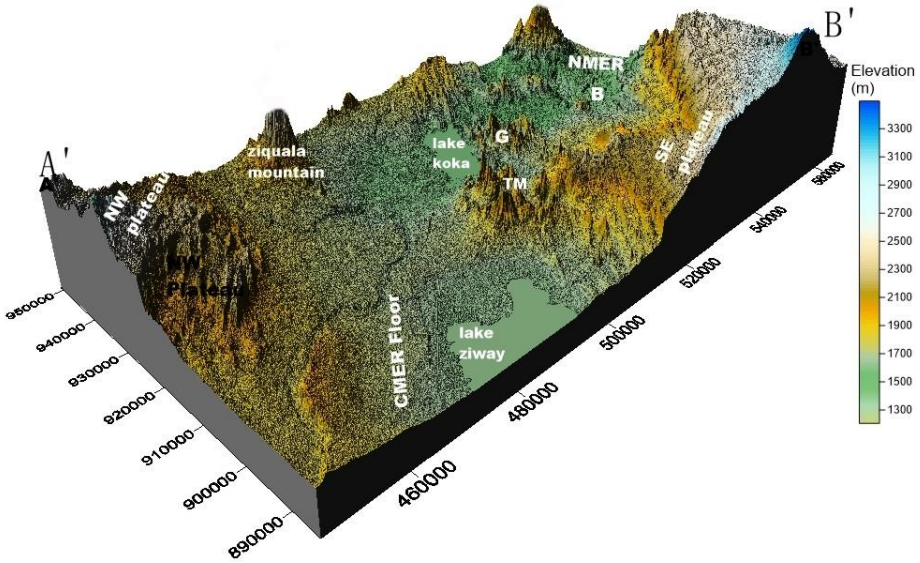

Figure 1.3 physiographic map of the area. Where B=Boseti, G=Gedemsa, TM=Tulumoye, NW=North Western, SE=South Eastern, CMR=Central MER and NMER= Northern MER.

very rugged terrain of the rift floor and the flanks of the MER (Fig. 1.3 and 1.4). Calderas (e.g. Gedemsa, Tulu), volcanic edifices and, vents dominate the area.

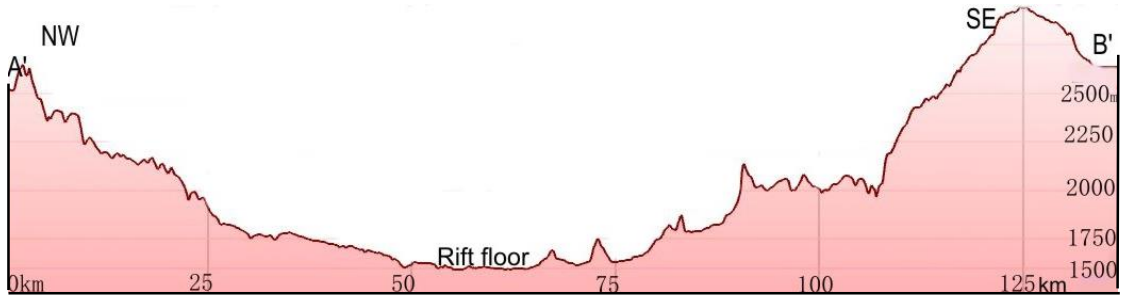

Figure 1. 4 Elevation profile of the MER across the Gedemsa TMS. Where, SE=South Eastern, NW=North Western and A'-B' is the profile line taken from the physiographic map (Fig. 1.3).

1.3 Statement of the problem

Although the crustal structure and role of magmatism in the MER remain a topic of continuing debate, it has been studied widely in terms of tectonic evolution of the rift, lithospheric and crustal structural analysis (Corti et al., 2009; Rooney, 2006). Various research efforts have been applied on the southern, central and northern segments of the MER. However, subsurface rift architecture in the Central sector remains unclear (Corti, 2009). Previous Researchers on regional wise (Bilham et al., 1999; Bastow et al., 2005; Ebinger and Casey, 2001; Casey, et al., 2006; Kurtz et al., 2007) proposed that TMSs are the locus of strain by active dyke injection in the rifting process of the MER. Furthermore, efforts from seismic, structural and geomorphologic observation indicate that the Miocene border faults are inactive and strain is localized to the 20 km-wide and 50 km long TMSs (Casey, et al., 2006). In this regard, a magmatic addition to the crust in the form of intrusion processes largely control the extension and rupture processes of the MER which magnifies the role of TMSs in the context of modeling the evolution of the MER. However, the extent, nature and structure of the crust beneath each TMSs remain poorly understood.

Geological and geophysical observation (Bekele Abebe et al., 2007; Bastow et al., 2010; Kendall et al., 2006) between 8 and 9.5°N along-rift suggests that the greatest melt supply, the likelihood volcanic eruption and geothermal potential lies between the Gedemsa and Dofan volcanoes. It is also simple to consider that, apart from the favorable geological conditions, geothermal resources in the MER are primarily controlled by rift structures (Engdawork

Admasu and Selamawit Worku, 2015). Previous geophysical studies established fundamental principles of rifting at large scale (Samrock et al. 2018). Nonetheless, regional analysis overlooks local analysis, where key geothermal structural features (shallow magma chambers, thin massive intrusion and fractures) remained relatively poorly constrained.

This study is aimed to contribute a vital geophysical component to the existing debate over crustal structure and bring out new subsurface information beneath the Gedemsa TMS along the central sector of the MER. Moreover, emphasis has been given on delineating the key concealed geothermal heat sources in the form of structural features.

1.4 Objectives

1.4.1 Main Objective:

The main target of this work is to map the structure of the crust beneath the Gedemsa tectono-magmatic segment and its environs by using geologically constrained geophysical data.

1.4.2 Specific Objectives:

This thesis aims at address the following specific objectives including:

a. Map the subsurface geological structures beneath the Gedemsa TMS and its environs.
b. Suggest the possible heat sources (intrusions, vents or shallow magma chambers) for the geothermal system beneath the Gedemsa TMS.
c. Outline the extent, nature and structure of the Gedemsa TMS.
d. Prepare geophysical and geological models for the entire and the upper crust beneath the study area using the compiled geophysical data constrained by the existing previous geological data.

1.5 Research questions

The following research questions are formulated to address the above objectives:

1. What kind of crustal structure exists beneath the Gedemsa TMS and its environs?
2. What is the significance of the subsurface geological structures on Geothermal resource occurrence of the area?
3. What would be the scientific justification on possible heat source of the prospective thermal fluid resource in the area?

1.6 Significance of the study

The en echelon along-axis segmentation of the MER represents the interplay between Miocene-Pliocene rift structures and localized magma intrusion zones marking the transition to seafloor spreading. Within a hope of providing new insight on evolution of the MER, understanding subsurface structure beneath each TMS which would be fairly achieved by geophysical methods is highly valuable. Gravity and magnetic data constrained by geological information reveal adequate results on subsurface structure as well as geothermal resource occurrence within the form of geologic structures. Moreover, effort is made to add new information on the gaps of previous works so as to add up scientific views. The following are among the major benefits of this research:

1. Provide adequate evidence on understanding subsurface crustal structure of the area.
2. Provide an insight on role of TMSs to the rifting process of the MER.
3. Give firsthand information on crustal structure and establish a scientifically guided trend for future regional geothermal resource exploration along the MER.
4. Upgrading once professional and scientific capability in order to carry out further detail works effectively in the areas of geothermal resource exploration which is highly contributes to the development goal of the country.

1.7 Materials and methods

1.7.1 Methods

In this study, geophysical approach in the form of gravity and magnetic methods constrained by geologic information has been conducted to clarify and detect the shallower and deeper structural tectonic setup of the Gedemsa TMS. Despite originate naturally due to gravitational or magnetic sources; non-geologic effects may result an erratic potential data. Within this regard, various data reduction and enhancement techniques (Fig. 5) have been applied to remove this unwanted noise effect. Thus, the gravity and magnetic method of prospecting with their distinct physical/mathematical foundation, data processing and interpretation techniques has been employed. Existing gravity and magnetic data with primary magnetic data were processed, analyzed and interpreted with previous geological and geophysical data as a constraint.

To address the research questions and framed objectives, the methodological approaches of this work were conducted in three phases (Fig. 5). The first phase consists of pre-field work preparation including collecting secondary data, review of previous works and preparation of organized work plan as well as maps. Secondary data were collected from different organization and institutions. The second phase is the stage of actual data collection from the proposed site. Magnetic and GPS data has been acquired on selected traverses. The final phase is the data processing, analysis and interpretation stage. After data reduction process, appropriate data enhancement techniques have been employed.

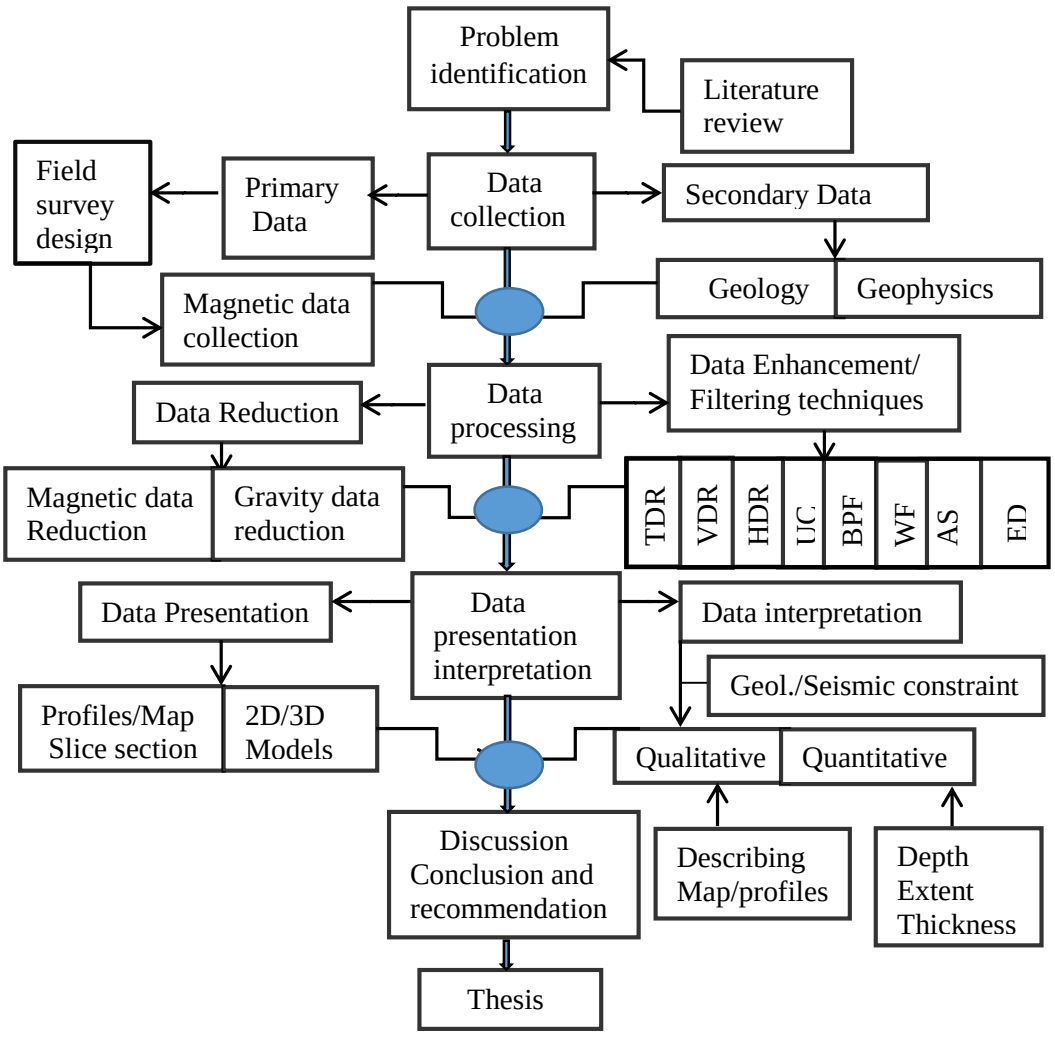

Figure 1.5 Methodological approach and work flow of the study. Abbreviations: TDR=tilt derivative, VDR=Vertical Derivative, HDR=Horizontal Derivative, UC=Upward continuations, BPF=Band Pass Filter, WF=Wave length filter, AS= Analytical signal and ED= Euler Deconvolution.

1.7.2 Materials and instruments

This thesis is a final output of an integrative use of different instruments, materials and software's. GPS and topo maps were used to determine the location (latitude, longitude and elevation) of magnetic data as well as to analyze the topographical variation of the area. Magnetic survey has been held within the help of Proton precession magnetometer. The row data becomes a scientific information with the help of basic software on potential field, oasis montaj (version 8.4), GYM SYS and supplementary software's including surfer (version 9), ARC GIS version 10.3 and CorelDRAW (Version 12).

1.8 Thesis organization

This thesis has been organized in to eight chapters of discrete contents. The first chapter gives an overview on the general framework of the research including description of the study area, rationale, objectives, methodological approach of the study, and the materials utilized.

The second chapter addresses the geophysical and geological reviews including: Geophysical evidences on crustal and lithospheric structure of the MER; A snapshot on evolution of the MER within the frame of East African Rift system; Overview on geology of the MER and the study area; Tectono-magmatic evolution of the MER; Fundamentals on geothermal energy and the case for this hidden treasures with in the MER with an emphasis on Tulumoye-Gedemsa geothermal prospect. In the third chapter, theoretical and mathematical foundations of the methods of the study are discussed.

Data acquisition, processing and presentation techniques adopted for the study are discussed in chapter four. The result of this study is presented in the fifth chapter of the thesis. It focuses on qualitative interpretation of gravity and magnetic anomaly maps with their enhanced components. Chapter six presents more of quantitative interpretation through modelling of the gravity data just to translate the vertical discontinuity of the geophysical signal in to geology.

The seventh chapter addresses the discussion and implication part of the present study. Finally, conclusions and recommendations based on the results and findings of the study are addressed in chapter eight.

CHAPTER TWO

GEOPHYSICAL AND GEOLOGICAL REVIEWS

2.1 Geophysical evidences on Crustal and lithospheric structure of the MER

The Main Ethiopian Rift (MER) has focused the attention of many research teams and a large geological and geophysical new datasets has been acquired in recent years. As a result, our knowledge of the rift structure, evolution and interactions between magmatism has been improved (Corti, 2009). Various geophysical techniques (tomography, receiver function analysis, seismic refraction and reflection, gravity and magnetotellurics) have been employed in the MER aiming at examining the process of continental breakup (Rooney, 2006).

2.1.1 Lithospheric structure of the main Ethiopian rift

Lithospheric mantle thins as rifting process thins the continental crust (Rooney, 2006) and the MER is an actual locale of this process. Ethio-Afar geoscientific lithospheric experiment (EAGLE), have provided a wealth of information on the lithospheric structure of the region (Keranen et al., 2004; Bastow et al., 2005; Cornwell et al., 2006; Maguire et al., 2006; Whaler and Hautot, 2006).

Dugda et al. (2007) reported that the lithospheric mantle beneath the MER and Afar extends to a depth of ~50 km. 3D gravity inversion by Tilahun Mammo (2013) supports the absence of lithospheric mantle in Afar but in the MER and the presence of magmatic underplating beneath the NW Ethiopian plateau. According to Lavayssière et al. (2018), there is no lithosphere asthenosphere boundary (LAB) beneath the rift to a depth of 75 km but beneath Afar. The lack of LAB phase beneath the rift suggests melt percolation through the base of the lithosphere beneath the northern most East African Rift System. Teleseismic study (Bastow et al., 2008) shows the presence of low velocity continuation of the African Superplume with an approximate width of 500 km and a depth range of 70-400 km in the MER and adjacent plateau. Upper mantle structural analysis by Bastow et al. (2005) reveals the along axis rift segmentation of the low velocity upwelling in the upper most 100 km with an offset to the side of the rift. Keranen et al. (2009) reported that the depth to Moho is about 28-40 km (Fig. 2.1b) Within the MER. However, Lithospheric imaging using receiver function by Lavayssière et al. (2018) resulted in Moho depth of 31±6 km beneath the plateau, 28±3 km beneath the MER.

2.1.2 Crustal structure of the main Ethiopian rift

Understanding rifting process of the MER requires a comprehensive view of crustal structure (Rooney, 2006). Knowledge of how the regional crustal structure has been modified during extension and volcanism in the MER is informative in dealing the processes controlling this fundamental transition. Controlled source seismic data (Maguire et al., 2003; Keranen et al., 2004; Dugda et al., 2005; Mackenzie et al., 2005; Maguire et al., 2006) provide more detailed pictures of the crust beneath the MER, assists in discriminating geodynamic models.

Along the rift sector, the crust gradually thins from 38–40 km in the SMER and CMER to 25–35 km (Fig. 2.2d) in the NMER (Dugda et al., 2005; 2007; Maguire et al., 2006; Stuart et al., 2006; Mickus et al., 2007; Keranen et al., 2009) (Fig. 5). A gravity study (Mehatsente et al., 1999; Tilahun Mammo, 2004) suggests that the lower crust is composed of mafic materials, indicative of extensional tectonics. Generally, the general physical and geological property variation of the MER along the rift axis are clearly shown in Figure 2.2a to d.

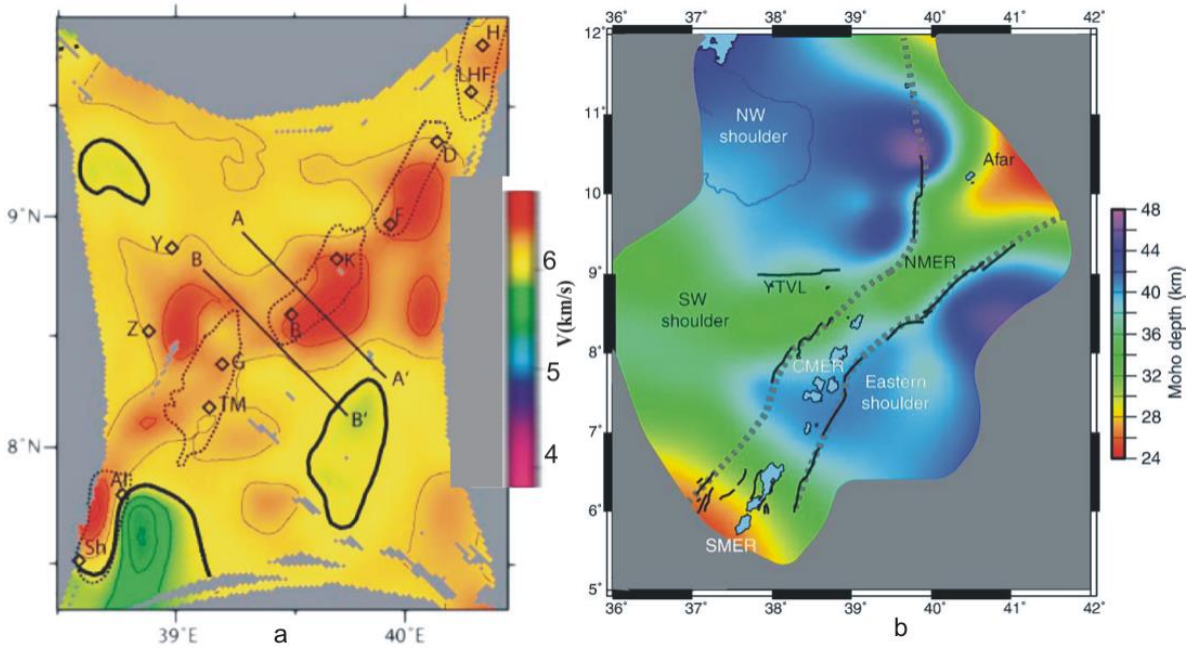

Figure 2.1 horizontal slice of VP at 10 km underlying TMSs of the MER(A). Dashed lines=TMS. Diamonds=eruptive centers: Sh=Shala; Al =Aluto; TM=Tulumoye; G=Gedemsa; B=Boseti; K=Kone; F=Fentale; D=Dofan; LHF=Liyado-Hayk field; H=Hertale. A-A' and B-B' are velocity profiles (Keranen et al., 2004). Moho depth on the MER (B) with dashed gray lines show the rift outlines and Solid black lines are the rift border faults (Keranen et al. 2009).

Shallow tomographic studies (Keranen et al., 2004; Daly et al.2008) reveal 20 km wide and 50 km-long high-velocity anomalies at depths of 5-15 km beneath both the SDFZ and WFB segmentation of the rift with distinct TMS (Fig. 2.1a). According to Daly et al. (2008), high p-wave velocity (6.5 km s^{-1}) beneath the axis of the rift at a depth of 12–25 km and high V_p/V_s ratios (1.81–1.84) at the same depth range suggest the existence of cooled mafic intrusions. This is consistent with resistivity (Whaler and Hautot, 2006), shear wave splitting, (Keir et al., 2005) and gravimetric (Cornwell et al., 2006; Mehatsente et al., 1999) results.

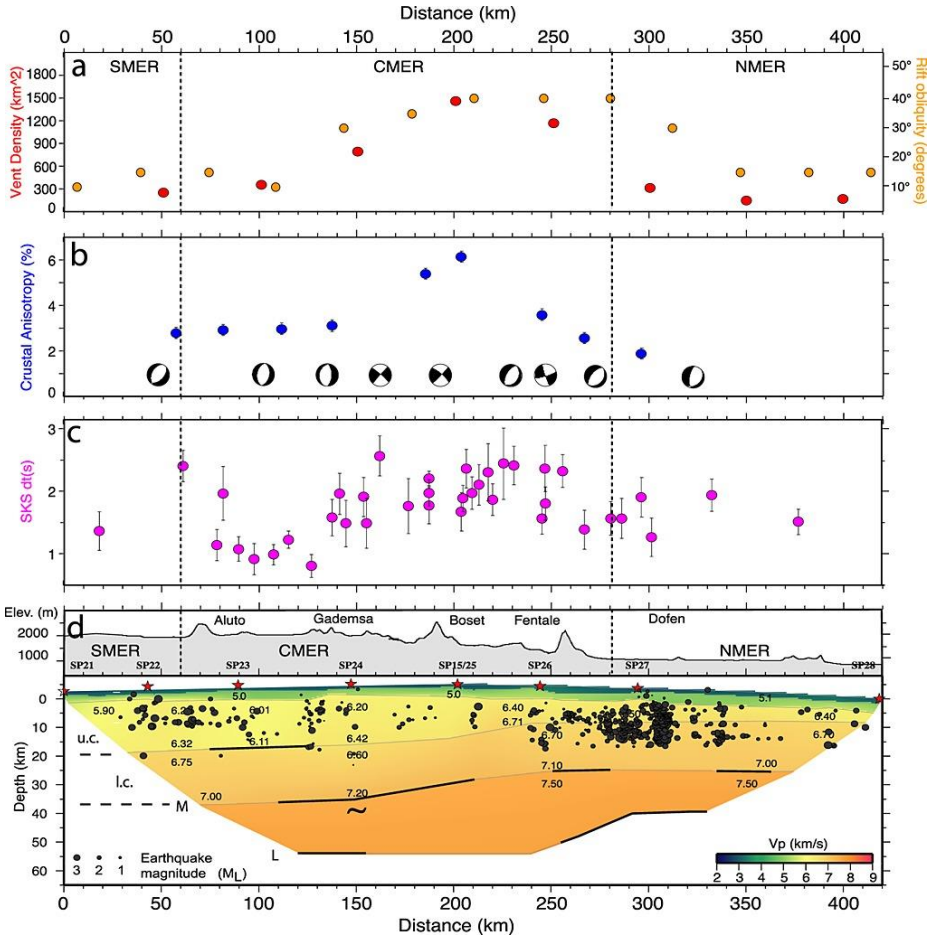

Figure 2.2 Geological and Geophysical Property variation along the axis of the MER. (a) rift obliquity-orange circles, vent density-red circles. (b) seismic anisotropy and focal mechanisms. (c) SKS splitting delay times. (d) Topographic profile (top) and P wave velocity model (bottom) (Maguire et al., 2006; Kendall et al., 2006; Keir et al., 2011a; 2011b). Labels, u.c.=upper crust, l.c.=lower crust, M=Mohorovic discontinuity, and L=mid-Lithospheric reflector. Stars=shot point location and black dots=Earthquake hypocenters.

According to Mehatsente et al. (1999), crustal thinning (31 km) coincides with the location of the intrusion beneath the rift floor. TMSs along the MER have been included in several regional gravimetric studies (Mickus et al., 2007; Mehatsente et al., 1999, Tiberi et al., 2005) and characterized by gravity maxima. Some regional Geophysical studies included Gedemsa TMS as part of their study to constrain the seismicity and crustal structure of the MER (Daly et al., 2008; Keranen et al., 2004; Maguire et al., 2006).

Gedemsa TMS lies within high-velocity 6.4 km/s at 10-km depth (Fig. 2.2d) regions defining the present day rift axis. The velocity structure within the rift showed low velocity (3.3–4.8 km/s) sediments near the surface extending to 5-km depth and P-wave velocities slightly faster than normal continental crust within the rift (6 km/s) (Fig. 2.2d). The best estimate for crustal thickness in this area of the MER is 35 km (Cornwell et al., 2010; Maguire et al., 2006) (Fig, 2.2d and 2.1b). Although the Gedemsa TMS has been included in the above regional and semi-regional studies, subsurface structures beneath the TMS remain relatively poorly constrained. This is the first study which has been conducted in a hope of imaging the subsurface of a single TMS with a combined potential field method.

2.2 Geologic and geodynamic setting

2.2.1 The East Africa rift system

Tectonic forces are the forming agents of rift systems on Continental plates of the Earth (Samrock et al., 2018). Continental Rifts provide an opportunity in shaping our planet, breaking continents apart and results in oceanic environments. Currently, the East African Rift system (EARS) (Fig. 1.1) is the most active site on Earth which captures the early stages of rifting in Tanzania to incipient oceanic spreading in Afar (Ebinger and Casey, 2001). It is a striking feature of the African continent which marks the separation of the Nubian and Somalia plates (Kendall et al., 2006).

Deep-seated mantle upwelling beneath Africa (African super plume) results in a dynamic topography (Fig. 1.1) (Kendall et al., 2006) and a site of numerous natural resources (e.g. freshwater, minerals and geothermal). Contrary to many other rifts hidden beneath our oceans, the EARS is exposed sub-areally, making it a unique locale for direct observation of the mechanisms of rifting, from continental breakup to seafloor spreading (Lavayssière, 2019). The Ethiopian rift forms the third arm of the Red Sea, Gulf of Aden rift-rift-rift triple junction

where the Arabian, Nubian, Somalian and Danakil plates join in Afar (Fig. 1.1). The Miocene-Recent EARS in Ethiopia sub-aerially exposes the transitional stage of rifting within the youngest continental flood basalt province (Bastow et al., 2005).

2.2.2 Tectono-magmatic evolution of the MER

The evolution of the MER is one of the main research topics for 21th century geoscientists (Corti, 2003). Several tectonic events affected Ethiopia prior to the Cenozoic rifting, from Precambrian collision to Mesozoic extension (Tsegaye Abebe et al., 2005 and references therein). This pre-Cenozoic history of tectonic events created pre-existing heterogeneities with variable orientation that have controlled the development of the EARS in Ethiopia (Tesfaye Korme et al., 2004). Major transversal volcano-tectonic lineaments; Yerer-Tulluwellel (YTVL) and the Goba-Bonga (Fig. 2.3a), affecting the rift and the surrounding plateaus (Tsegaye Abebe, 2014 and references therein). These lineaments mark the transition between different sectors of the MER. The MER, northern end of the EARS, accommodates 4–6 mm/yr N100°E oriented extension between Nubia and Somalia Plates (Corti et al., 2018). It is subdivided into three main sectors (Fig. 2.3a), the Southern, Central, and Northern MER, in terms of fault pattern, timing and lithospheric characteristics (Corti, 2009; Hayward and Ebinger, 1996; Giday Woldegebrel et al., 1990).

Two distinct system of normal faults affecting the MER: (1) the border faults (Fig. 2.3a) and (2) a set of faults affecting the rift floor (Fig. 2.3a) known as the Wonji Fault Belt (WFB), (Boccaletti et al., 1998). Recent volcano-tectonic activity in the MER is generally confined to the WFB (Mohr, 1962; 1967; Giday Woldegebrel et al., 1990), postulated to be tectono-magmatic segments and a precursor to a mid-ocean ridge (Ebinger and Casey, 2001). The WFB, tectono-volcanic system, characterized by relatively short, closely spaced and active faults that exhibit minor vertical throw with associated extensional fractures and grabens (Acocella et al., 2003; Boccaletti et al., 1998). They are intimately associated with intense Quaternary-Recent magmatism of the rift floor (Boccaletti et al., 1998; Ebinger and Casey, 2001). It is well expressed in the northern MER where its structures form clearly defined right-stepping en echelon segments obliquely cutting the rift floor (Ebinger and Casey, 2001). Wonji faults are primarily driven by magma intrusion triggering upward propagation of faulting and diking in to the brittle upper crust (Ebinger and Casey, 2001).

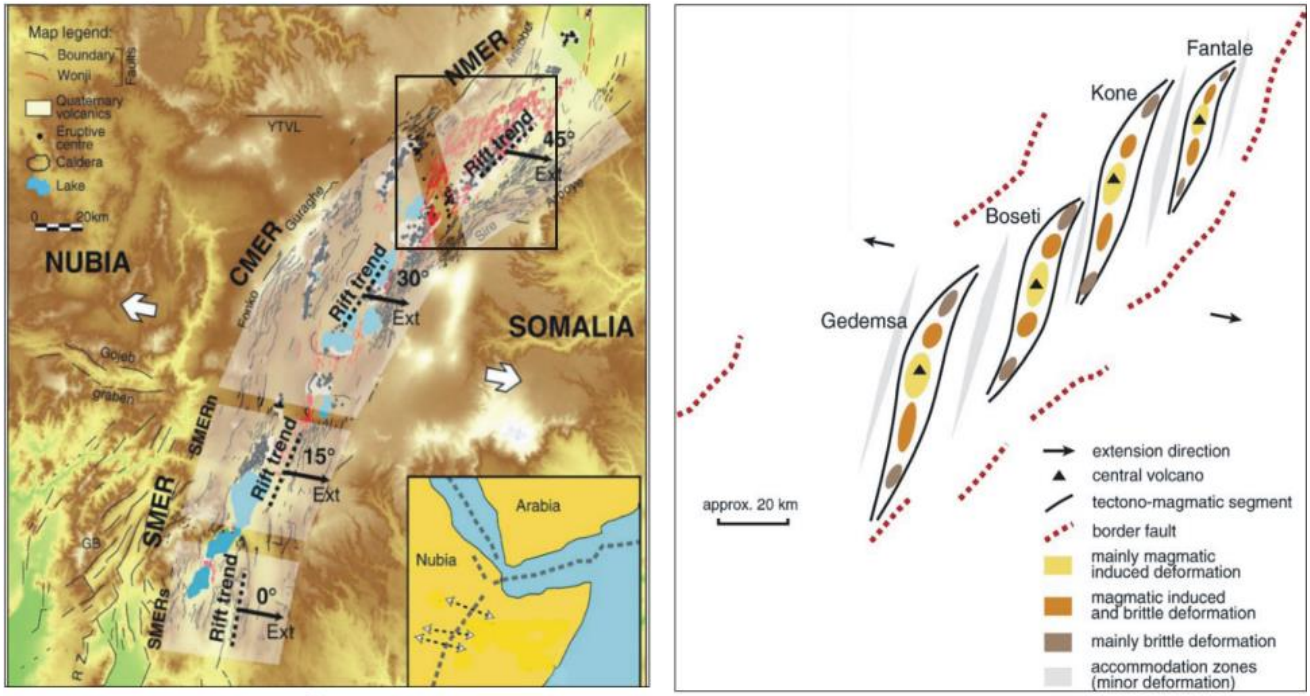

Figure 2.3 Structural setting (a) and major tectono-magmatic segments (b) of the MER. The inset (Fig. 2.3a) map shows the EARS with in the triple junction. The rectangle (Fig. 2.3a) shows the TMSs (Fig. 2.3b) of the MER (Agostini et al., 2011; Corti, 2009).

The abundance of Wonji faults decreases southward (Fig.2.3a): they are in an incipient stage of development in the CMER and negligible in the SMER (Agostini et al., 2011; Bonini et al., 1997; Corti, 2009). Geophysical findings (Keranen et al., 2004) in the central to Northern MER reveal the presence of magma throughout the lithosphere below the different fault segments. As a result, the WFB represent tectono-magmatic segmentation (Kurtz et al., 2007).

2.2.3 Major Tectono-magmatic segments of the Main Ethiopian rift

The Quaternary along-axis segmentation of faults and eruptive centers along the WFB has been reported by Ebinger and Casey (2001) and described as TMSs (Kurtz et al., 2007; Fig. 2.3b). The subsurface segmentation is revealed by tomographic (Bastow et al., 2005) and gravimetric (Tiberi et al., 2005; Cornwell et al., 2006) images with velocity and gravity highs that follows the same pattern as the surface. Each TMSs are oblique to the $N45^0$ strike Miocene border faults (Fig. 2.3a). Tomographic image of the upper crust by Keranen et al. *(*2004) reveals anomalously high-velocity material within 7-20 km depth ranges (Fig. 2.1a) beneath the magmatic segments. The along axis segmentation of the MER has been continued to be a

debating issue (Bonini et al., 1997). Wolfenden et al. (2004) proposes that the quaternary oblique deformation within the WFB is a result of a change in extension direction. Other models from geophysical (Keranen et al., 2004) and geological (Ebinger and Casey, 2001) studies linked the process to a slow spreading to oceanic ridge. Remote sensing based study by Kurtz et al. (2007) come up to a new conclusion of the segmentation of the MER is not only tectonic but also magmatic and represents tectono-magmatic segmentation. Towards the tips, the influence of diking decreases and faulting becomes dominant. 4) Domains with minor magmatic as well as brittle deformation separate the TMS.

2.2.3.1 Gedemsa tectono-magmatic segment

There is no a common consensus in naming of the Gedemsa TMS where the names Gedemsa TMS (Corti, 2009), Koka TMS (Ebinger and Casey, 2001; Wolfenden et al., 2004) and Aluto-Gedemsa TMS (Casey et al., 2006) are variably used. It is marked by numerous collapse calderas and volcanoes (Fig. 2.1a). This TMS shows only minor crustal thinning with respect to crustal thickness beneath the flanks (Stuart et al., 2006; Maguire et al., 2006; Tiberi et al., 2005). The 0.85-0.29 Ma Gedemsa caldera lies near the northern end of this TMS (Boccaletti et al.,1999). The morphologically youthful faults cut 1.97 Ma basalt flows which are overlain by a 1.6-0.6 Ma ignimbrites and Holocene flows (Pizzi et al., 2006). Individual faults within this TMS are up to 20 km in length, and bound narrow horsts and grabens.

2.2.3.2 Boseti-Kone tectono-magmatic segment

Boseti TMS is 65 km-long which steps 15 km to the east and lies about 500 m lower than the Gedemsa TMS. Morphology and seismicity patterns indicate that it is now inactive (Wolfenden et al., 2004; Keir et al., 2006). Boseti volcano lies near the southern tip of the segment, and the elongate, multiphase Kone caldera lies near its northern end (Fig. 2.3b).

2.2.3.3 Fantale-Dofan tectono-magmatic segment

Unlike the other TMS to the south, the Fantale-Dofan TMS lies within a half-graban bounded along its eastern side by a series of 60-80 m scarps. It is marked by felsic shield volcanoes with elongate calderas at both its southern (Fantale) and northern (Dofan) ends (Kurtz et al., 2007).

2.2.3.4 Angelele tectono-magmatic segment

The 60 km-long Angelele TMS has the form of a half-graben bounded on its eastern side by a 230 m-high fault system, the largest active fault in the area. Geological and geophysical information is sparse in this remote region. Faults and aligned eruptive centers do not show the right-stepping pattern of TMS to the south, perhaps owing to superposition of the MER on Oligocene Red Sea rift structures. Faults bounding the segment shows greater throws than to the south (Kurtz et al., 2007).

2.2.4 Geology of the main Ethiopian rift

Pre-rift geology of Ethiopia is composed by an extremely folded and foliated basement of pre-Cambrian rocks. Those rocks are exposed in southern MER, northern Afar and western rift escarpment of the Central MER (Fig. 2.4), overlain by Mesozoic sediments (Corti, 2009). Volcanism in Ethiopia started during the Eocene–Late Oligocene with the eruption of the Ethiopia–Yemen flood-basalt province (Trap series) (Mohr and Zanettin, 1988). This volcanic episode varies from tholeiitic to alkaline lava flows (Kieffer et al., 2004) and felsic lavas with pyroclastic rocks of rhyolitic or trachytic compositions interbedded with the flood basalts (Mohr and Zanettin, 1988).

The primary Eruption of flood basalts mostly occurred through fissures at places controlled by pre-existing weaknesses (Mohr and Zanettin, 1988; Mege and Tesfaye Korme, 2004). Most of the basalts and associated felsic rocks were apparently erupted in a rather short time interval (5 Ma.) with the greatest eruption rates occurring from 31-28 Ma (Baker et al., 1996; Hoffman et al., 1997).

A second stage of activity is Miocene in age and is characterized by the construction of huge basaltic shield volcanoes (Termaber Basalt Formation). A large number of shield volcanoes developed from 30 Ma to about 10 Ma on the surface of the volcanic plateau immediately after the peak of volcanic activity (Kieffer et al., 2004). This subsequent, less voluminous volcanic activity formed some of the highest reliefs of the plateau (e.g. Mts. Simien, and Choke) (Mohr and Zanettin, 1988; Kieffer et al., 2004).

The third stage, Pliocene-Quaternary in age, is directly related to the main phases of opening of the main Ethiopian rift and Afar (Giday Wolfenden et al., 2004). Volcanism in the MER is

dominated by per alkaline rhyolitic ignimbrites, pumice and ash-fall deposits with minor lava flows. Silicic rocks are associated with volumetrically subordinate basaltic products that form cinder cones and lava flows mostly aligned along the WFB (Mohr, 1971) (Fig. 2.4). Most recent acidic products in the northern MER have been erupted from central volcanoes with large summit caldera, (Gedemsa, Kone and Fantale). Fissural eruptions of silicic rocks have been inferred, but rarely demonstrated by field studies for the lowest exposed silicic rocks forming the rift-floor ignimbrites (Di Paola, 1972; Boccaletti et al., 1999). In terms of geology, the floor of the rift valley is predominantly covered by volcanic rocks such as rhyolites, trachyte, pyroclastic falls, ignimbrites and basalts (Giday Woldegebrel et al., 1990). According to Giday Woldegebrel et al., (1990), the central sector of the MER can be classified in to six chronostratigraphic units (Table 2.1).

Table 2.1 Stratigraphy of the central MER

Absolute age			Central MER Lithology
Era	Age		
Cenozoic	Quaternary 1.6		Quaternary sediment Wonji Group
	Pliocene (5.3)		Chillalo trachyte
			Butajira ignimbrite
	Miocene	upper 11.2	----------
			Guraghe basalt
		Middle 16.6	----------
			Shebele trachyte
		Late 23.7	---------- ----------
	Oligocene	Upper 30	Kella Basalt
		Lower 36.6	---------- ----------
	Eocene		
Mesozoic	Jurassic	Upper	Variegated shale
		middle	Antalo limestone
		lower	Adigrat sandstone
Pre-Cambrian			Crystalline basement

(After Giday Woldegebrel et al., 1990).

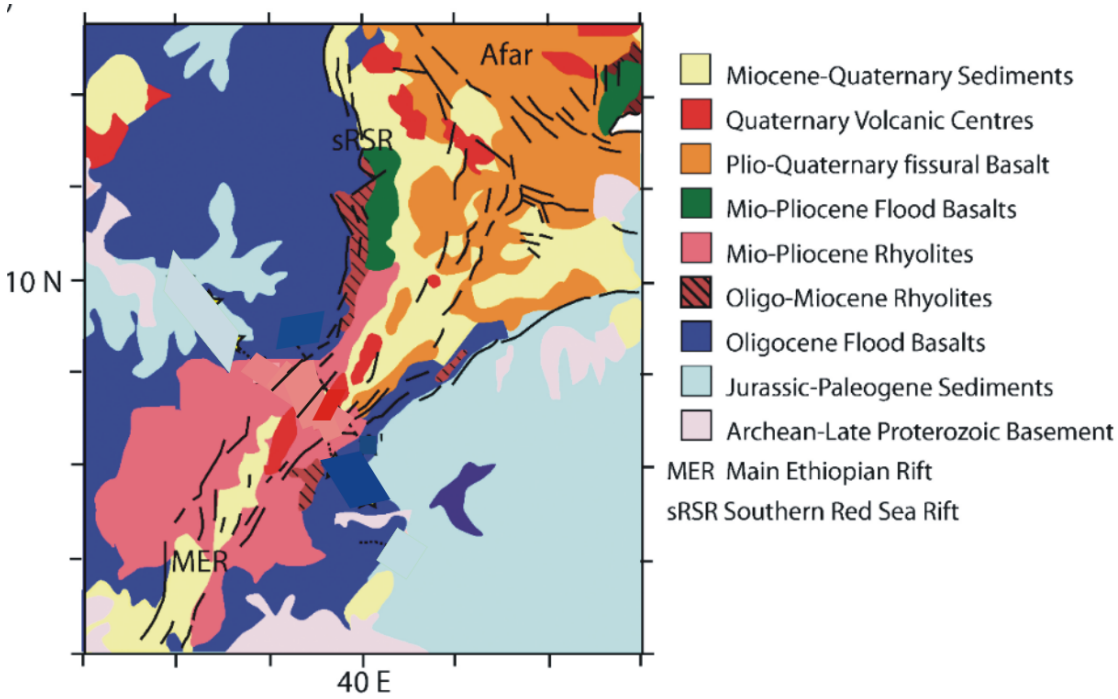

Figure 2.4 Simplified geological map of the MER and Afar region (after Wolfenden, 2003).

2.2.5 Geology of the study area

Geologically the study area is almost bare of pre-rift formations exposures and covered by rock units with syn-post rift formations (Fig. 2.5). Data from Chronological studies shows that, the rock units falls in the Pliocene to Holocene in age (Tsegaye Abebe et al., 2005). The following section addresses the geologic point of view (most of the description are adopted from Tsegaye Abebe et al. (2005) for the study area which is generalized in Figure 2.5.

2.2.5.1 Qul-alluvium cover

All forms of reworked materials of volcanic origin. alluvium, soil, fluvial, colluvium, slope scree and debris deposits occurs as caldera, creator as well as graben floor fillings with a thickness of < 0.5 m. They have been deposited since Holocene (Tsegaye Abebe et al., 2005).

2.2.5.2 Qjr-Jano rhyolites

The Jano rhyolite consists of two lithologic units: 1) vitric to sanadine phyric comenditic obsidian lava flows and domes with a maximum thickness of 100 m. 2) Porphyritic glassy black trachytic lava flows with a maximum thickness of 20 km. These formations found surrounding recent volcano, Tulumoye and are Holocene in age (Di Paola, 1972).

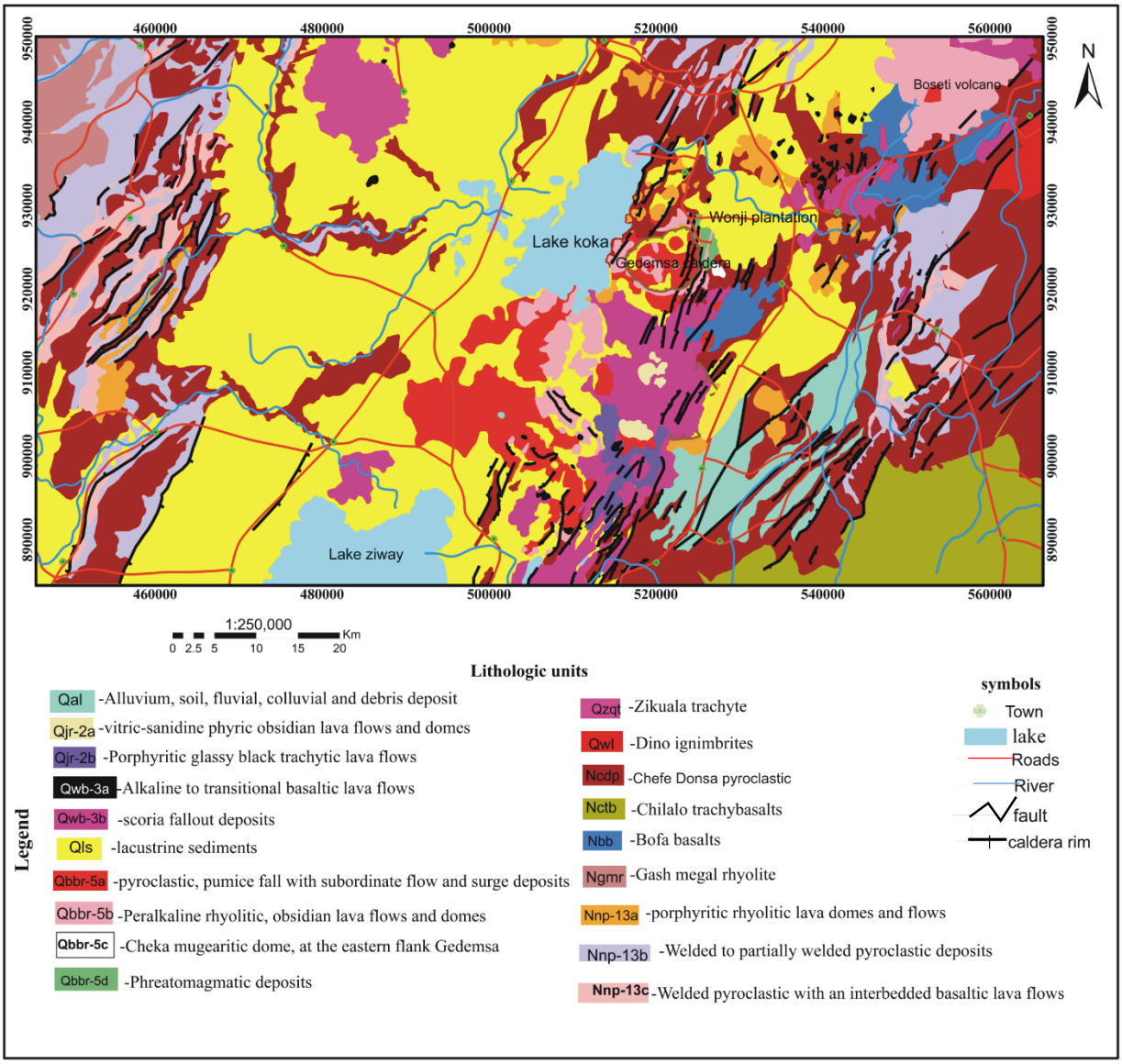

Figure 2. 5 Geological and structural map of the Gedemsa TMS and its environs (modified from Tsegaye Abebe et al., 2005).

2.2.5.3 Qwb-wonji basalts

There are three lithologic units within this formation close to the main depression of the MER associated with the oblique and en echelon structure of the WFB: 1) Alkaline to transitional basaltic lava flows outcropping along the axis of the MER (Wonji and Tulumoye) with a maximum thickness of 10m. 2) Scoria fallout deposits and 3) phreatomagmatic deposits with an age of < 0.1 Ma (Pleistocene-Holocene) (Tadiwos Chernet et al., 1998). They reach with a maximum thickness of 10 km at Tulumoye where volcanism is intense. They vary from

porphyritic to aphyric with olivine as a dominant phenocryst and composed of scoria cones fallout deposits, volcanic bombs, ropy fragments.

2.2.5.4 QLS-lacustrine sediments

Lacustrine sediments are composed of sand and silt intercalated with recent pyroclastic deposits. The major component of the sediments is volcanic origin including pumice, obsidian, rhyolite and basalt. They occur at elevation below 1900 m above msl and outcropping extensively in western part of the area (along the Awash, Mojo and Meki river gorges) with a maximum estimated thickness of 30 m. They are younger than 0.5 Ma and become younger towards the rift axis (Tsegaye Abebe et al., 2005 and references therein).

2.2.5.5 Qbbr-Bora-Bericha rhyolites

Central volcanoes such as Bora-Bericha, Tulumoye and Gedemsa representing the first volcanic activity associated with the oblique fracturing of the axial rift (WFB). This formation contains four main lithologic units: 1) pyroclastic, pumice fall with subordinate flow and surge deposits, 2) Peralkaline rhyolitic, obsidian lava flows and domes, 3) Cheka mugearitic dome, at the eastern flank of Gedemsa and 4) Phreatomagmatic deposits exposed at the northeast of Gedemsa flank with a maximum thickness of 10 m. Chronologically these formations are determined to be < 0.9 Ma (Kazmin et al., 1980). Gedemsa is an 8 km caldera where pre-caldera activity gave rise to ignimbrites associated with ash flows, pumice falls and surge deposits. The post caldera products are composed of lava domes. Bora and Bericha represent two larger recent volcanic centers at the west of the Tulumoye caldera.

2.2.5.6 Qzqt-Ziquala trachyte

Includes isolated well reserved composite cone of mount Ziquala extending NW-SE at its base and SW-NE at the upper part of cone (> 3000 km). Dark grey aphyric lava flows with few interbedded pyroclastic where sanadine, anorthoclase and quartz are the dominant phenocryst in the porphyritic lavas with an age of 1.28-0.85 Ma (Tsegaye Abebe et al., 2005).

2.2.5.7 Dino ignimbrite

Dino ignimbrite is a vitric rhyolitic tuff with an accretionary lapilli tuff and it contains a

volcanic glassy texture with crystals and rocks. Fine grained fragments of alkali feldspar and pumice are the common clasts (Tsegaye Abebe et al., 2005).

2.2.5.8 NQab-alkaline basalts

This lithologic unit consists of olivine pyroxene phyric alkaline basaltic lava flows with a maximum thickness of 5 m and scoria fall-out with some pyroxene crystals. Its geological age is determined to be 2.03-0.88 Ma (Zanettin et al., 1980; Tadiwos Chernet et al., 1998).

2.2.5.9 Ncdp-Chefe Donsa pyroclastic

It includes pyroclastic overlying the Nazret pyroclastics and Bofa basalts in some localities. It consists of unwelded to poorly welded fine volcanic ash flow and fall deposit composed by mainly comenditic rhyolite with lithics, glass shards and some crystals. They are 2.24-1.77 Ma in age (Mazzarini et al., 1999) with a maximum thickness of 70 m. Some big caldera forming central volcanoes (e.g. Boku) have age ranges overlapping with this rock unit which may represent the main source for this pyroclastic product.

2.2.5.10 Nctb-Chilalo trachybasalts

This unit includes the product of Chilalo central volcano, located east of Lake Ziway on the eastern rift shoulder. The slope of the volcano has constituted by a series of thick but short lava flows varying in composition from basaltic to trachytic with an age of 2.54-1.3 Ma (Giday Woldegebrel et al., 1990).

2.2.5.11 Nbb-Bofa basalts

This unit includes tabular basaltic lava flows of the rift floor lying above Nazret pyroclastic units. Plagioclase with few olivine and pyroxene phyric and rarely fine grained to scoriaceous basaltic lava flows with a maximum thickness of 30 m. They are 2.7-1.2 Ma in age (Kazmin et al., 1980; Giday Woldegebrel et al., 1990).

2.2.5.12 Nnp-Nazret pyroclastic

This is the most widely occurred silicic unit consisting of three syn-rift distinct lithologic units: 1) The upper member consists of per alkaline pantelleritic ignimbrite varying from strongly to

poorly welded. 2) Middle sequence of rhyolitic to trachytic quartz, sanadine, orthoclase-phyric lava domes associated with lava flows. 3) The lower member mainly consists of Welded peralkaline pantelleritic ignimbrite with an interbedded basaltic lava flows with a maximum thickness of 150 m. Their age is approximated to be 5.2-3.1 Ma (Tadiwos Chernet et al., 1998; Giday Woldegebrel et al., 1990; Tsegaye Abebe et al., 2005).

2.2.6 Structural setting of the study area

Situated within the transition of central to northern sector of the MER, the structural pattern of the study area is characterized by two fault systems: A roughly $N30^0$-40^0E trending border fault system and $N0^0$-20^0E trending fault systems (Tsegaye Abebe et al., 2005; Boccaletti et al., 1992). The former separates the main rift depression from the Ethiopian and Somalia plateaus, characterized by major fault escarpments. The continuation of Asela border fault is exposed at the foot of Chilalo volcano (Fig. 2.6) with in the southeastern part of the study area.

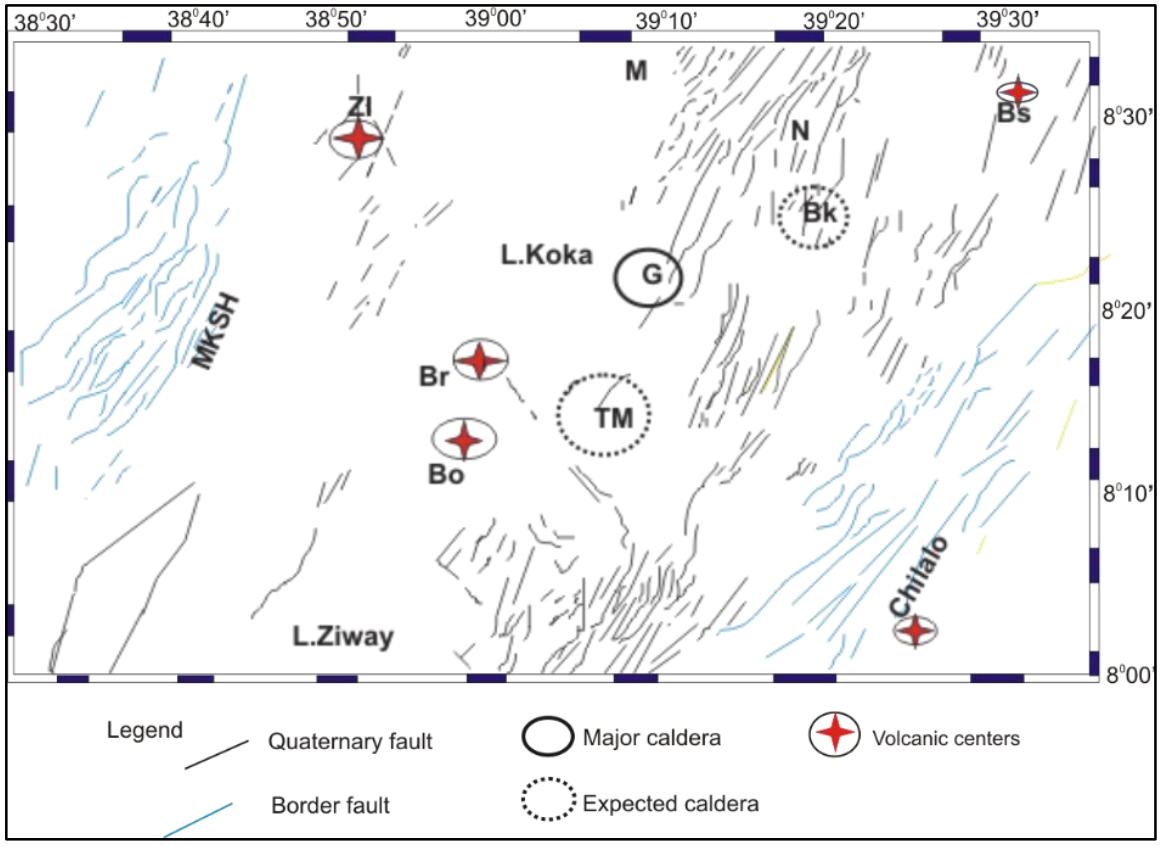

Figure 2. 6 Structural map of Gedemsa TMS and its environs (After Tsegaye Abebe et al., 2005). Abbreviations: M=Mojo, N=Nazret, Zi=Ziquala, Bs=Boseti, Bk=Boku, G=Gedemsa, TM=Tulumoye, Br=Bericha, Bo=Bora, MKSH=Midre Kebd Structural High.

Midre Kebd Structural High (MKSH) is exposed with in the western part of the area (Fig. 2.6).

The $N0^0$-20^0E trending fault systems affecting the rift floor, Wonji fault belt (WFB), are characterized by an echelon arrangement of right stepping branching of from the eastern and western margins. They are dense of fault swarms with steep scarps striking 20^0 counterclockwise from the border fault. The Pliocene-quaternary volcanics, sedimentary rocks and recent alluvial cover are affected by WFB systems reflecting quaternary tectonics. The two fault patterns have been attributed to two rifting models in the evolution of the MER: 1) Continuous NW-SE single phase orthogonal extension (Miocene-present) (Giday Woldegebrel et al., 1990) resulting the development of NE-SW trending boundary faults. 2) A more complex history polyphase deformation of two phase extension, a two phase extension which include Miocene-Pliocene orthogonal extension followed by quaternary oblique slip rifting (Bonini et al. 1997; Boccaletti et al., 1998).

2.3 Geothermal energy resources and the case for the Main Ethiopian rift

Heat from the Earth is an almost inexhaustible source of energy used since ancient time for thermal applications. Currently, geothermal energy is frequently part of a mixed solution to the energy problem (Pierrick, 2015). The following section addresses the fundamental points on geothermal resources and the case for the MER.

2.3.1 Geothermal energy fundamentals

By definition, geothermal resources are present everywhere on earth as it represents the heat naturally stored underground. A geothermal reservoir is thus a volume of rock from which heat can be extracted for a specific use where temperature and permeability are the two predominant physical parameters. On the other hand, a geothermal system is “any regionally localized geological setting where naturally occurring portions of the Earth’s thermal energy are transported close enough to the earth’s surface by circulating steam or hot water” (Williams et al., 2011). A geothermal system is thus made of three main elements (Fig. 2.7): a heat nearly 6,400-km-deep, is expected to be above 4,000°C (Hochstein, 1990). Heat flows constantly from its sources within the earth to the surface (EPRI, 1978). Hydrothermal geothermal resource can be found in same places as volcanoes, most often heat source of a geothermal

system. Most geothermal resources presently usable for electricity result from the intrusion of magma at great depths (0 to 10 km) into the earth's crust (Tester et al., 2005).

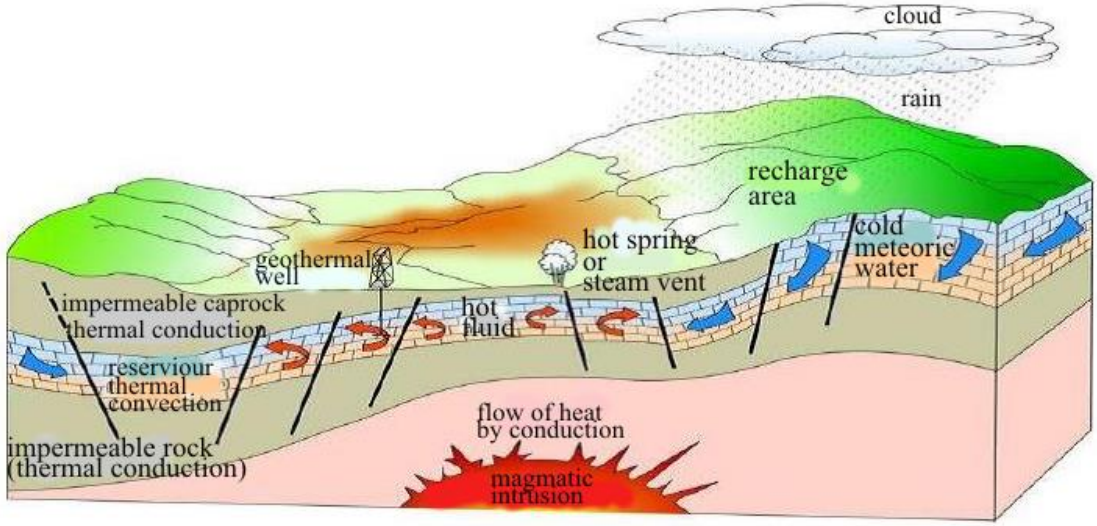

Figure 2. 7 conceptual model of a geothermal system (Hochstein, 1990).

2.3.2 The occurrence of geothermal resources within the Main Ethiopian rift

Likewise, to Iceland, Ethiopia is endowed with enormous geothermal potential (Bastow et al., 2011; Tigistu Haile and Tamiru Alemayehu, 2012) as rifting above anomalously hot mantle promotes the emplacement of magma into the shallow crust. The association of the MER with a series of volcanic episodes with collapsed structure results in shallow magmatic sources (Giday Woldegebrel et al., 1990; Boccaletti et al., 1999). As a result, Volcanoes in the MER have the potential to generate large amounts of geothermal power, a resource that is not well-exploited (Greenfield et al., 2019). Utilization of this renewable energy resource could contribute to a low-carbon sustainable energy mix for the growing economies in the country (Solomon Kebede, 2016; Samrock et al., 2018).

The Quaternary-recent volcano-tectonic activity of the MER with its fault swarms makes it the host (Corti et al., 2014) for the resource. The structural control of rift parallel faulting on the small scale recent volcanic features and on the geothermal system has been suggested by previous workers (Hutchison et al., 2015; Engdawork Admasu and Selamawit Worku, 2015). Geologic (Bekele Abebe et al., 2007), Geodetic (Bastow et al., 2011) and geophysical (Bastow et al., 2010; Kendall et al., 2006) observations detect shallow magma driving hydrothermal circulation in Aluto-Gedemsa area, geothermal potential prospective zones. As it is in

advanced stage of rift evolution, the highest geothermal potential is expected to be in the northernmost part of the MER as discussed below:

2.3.2.1. Corbetti geothermal prospect

Corbetti geothermal field is a Holocene volcanic complex hosted resource area found in the central sector of the MER (Martin-Jones et al., 2017), 250 km south of Addis Ababa. sedimentary and volcanic rocks with peralkaline pyroclastics are attributed to central-type eruptions with subsequent volcano-tectonic collapse in it.

2.3.2.2. Alutu-Langano geothermal prospect

Aluto is a Quaternary volcanics complex hosting geothermal field located along the WFB in the central MER at about 200 km SE of Addis Ababa. Studied widely, it is the first geothermal field in Ethiopia to be exploited where the only electricity producing geothermal power plant in the country is located (Meseret Teklemariam and Kibret Beyene, 2000).

2.3.2.3. Tulumoye-Gedemsa geothermal prospect

Tulumoye-Gedemsa is one of the lakes district geothermal prospects in the rift floor of the central sector of the MER. Currently, this area attracts exploration companies and academic researchers for its prospective geothermal resource and geologic relevance in understanding magma enhanced rifting processes. Seismic observation on the Bora-Tulumoye (Greenfield et al., 2019) between February 2016 and October 2017 reveals the occurrence of frequent seismicity triggered by hydrothermal circulation along preexisting fractures. According to Greenfield et al. (2019), fractures trending in parallel to the structures created during caldera forming eruptions could be attractive targets for geothermal power generation.

Furthermore, results from magnetotellurics represent an improved mapping of high-enthalpy geothermal reservoirs that form over magmatic intrusions (Samrock et al., 2018). But, the role of subsurface structure and potential heat sources, targeted in this study, remain unclear.

CHAPTER THREE

THEORETICAL FOUNDATIONS OF THE METHODS OF STUDY

3. Introduction

Geophysical methods have contributed invaluably through remotely sensing the nature and structure of the lithosphere (Hinze et al., 2013). Gravity and magnetic methods continue to have an important role as there are notable variations in density and magnetization properties of the crust and upper mantle that make up the lithosphere. This is particularly true in the crystalline portion of the lithosphere where structural deformation and intrusive events are more likely to result in near-vertical contacts, produces much more identifiable gravity and magnetic anomalies. Magnetometry and gravimetry are often referred to as structural methods. They have much in common, complement each other and supply more information about the subsurface than either technique on its own (Reynolds, 1997).

In geophysics, the gravity method exploits the earth's gravity field difference caused by lateral density variations. It plays two fundamentally useful roles in the earth sciences: 1) inexpensively detect "anomalies" worth studying. 2) Falsifies and eliminates models by forward computations. The method is also used in modeling the earth's crust and it is the basis for the study of the earth's shape (Telford et al., 1990). Geomagnetic methods can provide a wide variety of applications and range from small to large-scale regional geological mapping to determine gross structure (e.g., concealed igneous dyke intrusion, fault zones) (Reynolds, 1997). The field varies inversely one power faster with distance than does the gravity field; it is more sensitive to the source depth which is an important objective in interpretation of the observations. Despite its high resolving power (Hinze et al., 2013), it is much more complex due to dipolar nature and time based variation of the magnetic field (Telford et al., 1990).

3.1 The basics of gravimetry

3.1.1 Principles of gravity method

The basis for gravity method is Newton's law, a mathematical description of one of the most fundamental phenomena of nature. This law states that each particle of matter in the universe attracts all others with a force directly proportional to its mass and inversely proportional to

the distance between them. The force between a particle of mass m_1 centered at point Q = (x', y', z') and a particle of mass m_2 at P= (x, y, z) is given by:

$$F = \frac{Gm_1m_2}{r^2}\hat{e} \quad (3.1)$$

Where, r =radius, G is universal gravitational constant, G =$6.67x10^{-11}$ Nm^2 /Kg^2 and r is the distance between the two masses, m_1 and m_2 and $\hat{e}$ is a unit vector in the direction of the line connecting the center of the two masses.

When making measurements of the earth's gravity, we measure the gravitational acceleration, the time rate of change of a body's speed under the influence of the gravitational force. Newton's second law states that: force is proportional to acceleration.

$$F = \frac{Gm_1m_2}{r^2}\hat{e} = m_2g \quad (3.2)$$

In the case of earths mass, m_e and a body of mass, m, on its surface;

$$F = \frac{Gm_em}{r^2}\hat{e} = mg \quad (3.3)$$

If we solve equation 3.3 for g;

$$g = \frac{Gm_e}{r^2}\hat{e} \quad (3.4)$$

g–is gravity or acceleration due to gravity. The unit of 'g' is Gal in the honor of Galileo Galilei where 1 Gal =1 cm/s^2. However, the unit commonly used is mGal (1mGal=10^{-3} cm/s^2). If we consider earth as homogeneous, gravity would be constant. However, the Earth's ellipsoidal shape, rotation, irregular surface relief and internal mass distribution cause gravity to vary over its surface. The gravitational field is most usefully defined in terms of the gravitational potential U:

$$U = \frac{Gm}{r} \quad (3.5)$$

Unlike Gravitational acceleration, gravitational potential (U) is a scalar.

3.1.2 Gravity field and figure of the Earth

For a small mass, moving with a velocity, on the surface of the earth rotating with angular velocity as shown in the Fig 3.1a**,** different forces are acting on it and it is possible to develop the theoretical gravity or the normal gravity value of the earth. The resultant force per unit mass acting on m is;

$$\vec{g} = \vec{g}_m + \vec{g}_\omega + \vec{T} + \vec{C} \quad (3.6)$$

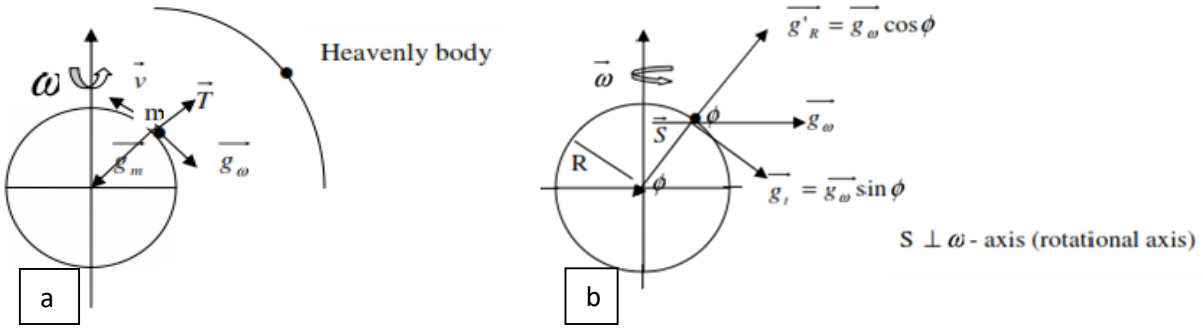

Figure 3.1 Gravity force per unit mass acting on a mass, m on earth (a) and components of forces acting on mass, m on earth's surface (b) (Reynolds, 1997).

Where g_m - attraction force per unit mass acting on due to earth's mass.

g_w - Centrifugal force per unit mass acting on due to earth's rotation with

T - Tidal force per unit mass acting on due to mass attraction of heavenly bodies

C - Coriolis force acting on due to its motion, and its value is zero if it is at rest.

If we assume the earth to be spherical in shape with radius r and neglect the effect of $\vec{C}$ and $\vec{T}$ in actual work, mass attraction and rotational forces per unit mass remain (Fig. 3.1b), gravity is only due to mass and rotational effects given by:

$$\vec{g} = \vec{g}_m + \vec{g}_\omega = \frac{Gm_e}{r^2}\hat{e} + \vec{\omega}(\vec{\omega} \times \vec{R}) \qquad (3.7)$$

Closely examining figure 3.1b, considering only the radial component, g'_R of $\vec{g}_\omega$ implies;

$$g = \vec{g}_m - g'_R = \frac{Gm}{R^2} - \omega^2 R\cos^2\emptyset \qquad (3.8)$$

g'_t is the tangential component of $\vec{g}_\omega$ having no effect on mass m. therefor equation 3.8 at the equator (g_e), where $\emptyset = 0°$ becomes;

$$g_e = \frac{Gm}{R^2} - \omega^2 R\cos^2\emptyset = \frac{Gm}{R^2} - \omega^2 R \qquad (3.9)$$

Similarly the gravitational acceleration at the pole (g_p), where $\emptyset = \pm 90°$ is given by:

$$g_p = \frac{Gm}{R^2} - \omega^2 R\cos^2\emptyset = \frac{Gm}{R^2} \qquad (3.10)$$

Equation 3.9 and 3.10 shows the minimum and maximum values of gravity at the globe respectively. The real earth observed gravity values are g_p=983.218 Gals and g_e=978.032 Gals with difference ($g_p - g_e$) of 5.2 Gals but calculations a spherical earth model results difference ($g_p - g_e = \omega^2 R\cos^2\emptyset$) of about 3.4 Gals. The disagreement between observed and calculated

value of gravity, for a spherical earth is due to the assumptions (spherical shape) used above. From these disagreements one can conclude that;

1. The shape of the real earth is not spherical, rotationally distorted, flattened at the poles and bulged at the equator (Fig. 3.2).

2. Gravity value, varies as a function of latitude (∅).

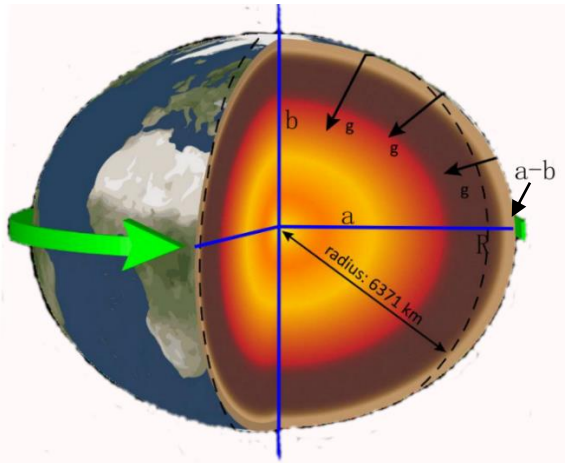

The bulged outward equator of the earth due its rotation is radially greater than the radius at the pole by a-b (Fig. 3.2): As shown in equation 3.4 gravity decreases with a function of radius square which supports the equator ward reduction in g (Fig. 3.2).

Figure 3.2 the gravity figure of the earth. where, a-b is the difference in equatorial and polar radius respectively. g: gravity and Fc=centrifugal force. (adopted from pierrick, 2015).

3.1.3 The Geoids and the Reference Ellipsoid

Geodesist or geophysicists consider two surfaces that represent the average shape of rotationally distorted earth to study its gravity field, geoid and reference ellipsoid (Fig. 3.3).

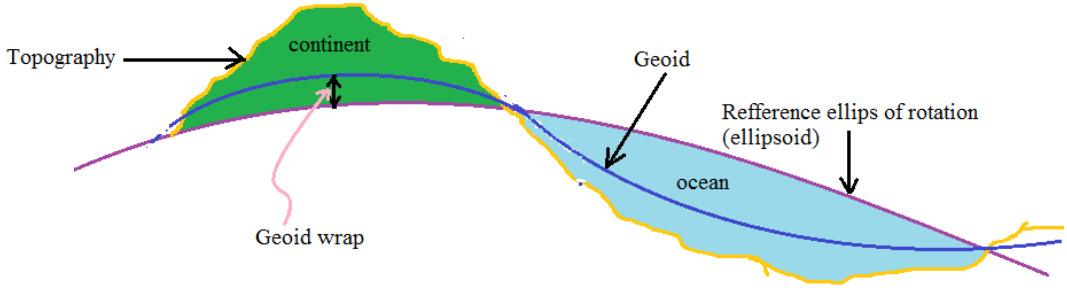

Figure 3.3 geophysical reference surfaces geoid, topography and ellipsoid (Reynolds, 1997).

In geodetic and geophysical measurements reference surfaces (topography, geoid, and ellipsoid) play key roles in theoretical calculations and physical measurements.

The reference spheroid: A mathematically generated theoretical earth model, flattened at the poles and bulged at the equator, neglecting undulations on the earth's surface where as we have

hills, mountains and depressions on the real earth. The flattening (*f*) of the earth is expressed as:

$$f = \frac{a-b}{a} = \frac{1}{298.25} \quad (3.11)$$

The theoretical value of gravity γ adopted by the International Union of Geophysics and Geodesy (IUGG) in 1930 and revised by the Geodetic Reference System in 1967 is given by

$$\gamma = g_e(1 + B_1 sin^2\emptyset + B_2 sin^2 2\emptyset) \quad (3.12)$$

Where, $g_e = 978031.846, B_1 = 0.005278895, B_2 = -0.0000059,$ and $\emptyset$ *is the* latitude.

The geoid: The reference geoid, physical equipotential surface referred to mean sea level, forms a reference surface for measurements of acceleration due to gravity. Hence to account continental elevation and ocean depression, it is necessary to define the geoid, as the average sea level over the oceans and over the surface of sea water (Telford et al., 1990). Geoid warped upward under continents because of attracting material above and downward over the ocean basins due to the low density of water (Fig. 3.3).

3.1.4 Fundamentals of Gravity data reductions

Although subsurface density variation is the main target, Gravity based observations include additional combined effects including: instrumental, surface, terrain, and planetary sources. To isolate the effects of subsurface sources, temporal and spatial variations are removed using theoretical considerations, geological information, and empirical observations. Reduction is a term refers to the conversion of raw gravity data to a usable form. Generally, Variations in gravity field of the earth arises from:

A. Temporal Based Variations - time dependent changes in the observed acceleration (e.g. instrument Drift and Tidal effects.

B. Spatial Based Variations -space dependent changes in the observed acceleration (e,g., Latitude variation, Elevation Variations , Slab Effects and Topographic Effects).

Much of the gravity signals in gravity works are produced by sources which are not of direct geological interest. Therefore, we must make corrections to reduce gravity to the values as they would have a datum on equipotential surface such as the geoid (Telford et al., 1990)**.** The fundamental corrections to be made in gravity survey are summarized in Table 3.1.

Table 3. 1 fundamental gravity data corrections

No	Source of non-geologic effect	Basic correction	Correction factor ($\pm$)
1	Change in elastic property of the instrument	Drift correction	$d(t_j - t_{Ab})$ where $d = \frac{R_{Ae}-R_{Ab}}{t_{Ae}-t_{Ab}}$
2	ellipsoidal shape of the earth and its rotation	Latitude correction	$0.812\sin 2\emptyset \times ds$
3	Elevation difference of observation points	Free air correction	0.308h
4	Excess mass between observation point and datum	Bouguer correction	$2\pi G\rho h = 0.4191\rho h$
5	Hill/valley near measurement	Terrain correction	Computer aided work

d-drift, t_j-time at j^{th} station, t_{Ab}-time at beginning of base station, R_{Ab} and RAe- relative gravity at the beginning and end respectively, h= height, ds=change in position (Telford et al., 1990).

3.1.5 Gravity anomalies

After appropriate data reduction, the final output of any gravity survey shows variations-anomaly of gravity in subsurface either of free-air anomaly (FAA) (Equation 3.13) or Bouguer anomaly (BA) (Equation 3.14). The equation for Free-Air anomaly (FAA) is given by:

$$FAA = g_{obs} - g_{\emptyset} + FAC \quad (3.13)$$

The FAA is nothing but squashing up all the mass above sea level into an infinitesimally thin layer at sea level, and measuring gravity there. Bouguer anomaly (BA) is given by:

$$BA = g_{obs} - g_{\emptyset} + FAC \ \pm BC + TC \quad (3.14)$$

BA is equivalent to removing away everything above sea level and forms the basis for the interpretation of gravity data on land.

3.2 Fundamentals of Magnetometry: Principles and elementary theory

3.2.1 Flux density, field strength and permeability

The existence of magnetic flux around a bar magnet indicated by the flux lines (Fig. 3.4) converging near the ends of the magnet, known as the magnetic poles. A bar magnet Suspended in free air will align itself with similar polarity of the earth's magnetic field. Magnetic poles always exist in pairs of opposite sense to form a dipole (Hinze et al., 2013). The magnetic field

B due to a pole of strength m at a distance r from the pole is defined as the force exerted on a unit positive pole at that point.

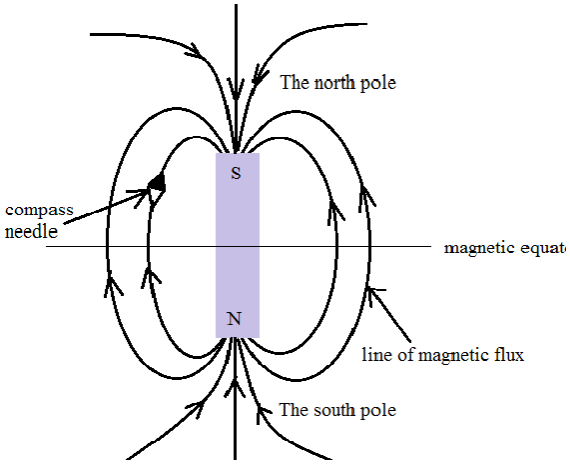

The closeness of the flux lines (Fig. 3.4), the flux per unit area, is the flux density B (and is measured in weber/m ^{2}=teslas). The attraction or repulsion force between two poles of strength m_1 and m_2 is given by:

$$F=\frac{m_1 m_2}{4\pi\mu r^2} \qquad (3.15)$$

$$B = \frac{m}{4\pi\mu r^2} \qquad (3.16)$$

Figure 3.4 Lines of magnetic flux around a bar magnet (Reynolds, 1997).

The unit is practical in geophysical work is called the nanotesla (nT=10^{-9}T). The magnetic field can also be defined in terms of a force field, the magnetizing field strength, H with units of ampere per meter as:

$$B = \mu H \qquad (3.17)$$

Since $\mu = \mu_r \mu_0$ equation 3.22 can be written as

$$B = \mu_r \mu_0 H \qquad (3.18)$$

Introducing $k + 1 = \mu_r$ where k is magnetic susceptibility and rock magnetization J as $J = kH$ to equation 3.18 results:

$$B = \mu_0 H(1 + k) \qquad (3.19)$$

Absolute magnetic permeability (μ) is the ratio of the flux density B to the magnetizing field strength H. μ of water or air is equal to that of free space (μ_0=4πx10^{-7} Wb A^{-1} m^{-1}). Relative permeability (μ_r) is the ratio of permeability of a medium to that of free space.

3.2.2 Magnetic susceptibility and intensity of magnetization

The geologically diagnostic parameter, magnetic susceptibility, κ (Equation 3.19), is measure of how susceptible a material is to becoming magnetized. The susceptibility (κ) values ranges from -1 to 1 and for a vacuum, μ_r =1and κ=0. which we called intensity of magnetization induced by the magnetizing force, H. Magnetization in the presence of applied external field

H is called induced magnetization whereas the existence of measurable field in the absence of the external field is known as permanent or remanent magnetization (Jr). A rock mass containing magnetic minerals will have an induced as well as a remanent magnetization. The magnitude and orientation of the resultant (J) dictate both the amplitude and shape of a magnetic anomaly (Fig. 3.5).

3.2.3 The Earth's magnetic field and its components

Geomagnetic field of the Earth originates largely from within and around the Earth's core.

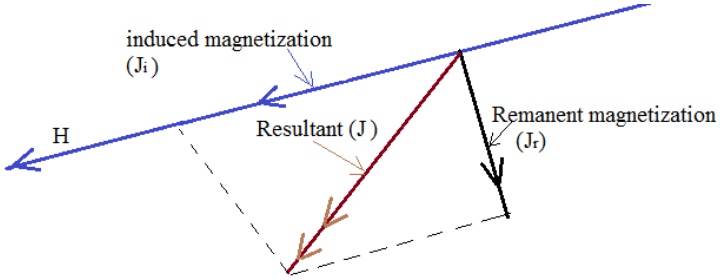

From equation 3.19 it is clear that for vacuum B= μ_0H as (κ=0). However, for materials other than vacuum there is an extra magnetizing field strength (κ H)

Figure 3.5 components of magnetization (Kearey et al., 2002).

Rock magnetizations are localized effects superimposed on the normal magnetic field of the Earth (Kearey et al., 2002). As a result, knowledge of the geomagnetic field is vital both in the reduction of magnetic data and in the interpretation of the resulting anomalies (Kearey et al., 2002). There are three components of the Earth's magnetic field: 1) the main dipole field, 2) the rock magnetization field and 3) the external field.

3.2.3.1 The main dipole field (Geodynamo)

The geomagnetic field main component is called the dipolar field located at the center of the Earth but inclined at 11.5° to the Earth's rotational axis. This field is produced by electric currents induced within the conductive liquid outer core, slow convective movements within it. The positions of the geomagnetic dipoles change with time (Reynolds, 1997) it can be described in terms of the declination (D), inclination (I), and total force vector (F) (Fig. 3.6).

3.2.3.2 The external magnetic field

Electric currents in the ionized layers of the atmosphere, magnetosphere, results the remaining small portion of the geomagnetic field which is more rapid in time based variation due to external activities (Telford et al., 1990). The external field has a quite complicated appearance

as it is strongly affected by the solar wind (Lowrie, 2007). The elements of geomagnetic field are related as:

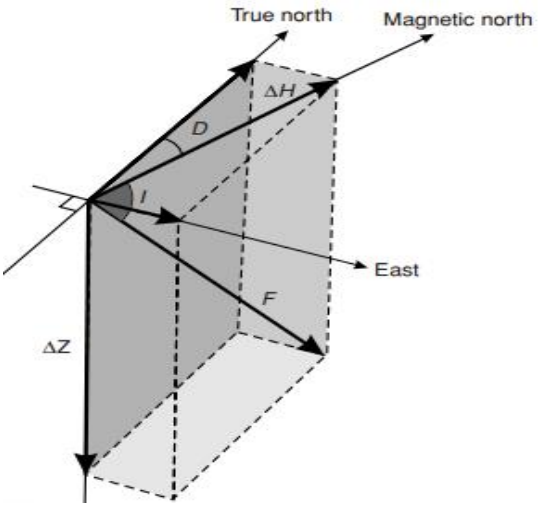

$$z^2 + H^2 = F^2 \qquad (3.20)$$

$$I = tan^{-1}\left[\frac{z}{\Delta H}\right] \qquad (3.21)$$

$$\tan I = 2\tan\gamma \qquad (3.22)$$

$where\ \gamma =$ latitude during rock formation.

Figure 3. 6 Elements of the magnetic field: inclination (I), declination (D), and total magnetic field, (F). (Lowrie, 2007).

3.2.3.3 Crustal (anomalous) magnetic field

The third component of geomagnetic field arise from magnetization of rocks which depend on the magnetic mineral content of near surface rocks. This is the most important component of geomagnetic field in exploration geophysics. The sources of local magnetic anomalies cannot be very deep because of the Curie temperature, associated with features in the upper crust (Telford et al.,1990). The total magnetic field, sum of its components, is expressed as:

$$B_T = B_{ext} + B_{int} = B_{ext} + B_D + B_{rm} \qquad (3.22)$$

Where, B_T=total field, B_{ext}=external field, B_D=dipole field, and B_{rm}=field of rock magnetism.

3.2.4 Variations in the Geomagnetic field

The earth's magnetic field is a dynamic phenomenon which varies with time and space. Time based variations include magnetic storm, diurnal and secular variations. Diurnal variation is variations of the Earth's magnetic field, related to sources of solar ionosphere (Dentith and Mudge, 2014). Electric currents flowing in the ionosphere generate magnetic fields which interfere with the Earth's field causing it to vary over minutes and hours (Dentith and Mudge, 2014). Magnetic storms cause rapid variations of the field, periods of milliseconds to minutes

making magnetic surveying impractical (Dentith and Mudge, 2014). Similar with gravity field, the earth's magnetic field varies with latitude, space based variations.

3.2.5 Basics of Magnetic data reduction

3.2.5.1 Diurnal correction

Magnetometry needs a very careful survey procedure as various factors cause our data to be erratic. The most important factor in which we have to consider is the daily variation in the intensity of the solar ionosphere. In addition to avoiding to do a magnetic survey with high radiation, we have a technique of removing the effect of daily variation in reading of the instrument called diurnal correction. Repeated reading in a given station (base station) with a constant interval of time enables us to do diurnal correction as:

$$\delta B_D = B_i \pm \left[\frac{\Delta B}{\Delta t}\right] \Delta t_i \qquad (3.23)$$

Where, δB_D = diurnally corrected data measured at time ti, Bi = magnetic field measured at time ti. $\Delta B = B_2 - B_1$; where B_2 *and* B_2 are base station reading at the beginning and end of the survey respectively. $\Delta t = t_2 - t_1$, where, t_1 and t_2 are base station time reading at the beginning and end of the survey respectively and $\Delta t_i = ti - t_1$ is the time difference of any station and base station respectively .

3.2.5.2 Geomagnetic correction

As gravity, the earth's magnetic field varies spatially. In this regard, the remaining total magnetic from diurnal correction is further reduced by IGRF correction to get magnetic anomaly. The magnetic equivalent of latitude correction is IGRF correction given by:

$$B_{IGRF-corrected} = \delta B_D - IGRF \qquad (3.24)$$

Where, $B_{IGRF-corrected}$=IGRF corrected total magnetic intensity, δB_D is diurnally corrected magnetic intensity value and IGRF is the International Geomagnetic Reference Field value defined by its latitude.

3.3 Interpretation of potential field (gravity and magnetics) data

Gravity and magnetics have much in common in data processing and interpretation. Interpretation is the art of translating geophysical signals in to geology. There are two approaches to the interpretation of gravity or magnetic anomaly data: direct and indirect method. In the former method, original data are analyzed to produce an interpretation where

as in the later models are constructed to compute synthetic gravity or magnetic anomalies which are compared in turn with the observed anomaly (Reynolds, 1997). Interpretation may be qualitative or quantitative.

After complete gravity or magnetic survey, appropriate data processing and removal of regional field, what comes next is straight forward: estimating the parameters of the source from observed gravity or magnetic while incorporating all available geological, geophysical and other independent information (Blakely, 1995). According to Blakely (1995), Interpretation techniques can be categorized in to two basic approaches although the goal of all the technique is to illuminate the spatial distribution of gravity sources.

Forward method: constructing an initial model for the source body based on geological or geophysical intuition is needed to calculate the model anomaly. The model parameters are adjusted until an optimum fit between the two anomalies. It is a repeated their step (Fig. 3.7) process of body adjustment, anomaly calculation and comparison until the two anomalies are best fitted.

Inverse method: source parameters are calculated automatically and directly from the observed anomaly with the aid of simplifying assumptions (Fig. 3.7).

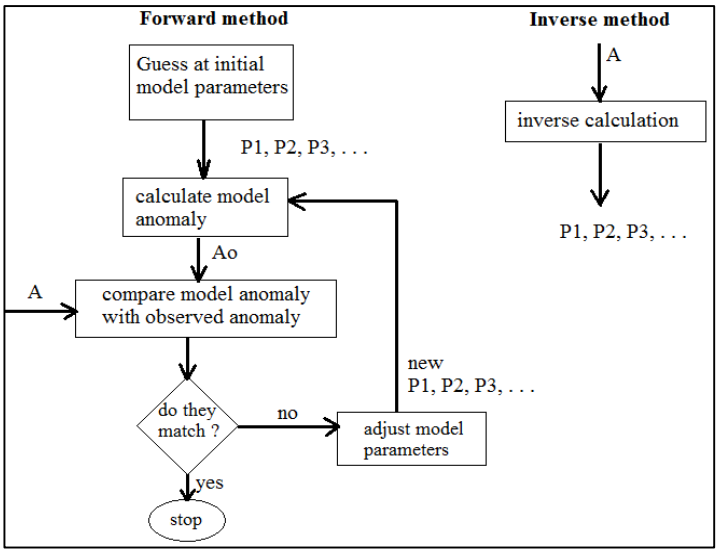

Figure 3.7 Modelling techniques of gravity data. Measured anomaly is represented by A, calculated anomaly by Ao, parameters P1, P2, P3, are attributes of the sources such as, depth, thickness and density (Blakely, 1995).

CHAPTER FOUR

DATA ACQUISITION, PROCESSING AND PRESENTATION

4.1 Data acquisition

4.1.1 Gravity data acquisition and distribution

The resolution and accuracy of data are the key factors in interpretation of gravity data. The MER has been investigated using regional gravity surveys (Mehatsente, 1999, Tiberi et al., 2005, and Mickus et al., 2007) based on ground gravity data. However, the resolution and accuracy of the ground gravity data employed by these surveys could be claimed to be low. The topographic complexity of the area when performing ground gravity surveys is liable to result in low resolution and poor data coverage. The data collected by different individuals and different instruments at different times is liable to result in different observed gravity values for the same observation station. To minimize and avoid effects of the above limitations, the present study uses gravity data which is part of the new ultra-high resolution picture of Earth's gravity field aimed at getting better investigation results.

The gravity data for this research was provided by the International Gravimetric Bureau (IGB) freely through htt://ddfe.curtin.edu.au/gravitymodels/GGMplus/GGMplus-readme.dat/ of an available website. IGB is an association of world Geodesists and Geophysicists aimed to collect, compile and store all measurements of the earth gravity field so as to redistribute on request to a large variety of users for scientific purposes (https://edx.netl.doe.gov). The data employed in this work is part of world gravity grids and models, Global Gravity model plus (GGMplus2013), which is the result of a research intuitive of Curtin (Australia) and Munich (German) universities. GGMplus2013 is a composite of ground gravity data, satellite gravity data and topographic gravity effects (Hirt et al,. 2013). The plus in GGMplus2013 indicating the leap in resolution over previous global gravity models (200 m×200 m). Regarding to the satellite data component, it consists of the latest satellite measured gravity data from the European Space Agency's (GOCE satellite) providing the highest resolution picture of Earth's gravity currently (Hirt et al,. 2013). The conversion of topography to topographic gravity effect is based on the residual terrain modeling technique. Addition of all components (terrestrial, satellite and topographic gravity effects) using massive parallel computation techniques results in the ultrahigh-resolution gravity picture of the globe (Hirt et al,. 2013).

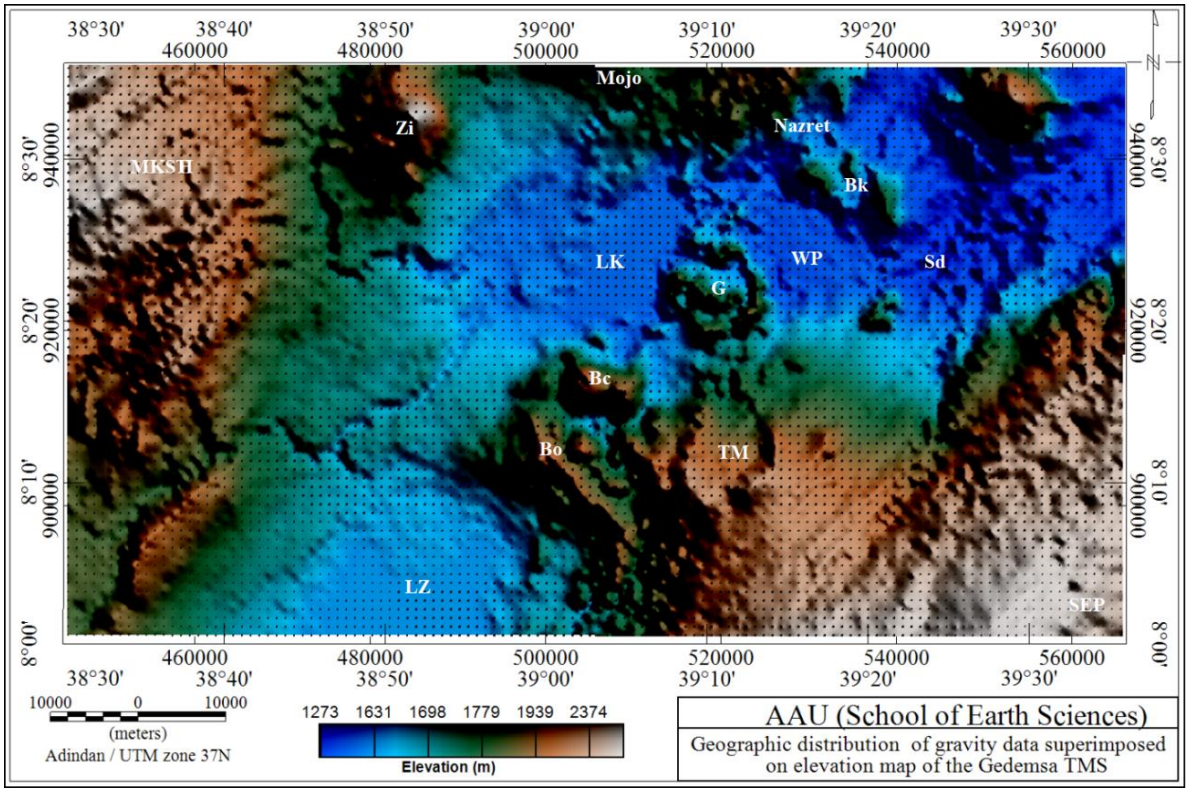

Figure 4.1 Geographic distribution of gravity data (black dot) superimposed on shadowed elevation map. The abbreviations are, MKSH=Midre Kebd Structural High, SEP south eastern plateau, Zi=Ziquala volcano, Bk=Boku volcanic complex, Sd=Soderie, Bo=Bora m

In this research, the row data was downloadded through the available wavepage and converted to gravity data sheet using MatLab software. Primarily a total of 37,074 gravity data points were extracted from 38^0 to 40^0 and 7.5^0 to 9^0 geographic longitude and latitude of the MER respectively to characterize the subsurface at a crustal scale. From the overall data, about 8,052 data falls with in the Gedemsa TMS and its environs with an absolute station interval of 0.2 km (200 m×200 m resolution) (Fig. 4.1). The resolution and accuracy of the data is sufficient enough to characterize the subsurface structure of the area at a local and regional scale.

4.1.2 Magnetic data acquisition and distribution

The magnetic survey was conducted using GSM-T19 proton precision magnetometer. It is an automatic recording instrument with a resolution and absolute accuracy of 0.01 and 0.02 nT respectively over its full range temperature. Although all of the components can be packed in one packing box (Fig. 4.2a) for simplicity and safety, it has three basic separate elements: reading and recording instrument (Fig 4.2b), sensor (Fig 4.2c, the bottom white), the GPS (Fig.

4.2c, top white circularly shaped). The overview on operation of the survey is shown in Figure 4.3 of which the primary data acquisition has been completed within 10 days. The primary data were collected with an average station interval of 0.3-0.6 km and approximately E-W profiles. In addition, data were also acquired in a random profile for the ease of interpolation of the survey data. Base stations were established and repeated measurements were conducted there to preclude the effect of daily variation of the observed geomagnetic field. A total of about 1400 data points have been utilized in this work of which about 940 data points are acquired previously by the Geological Survey of Ethiopia (GSE). The remaining 500 data points were collected by the researcher from march 18/2020 to march 28/2020.

Figure 4. 2 instrumentation and data acquisition of magnetic survey: packing box(a), reading and recording instrument(b), GPS antenna (top white circle) and sensor (bottom white) (c).

In a hope of crossing the SSW-NNE quaternary faults and other hidden structures related to the E-W extension direction of the MER, most of the survey lines were chosen to be E-W profile lines across the rift floor of the MER. Despite the gravity data distribution which cover the Gedemsa and Tulumoye volcanoes including the rift flanks, the magnetic data distribution precludes the rift margins being concentrated on the geothermal prospect area associated with Tulumoye, Gedemsa and Bericha volcanic complexes (Fig. 4.4).

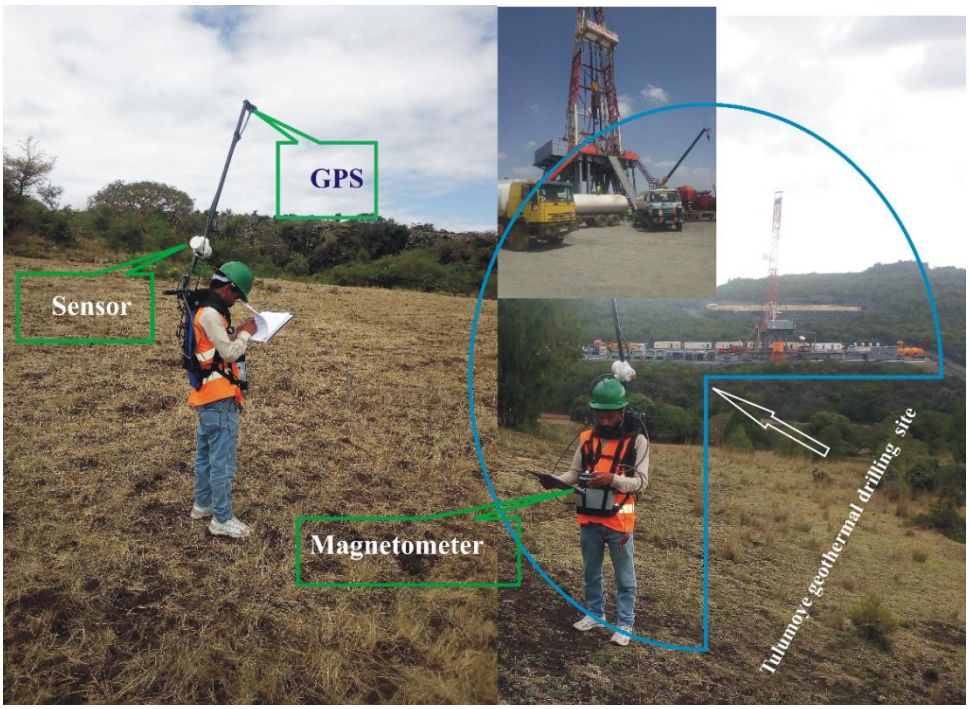

Figure 4.3 Magnetic field data acquisition at north east of Tulumoye geothermal field.

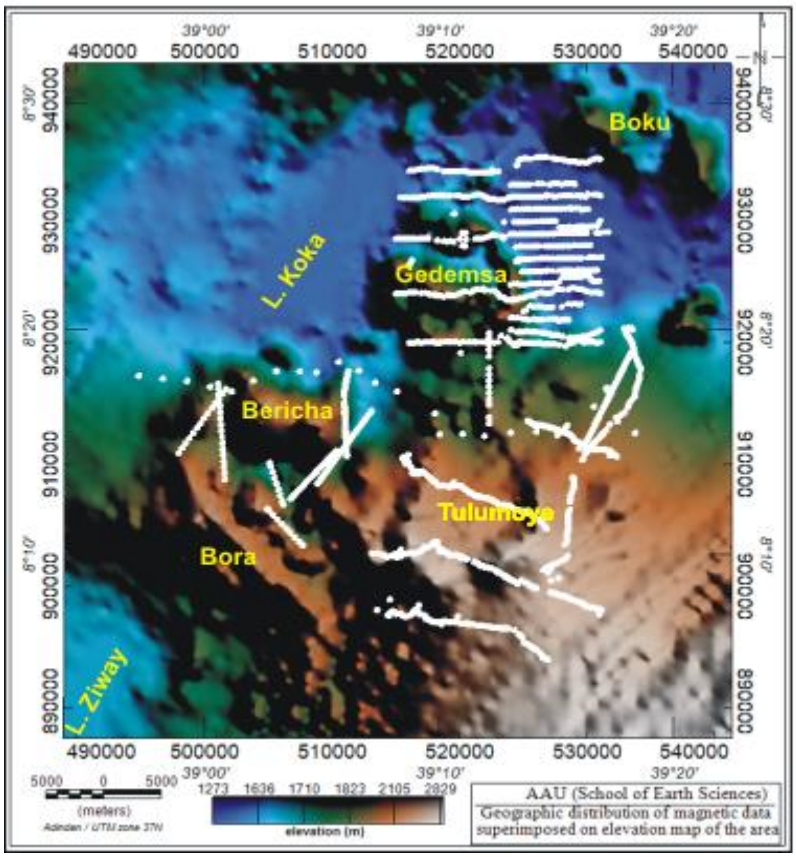

Figure 4. 4 Geographic distribution of the magnetic data (white dots).

4.2 Data processing

Gravimeters or magnetometers do not give the direct measurement of gravity or magnetic data for interpretation as additional factors affect those instruments. As a result, field observations are processed to minimize or remove these extraneous effects that result from indirect geological interest. This conversion procedure is commonly referred to as correction or reduction of the gravity or magnetic data.

4.2.1 Data correction

As discussed in section 3.1.4 and 3.25, reduction of gravity or magnetic data is nothing more than translating the row data in to usable form (see also Table 3.1). In this regard, correction does not imply that errors are present in the data and reduction does not suggest that the data are reduced to a common vertical datum. However, both terms refer to the conversion of raw gravity or magnetic observations to anomaly form.

It is not possible to download the gravity data in a usable form directly from the IGB. In this thesis, the row data provided by the IGB was processed and converted to usable data format using MatLab software. The conversion results to geographic location of each data with their respective observed gravity and elevation value. The complete Bouguer anomaly map (Fig. 5.2) in this thesis is the end result of the following fundamental procedures of gravity data reductions: The data provided from the BGI is an observed gravity. As a result, the theoretical gravity value at each observation station is computed using the Geodetic Reference System 1967 (GRS67). The data was corrected for Free air and Bouguer plate using a free-air gradient of 0.3086 mGal/m and a reduction density of 2.67 g/c^3 respectively (Table 3.1). In addition, topographic effects were removed by applying Terrain corrections which intern computed by using digital elevation model (DEM) as an input.

The final gravity anomaly is the difference between the observed gravity and the theoretical gravity values at each of the station. The end results of the gravity survey such as the free-air anomaly values and the complete Bouguer anomaly values of all the stations considered in the study area have been determined as part of the processing sequence.

As other magnetometers, the instrument used in the present magnetic survey can't be sense the effect of only magnetic sources from the subsurface of the study area. However, the daily

variation of solar ionospheric as well as anthropogenic factors should have recorded as a part of measured data. Magnetic anomaly is nothing but the remaining magnetic field strength after taking account the effect of all non-geologic factors, applying both diurnal and IGRF correction in the case of this study. In this work, the effect of man-made objects and magnetic storms were tried to reduce by avoiding a magnetic survey measurement in the presence of such conditions. However, the daily variation of the instrument or diurnal variation were eliminated by a process called diurnal correction as discussed in section 3.2.5. The diurnally corrected data (total magnetic intensity) were also further processed for IGRF correction to get the total magnetic anomaly at each station of the area.

4.2.2 Gridding and mapping of gravity and magnetic data

Despite having different application, the data processing steps in gravity and magnetic methods are more or less similar. Towards this end, the finally reduced gravity or magnetic data were compiled and further processed using Geosoft Oasis Montaj (version 8.4) software: The data has been gridded or regularly interpolated on a 0.2×0.2 km and 1×1 km square grids using a gridding algorithm of minimum curvature to create a spatial map display for the gravity and magnetic data respectively. Following the gridding, gravity and magnetic data were prepared for further data processes (enhancing, mapping and modelling).

4.2.3 Data enhancement

Only reduction of gravity or magnetic data in to anomaly form can't enable us to translate the anomaly to the correct subsurface geological information. Prior to modeling of gravity data relevant information can be extracted from the gravity data itself (Tilahun Mammo, 2010) using various filtering techniques. A technique called data enhancement or filtering helps us in highlighting anomalies of preference through certain spectral aspects of observed Bouguer gravity or magnetic anomalies. In this regard, a suit of carefully chosen enhancement techniques enables us to shed structural trends, fault kinematics, crustal architecture, regional tectonics, and intrusive bodies. In a hope of this, different data enhancement techniques were employed including upward continuation, wavelength filtering, band pass filtering, horizontal derivative, analytical signal, tilt derivative and Euler deconvolution.

The most and primarily important step in gravity and magnetic data interpretation is the regional-residual separation of gravity and magnetic anomaly which was part of data

enhancement in this work. The observed gravity or magnetic anomaly represents the total effect of deep seated geologic sources which results long wavelength anomalies and shallow geologic sources that give rise to short wavelength anomalies. Detail analysis of gravity or magnetic data needs to separate the regional from the observed data called regional-residual separation. This requires estimating the regional anomaly using an appropriate standard technique so that the estimated regional component can be subtracted from the complete Bouguer or total magnetic anomaly to determine the residual anomaly component.

In this thesis, the upward continuation and the wavelength filtering techniques were used to estimate the regional gravity and magnetic anomaly components respectively. Those techniques suppress all the short wavelength (residual) components arising from shallow sources and enhances the long wave length (regional) components arising from deep seated sources. The residual gravity anomaly is obtained by subtracting the regional anomaly from the complete Bouguer anomaly and similarly the residual magnetic anomaly is obtained by subtracting the regional magnetic anomaly from the total magnetic anomaly.

4.3 Data presentation

Data presentation is one of the key stages in every gravity and magnetic survey which assists our interpretation. A successful geophysical survey needs careful data acquisition, processing, presentation and interpretation (Fig. 1.5). Translating gravity and magnetic data into geology requires an appropriate data presentation. A processed data of the two potential fields can be presented in the form of profiles (1D), maps (2D), or models (2D or 3D). In this research the final processed gravity data is presented in the form of maps including: Free air anomaly (Fig. 5.1), Complete Bouguer anomaly (Fig. 5.2 and 6.2), upward continued (Fig. 5.3 and 5.5), residual anomaly (Fig. 5.4 and 6.2), derivatives (Fig. 5.6, 5.7 and 5.8), band pass filtered (Fig. 5.9, 6.3 and 6.4) and Euler deconvolution (Fig. 5.10). In addition, an attempt has been made to present the gravity data in the form of 2D density models (Fig. 6.5, 6.6, 6.7 and 6.8) with profiles (1D). Finally, the 2D density models and the geological map of the area are combined together to understand the upper crust in 3D view (Fig. 6.9). The magnetic data is presented in the form of maps including: total magnetic intensity (Fig. 5.11), total magnetic anomaly (Fig. 5.12), regional magnetic anomaly (Fig. 5.13), residual magnetic anomaly (Fig. 5.14), upward continued (5.15) and derivatives (5.16 and 5.17).

CHAPTER FIVE

RESULT, ANALYSIS AND INTERPRETATION

5.1 Gravity data Result, analysis and Interpretation

The amount of geological information at hand and the precision of gravity survey are the key factors in interpretation of gravity data. The Gedemsa TMS and its environs have been included in subsequent geological studies to get an insight on evolution of the MER (Kazmin, 1980; Giday Woldegebrel et al., 1990; Mazzarini et al., 1999; Tsegaye Abebe et al., 20015). As a result, there is sufficient geological information in the area to interpret the geophysical data employed in this work. The gravity data utilized in this study has a sufficient areal coverage and high resolution to interpret the subsurface of the area precisely at local scale than the previous regional gravity surveys. Moreover, careful data processing and enhancement techniques were applied to picture the subsurface beneath the area with a better resolution.

Of the three types of gravity anomalies; free air, Bouguer and isostatic, only free air and Bouguer anomalies were considered in the present work. As discussed in section 3.1.4, both anomalies are highly correlated with elevation of an area. The interpretation of the geophysical data in this research includes simple qualitative to semi-quantitative descriptions of maps or profiles (chapter 5) and more advanced quantitative interpretation (chapter 6). The quantitative interpretation consists of empirical determination of geologic parameters through 2D forward modelling of gravity data as discussed in chapter 6.

5.1.1 Topographic, free air and complete Bouguer anomaly maps

Situated within the Central to northern MER transition zone, the Gedemsa TMS and its adjacent areas show heterogeneously rugged topography (Fig. 4.1). A casual glance of Figure 4.1 shows that the rift flanks (eastern and western rift margin) and Ziquala Mountain are the highly elevated localities in the study area. The SW-NE aligned lower elevated locale shows the rift floor of the MER with quaternary volcanoes which are reflected by the circularly ridge shaped peaks. The transition from low lands (elevation up to 1200 m) of the rift floor (Blue color) to high lands (elevation up to 3000 m) demarcates margins of the rift (blue color). The exact separation of the central and northern MER remain unclear: Some authors reported that the separation of the two segments is near the Gedemsa region (e.g. Corti, 2009; Boccaletti et

al., 1999). Figure 4.1 shows sudden decrease in elevation of the rift floor after the northern termination of the Gedemsa TMS.

Free air anomaly is the gravitational acceleration after removal of the effect of elevation using a mathematical model (Equation 3.13). The free-air gravity anomaly takes into account the theoretical gravity and the vertical change in gravity between the reference datum and the observation height. The intervening space between the observation point and the height datum is assumed to have no mass or gravitational effect (Hinze et al., 2013). Unlike other anomalies no assumptions are made about the Earth's mass and it is the most basic anomalies used in geologic studies.

In this research, free air anomaly map (Fig. 5.1) has been compiled after taking account the theoretical gravity and elevation above sea level using oasis montaj software. The positive correlation between free air anomaly and elevation is described mathematically in Equation 3.13. This is also clearly revealed by comparing the elevation (Fig. 4.1) and free air anomaly (Fig. 5.1) maps of the present study. Examining these maps reflects that higher elevated localities, north western and south eastern plateaus as well as mountains (Ziquala), are characterized by positive free air anomaly. Conversely, lower elevated localities of the rift floor are characterized by relatively negative free air anomaly which is as low as -32 mGal. One can't ignore the fact that an undulated topography like the Gedemsa TMS results in high range value (100 mGal) of free air anomaly.

The Free air anomaly is unsuitable for the interpretation of local gravity studies as it doesn't take account the effect of masses between observation point and reference geoid (Hinze et al., 2013). The effect of the attraction of rock units between observation point and reference geoid can be precluded using Bouguer plate correction (equation 3.14). The remaining gravity value after allowing the effect of elevation, theoretical gravity and the mass between observation point and geoid is simple Bouguer anomaly (Telford et al., 1990). In fact, for a Bouguer anomaly to be complete, the effect of topography (terrain correction) must be considered. Figure 5.2 shows the complete Bouguer anomaly (CBA) map compiled for the Gedemsa TMS and its surroundings. Closely examining the mathematical equations for CBA (Equation 3.14) enables us to evaluate the effect of elevation in gravity survey. In this regard, it is better to consider the spatial variation in elevation of the area (Fig. 4.1) so as to interpret the subsurface

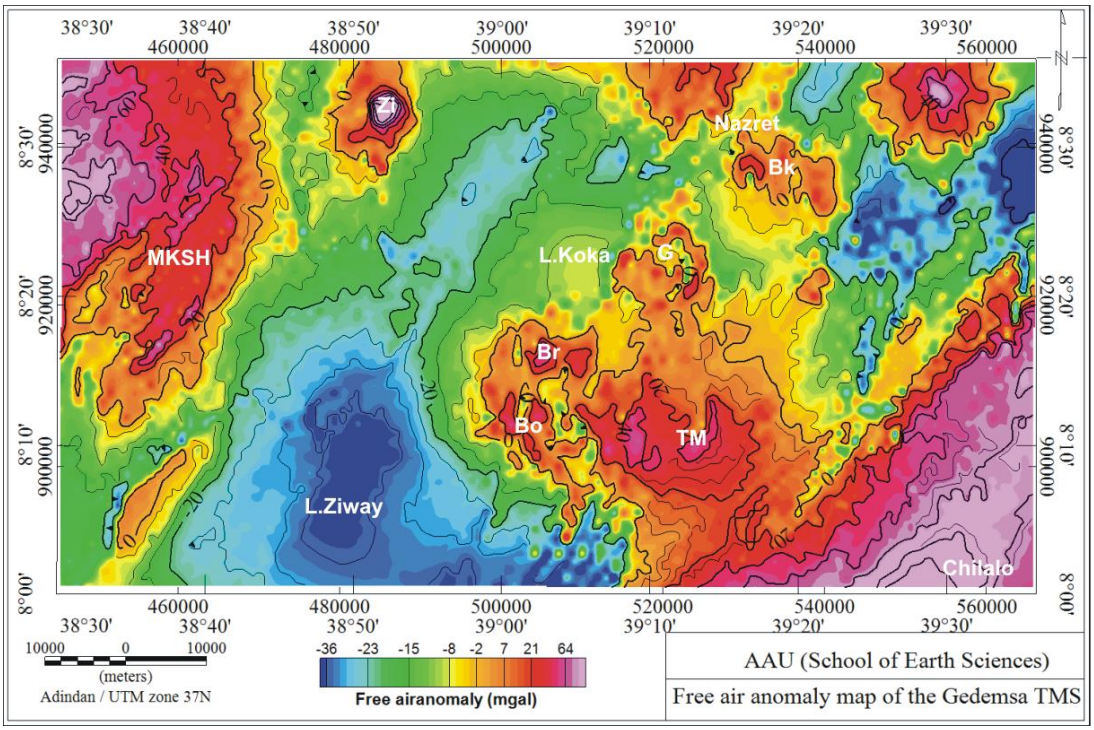

Figure 5.1 Free air anomaly map of the Gedemsa TMS and its environs. Labels: MKSH=Midre Kebd Structural High, Zi=Ziquala volcano, Bk=Boku volcanic complex, G=Gedemsa, TM=Tulumoye volcano, Bo=Bora mount, Bc=Bericha mount, LZ=Lake Ziway, LK=Lake Koka.

geology based on gravity data. A casual glance of it implies that the spatial variation in Bouguer anomaly is negatively correlated with elevation (Fig. 4.1). It is known that CBA is negatively correlated to broad topographic variations that are isostatically compensated (Hinze et al., 2013). Because of the relatively smaller size of the area, the observed gravity anomaly map (Fig. 5.2) could be attributed to the effect of lower to upper crust density heterogeneities. Three regions of gravity field signatures are observed by closely examining the CBA map (Fig. 5.2): high (-199 mGal to 180 mGal), intermediate (220 mGal to 200 mGal) and low (-245 mGal to 221 mGal).

The floor of the MER after the northern termination of the Gedemsa TMS and its surroundings is characterized by gravity maxima. On the contrary, the remaining parts of the rift floor including the rift flanks in the study area are characterized by intermediate gravity response (Fig. 5.2). Gravity minima are coincident with the Eastern flank of the rift corresponding to the SE Plateau. The change in behavior of the MER near the Gedemsa region can be observed

clearly from the CBA map (Fig. 5.2) by sudden increase in gravity field.

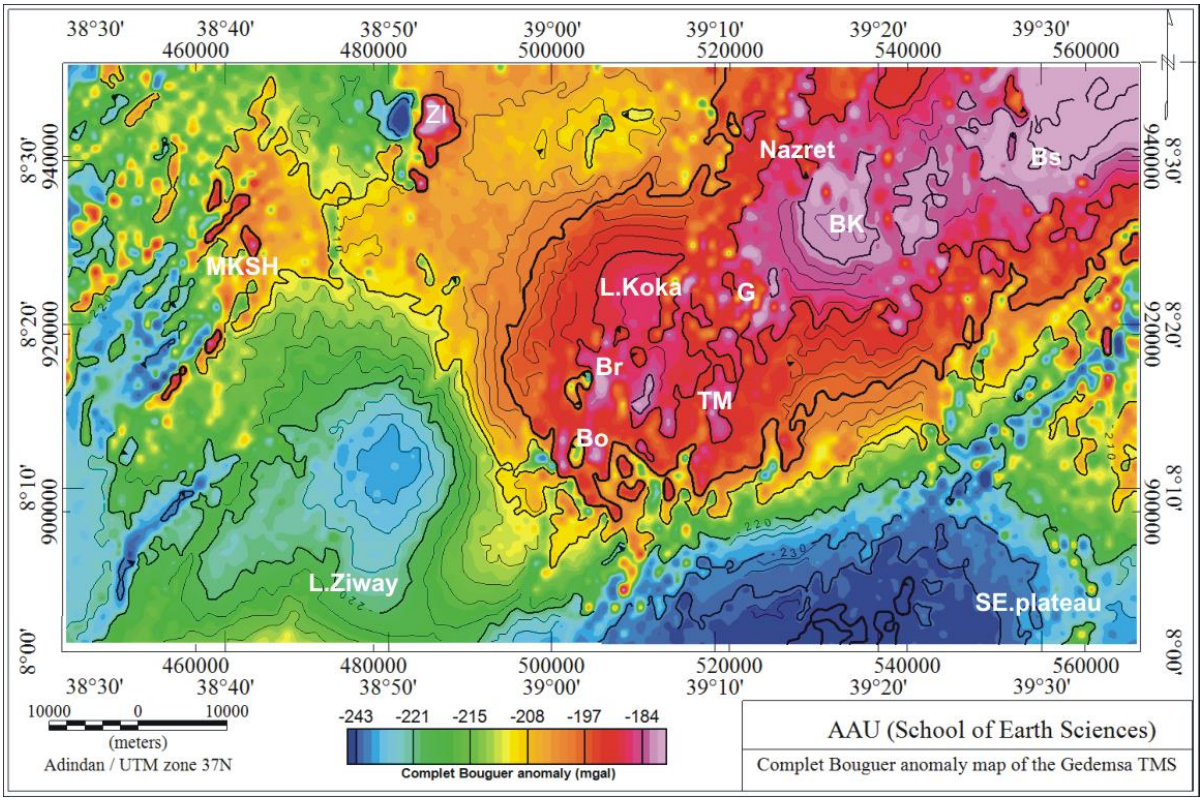

Figure 5.2 Complete Bouguer anomaly map. Labels: SEP=south eastern plateau, MKSH=Midre Kebd Structural High, Zi=Ziquala volcano, Bo=Bora, Bc=Bericha. Bk=Boku volcanic complex, Boseti= Boseti volcano, L. Ziway=Lake Ziway, L. Koka=Lake Koka and TM and G denote Tulumoye and Gedemsa quaternary volcanic centers respectively.

This northward increase in the CBA map following the protoridge axis of the MER has been attributed to a decrease in depth of crust mantle interface or an increase in crust/upper mantle density (Tiberti et al, 2005). The CBA map (Fig. 5.2) is the combined effect of deep (longer wavelength) and shallow (shorter wavelength) seated bodies. As a result, shorter wavelength anomalies are masked by longer wavelength anomalies and it is a difficult to get information on depth of the causative bodies. In this regard, separating the regional field from its residual counterpart (section 5.1.2) simplify the task of interpretation of the gravity data.

5.1.2 Upward continuation as regional-residual separation of gravity field

The mathematical projection of potential fields from a datum vertically up to another datum is known as upward continuation (Jacobsen, 1987). It simulates the anomaly as if the data has

been obtained at that levels. According to Jacobsen (1987), an upward continuation of a potential field to a height of z enables us to see anomaly sources at and below a depth of z/2. The gravitational attraction per unit mass of an anomalous body of mass *dm* at the msl Q(x_o, y_o, z_o=0) a distance R from the body location point Q(X,Y,Z) is given by:

$$dg = \frac{Gdm}{R^2} = \frac{Gdm}{(\boldsymbol{x-x_0})^2+(\boldsymbol{y-y_0})^2+(\boldsymbol{z-z_0=0})^2} \quad (5.1)$$

The vertical component dg_z gives a gravity anomaly Δg_o of the source at the msl (z_0=0) is:

$$dgz = \frac{Gdm}{R^2}\frac{z}{R} = Gdm\frac{z}{R^3} = Gdm\frac{\boldsymbol{z}}{\left[(\boldsymbol{x-x_0})^2+(\boldsymbol{y-y_0})^2+(\boldsymbol{z})^2\right]^{3/2}} \quad (5.2)$$

Likewise, the gravity anomaly Δg_p of the anomalous source located at Q(x, y, z) and measured at an upward continued surface of point p(x_o, y_o, -h) with distances between p and Q is:

$$dg = \frac{Gdm}{s^2}\frac{z+h}{s} = Gdm\frac{z+h}{s^3} = Gdm\frac{z+h}{[(x-x_0)^2+(y-y_0)^2+(z+h)^2]^{3/2}} \quad (5.3)$$

Upward continuation is a smooth, low-wavenumber pass filter which emphasizes the anomalies from the broader, deeper sources at the expense of the shallow-sourced anomalies (Hinze et al., 2013). It effectively attenuates noise without changing the physical significance of the data. In this work, this data enhancement technique has been used to understand the regional gravity field variation at different depths (Section 5.1.2.1), residual gravity anomaly pattern (Section 5.1.2.2) and gravity responses of the TMS at different depths (Secion 5.1.2.3).

5.1.2.1 The regional gravity anomaly map compiled from upward continuation of the complete Bouguer anomaly

Characterizing the causative bodies of gravity anomaly varies as per our interest in depth of investigation. The regional anomaly is considered here in order to study the entire crust beneath the Gedemsa TMS and its environs. The regional gravity anomaly map (Fig. 5.3) of this work has been compiled by upward continuation of the CBA map (Fig. 5.2). In a hope of observing the effect of deep seated bodies, the CBA map (Fig. 5.2) has been continued for different continuation distances (Fig. 5.3). In this regard, Figure 5.3 provides an important insight in understanding the pattern of regional gravity field at different distances. Upward continuation of the CBA map to 5 km, 10 km 20 km and 40 km have been made to see the gravity effect as if we observe the subsurface at 2.5 km, 5 km 10 km and 20 km depths surface respectively. A careful observation of Figure 5.3 reveals a subsequent suppression and enhancement of shallow and deep seated bodies respectively.

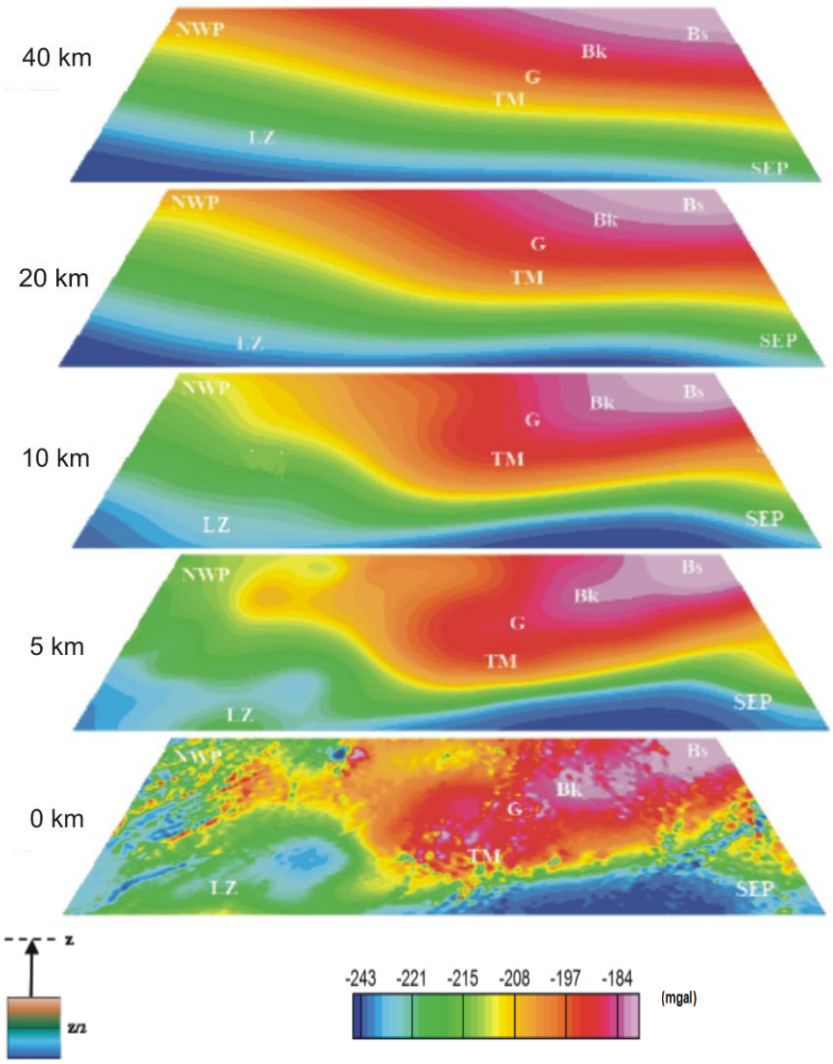

Figure 5.3 Regional gravity anomaly map obtained by upward continuation of the complete Bouguer anomaly map to heights of 2 km, 5 km, 10 km, 20 km, and 40 km. Labels: Z=height of upward continuation, SEP=south eastern plateau, NWP=North western plateau, LZ=Lake Ziway, Bs=Boseti, Bk=Boku volcanic complex, TM and G denote Tulumoye and Gedemsa quaternary volcanic centers respectively.

The CBA map at the ground level (0 km) (Fig. 5.3) shows the effect of shallow seated bodies superimposed on deep seated bodies. However, upward continuation of the CBA map to 5 km to see the anomaly sources buried beneath 2.5 km reveals the removal of the short wavelength and enhancement in effect of deep seated bodies. Four gravity regions can be identified at a glance of this map: 1) Very low gravity responses of deep seated bodies is observed at the flanks of the rift (SEP, and west of lake Ziway). 2) The rift margins and its floor after the southern termination of the Gedemsa area are reflected by low gravity response. 3) The floor

of the rift and the Gedemsa TMS is reflected by intermediate to high gravity responses. 4) Very high gravity field response is observed northward after the southern termination of the Boseti TMS. This gravity anomaly zones are further enhanced (10 km, 20 km and 40 km upward continuation) with subsequent suppression of shallow seated bodies (Fig. 5.3).

The general regional gravity trend of the MER is shown on the regional Bouguer anomaly map (Fig. 5.3) with northward gravity increment following the protoridge axis. At smaller upward continuation distances the effect of border faults and structural highs are observed as a general northeast striking feature. A sudden increase in regional gravity anomaly (Fig. 5.3) is observed north and northeast of the Gedemsa TMS. This gravity anomaly signature reinforces the explanation that the NMER is more evolved than the central segment, suggested by previous geologic (Ebinger and Casey et al., 2001; Wolfenden et al., 2004; Agostini et al., 2011; Bonini et al., 1997; Corti, 2009; Mazzarini, 2011) and Seismic (Keranen et al., 2004) studies.

5.1.2.2 The residual gravity anomaly map

The CBA map (Fig. 5.2) which contains the short and long wavelength components together is not simple for interpretation and separating it in to its regional and residual components is very important to avoid this ambiguity. Regional studies reported the occurrence of TMSs beneath the axis of the rift at a depth range of 12–25 km (Keranen et al., 2004; Whaler and Hautot, 2006; Daly et al., 2008). Aiming at mapping the Gedemsa TMS, the residual gravity anomaly map (Fig. 5.4) is compiled by substracting the regional anomaly obtained 40 km upward continuation of the CBA map (Fig. 5.2) from the actual CBA map (Fig. 5.2). In Figure 5.4 the effect of geologic bodies buried beneath 20 km depth are neglected. It consists only the effect of shallow subsurface (approximately less than 20 km) distribution of geologic bodies. The Gedemsa and Boseti TMSs are characterized by gravity maxima in the CBA map (Fig. 5.2). However, Figure 5.4 shows more localized shorter wavelength positive gravity anomalies as compared to the CBA map (Fig. 5.2). Whereas, the plateaus and mountains lying NW and SW of the Gedemsa TMS show negative gravity anomaly values. Smaller circular contour lines describe the presence of several volcanic centers forming of caldera (Gedemsa, Tulumoye and Boku) within the rift and off rift volcanoes (e.g, Ziquala). The most notable feature of Figure 5.4 is a NE strike feature of gravity maxima, crossing the area diagonally, which appears to be broader over the Gedemsa TMS.

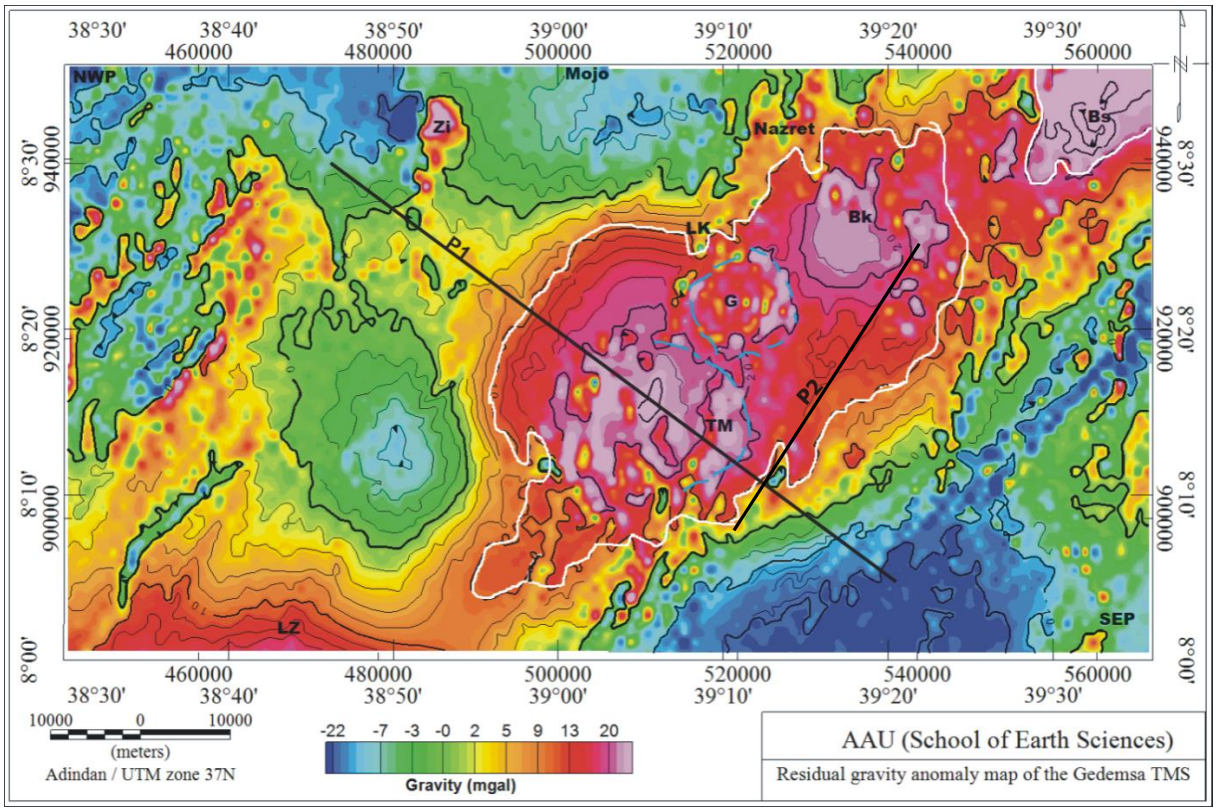

Figure 5.4 Residual gravity anomaly map. Labels: SEP=south eastern plateau, NWP=north western plateau, Zi=Ziquala volcano, Bk=Boku volcanic complex, Bs=Boseti volcano, TM=Tulumoye, G=Gedemsa, LZ=Lake Ziway, LK=Lake Koka. p1 and p2 are profile lines of modelling. Irregular polygon enclosed with white line denote the boundary of TMS.

Invoking geologic information provides a better constraint on the interpretation of the residual gravity anomaly map (Fig. 5.4). Most of the rift floor is covered with lacustrine sediment (low density) but the residual gravity anomaly map shows positive anomaly. Of course if we consider only information's from geology (Fig. 2.5) of the area, we may misinterpret the residual map. The residual gravity map consists the gravity response of geologic materials buried beneath at depths less than 20 km. This is approximately the thickness of the upper crust within the central MER. Our interpretation should consider not only the geological map (Fig. 2.5) of the area but also the regional stratigraphy (Table 2.1) and tectonic setting (Fig. 2.6) of the area. The rift floor is characterized by intense deformation and volcano-tectonic activity (Ebniger and Casey, 2006). The thickness of volcanic rocks may reach up to 5 km whereas the maximum thickness of the volcanics is 2 km in the rift flanks (Wolfenden et al., 2004).

Therefore, gravity maxima occurring over the MER floor in the residual map (Fig. 5.4) is attributed to be the response of thick volcanic rocks and magmatic addition to the upper crust (Keranen et al., 2004). On the contrary, the adjacent sides of the rift are generally characterized by gravity minima as magmatic addition and volcanism is less intense compared to the rift floor. Finally, short wavelength extreme gravity maxima superimposed on gravity maxima of the rift floor reflects the response of the volcanic centers and related volcanics.

5.1.2.3 Upward continuation of the residual gravity anomaly map

Figure 5.3 shows the trend of the regional gravity anomaly compiled by a subsequent upward continuation of the CBA map (Fig. 5.2). In this map, the response of magmatic segments is not clearly observed. This is likely because their gravity response could be masked by higher density deep seated regional bodies (either uplifted lower crust or upper mantle). Regional geophysical studies (Keranen et al., 2004) have shown that magmatic segments of the MER are the result of magmatic addition to the upper crust. The residual gravity anomaly map (Fig. 5.4) is the effect of causative bodies buried at depths less than 20 km which is the approximate thickness of the upper crust. Therefore, an insight on the extent, nature and depth of the Gedemsa TMS can be inferred from subsequent upward continuation of the residual gravity anomaly map. Figure 5.5 shows the upward continuation to 5 km, 10 km, 20 km and 30 km of the residual gravity anomaly map to see the nature of the TMS at 2.5 km, 5 km, 10 km and 15 km respectively.

Closely examining the individual grids in Figure 5.5 shows the suppression of shorter wavelengths resulting from shallower bodies and enhancement of longer wavelengths associated with effect of deep seated bodies. Continuation of the residual map to 5 km upward so as to see the sources of anomalies at 2.5 km beneath the surface reveals three sets of circularly shaped gravity maxima. Such gravity maxima's could be the reflection of the three volcanic centers within the WFB: Tulumoye-Gedemsa, Boku and Boseti from south to north. Further continuation up to 10 km, to see sources at 5 km beneath the surface, magnifies gravity maxima at the TMSs. The gravity response of Boku and Gedemsa observed as discrete anomaly maxima on the 0 km and 5 km upward continued residual anomaly map (Fig. 5.5). However, the NW and SE flanks of the rift are characterized by negative anomalies. Gravity response from very shallow causative bodies appears to disappear. In addition, 20 km upward

continuation of the residual anomaly results in too smooth signal response indicating that the long wavelength anomalies become dominant. This could be attributed to an increase in extent of the causative bodies occurring at approximately 10 km depth beneath the surface of the TMS and its environs.

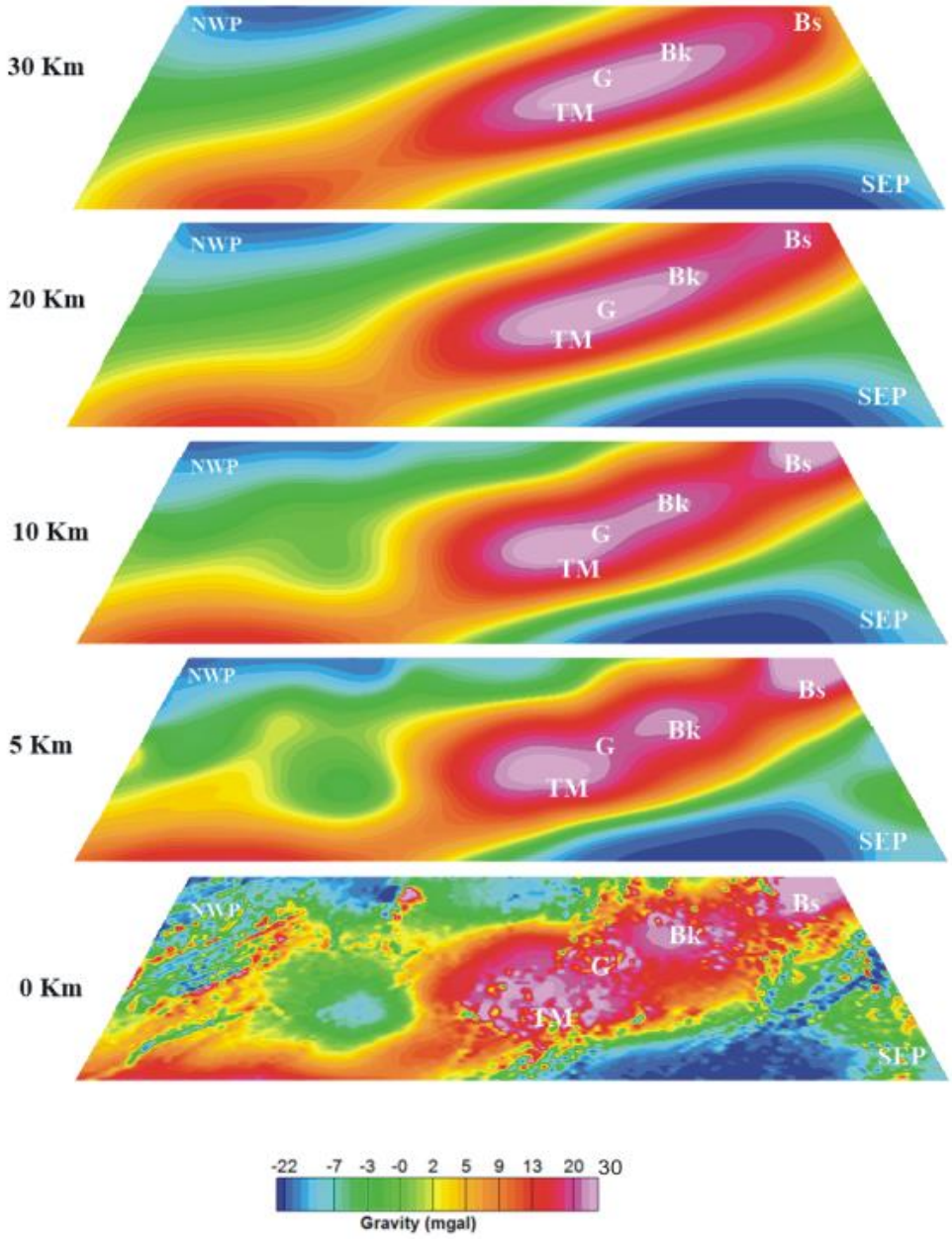

Figure 5.5 Upward continuation of the residual gravity map to a height of 2 km, 5 km, 10 km, 20 km, and 30 km. Labels: Bk=Boku, Bs=Boseti, TM=Tulumoye, G=Gedemsa NWP=North western plateau, SEP=South eastern plateau.

Gravity maxima beneath the Gedemsa and Boku volcanic centers merge to become a single anomaly peak for 20 km upward continuation. Interpretation of this phenomena needs Geochemical evidence to confirm the possibility of a single intrusion occurring at deeper depth. However, the possible geological suggestion for this gravity signal response could be: Additional supply of a melt from the lower to upper crust as a single intrusion may result in different magmatic chambers and volcanic centers at shallow depths through migration of melt following the WFB.

The most notable feature in Figure 5.5 is the decrease and increase in gravity maxima with depth beneath Boseti and Gedemsa TMSs respectively. The most plausible reason for such phenomena is that the magmatic addition beneath the former is at relatively shallower depth than the latter TMS. The above explanation does not apply to the regional trend of the gravity field which appears to increase towards Boseti TMS (Fig. 5.3). The 30 km upward continuation map (Fig. 5.5) shows the shift in gravity maxima towards the Gedemsa TMS where its probable upper interface could be thought to occur at a depth close to10 km. Three anomalous regions associated with sources occurring at a depth of 15 km (Fig. 5.5) are observed in the study area: Gravity maxima over the rift floor including the TMSs, gravity lows over the highlands and medium gravity anomalies over the rift floor excluding the TMSs.

5.1.3 Horizontal derivative gravity map

Prior to modelling of gravity data relevant information can be extracted from the gravity data itself using various filtering techniques (Tilahun Mammo, 2010). As demonstrated by Blakely and Simpson (1986), horizontal derivative (HDR) enables to locate the boundaries of near surface geologic bodies of contrasting density and can be expressed as:

$$\mathrm{HDR} = \mathrm{H(x,y)} = \sqrt{\left(\frac{\partial \Delta g}{\partial x}\right)^2 + \left(\frac{\partial \Delta g}{\partial y}\right)^2} \qquad (5.7)$$

It works based on the principle that the maximum horizontal gradient is caused by a planar anomalous body tends to overlie the edge of the body and vertical discontinuities.

In this work, the HDR map (Fig. 5.6) is constructed by applying the HDR filter to the gridded residual gravity anomaly map (Fig.5.4) in order to enhance and clearly demarcates the pattern of the tectonic relief of the area. In conjunction with the horizontal gradient filtering, 135^0 counter clockwise rotation has been applied for direction based enhancement purpose. A gravity discontinuity in the horizontal derivative is either structural or lithological

discontinuity. Accordingly, interpretation of the horizontal derivative gravity map (Fig. 5.6) needs to be correlated with the geology (Fig. 2.5) and structural set up (Fig. 2.6) of the area. The eastern margin of the MER is clearly reflected by continuous positive and negative gradients. This is attributed to be a structural discontinuity, mainly boundary faults, between the rift floor and the eastern flank of the rift. The western margin of the rift is also highlighted with MKSH as SW-NE striking feature which is replaced by SDFZ further to the east. The rift floor is characterized by intermediate gradient value in the HDR (Fig. 5.6) resulting from the lacustrine sediment without abundance faults (planar bodies). On the other hands, the volcanic complexes (Boku, Gedemsa and Tulumoye) are characterized by negative and positive gradients which reflects the quaternary volcanics affected by faults and fractures.

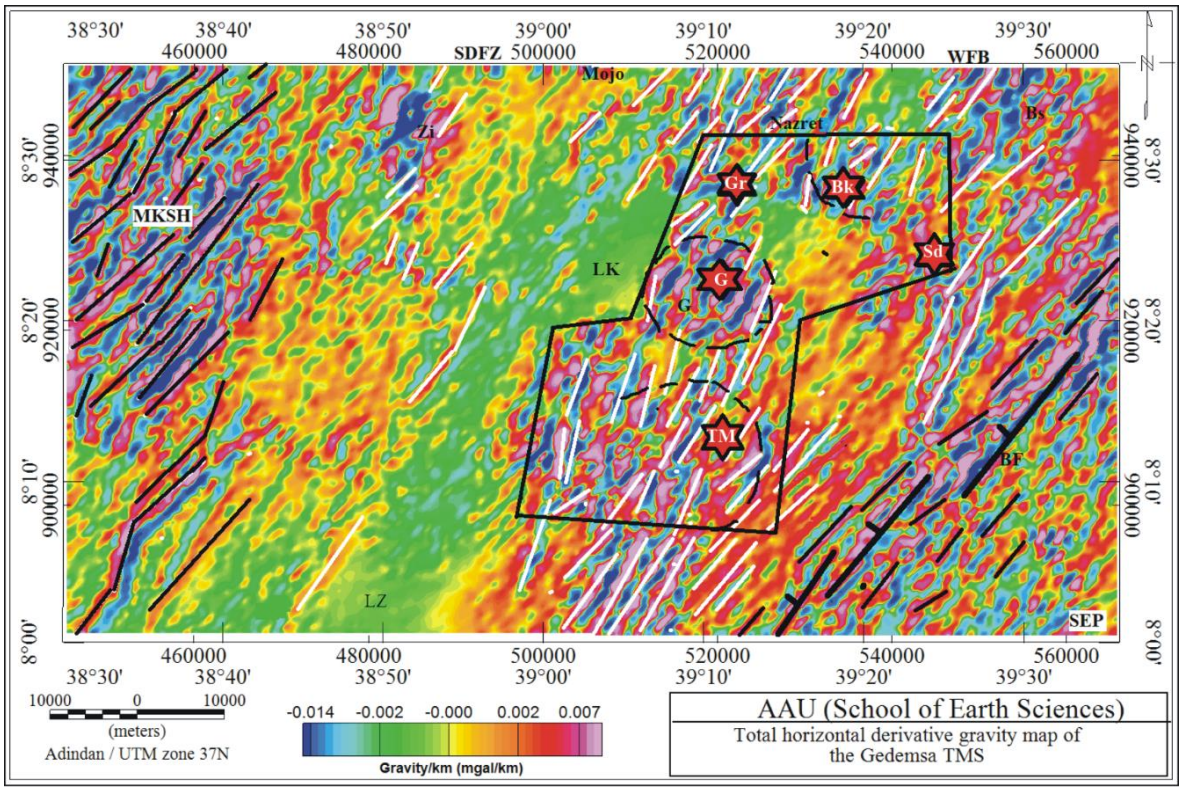

Figure 5.6 Horizontal derivative map rotated 135^0 ccw. Labels: MKSH=Midre Kebd structural High, SEP=Southeastern plateau, BF=major boundary fault, LZ=lake Ziway, LK=lake Koka, the star's field with red colors are geothermal prospect sites (TM=Tulumoye, G=Gedemsa, Gr=Geregendi, Bk=Boku, Bs=Boseti and Sd=Soderie). The polygon enclosed with black line is the geothermal prospect area. The black lines represent the border faults and the white lines indicate the WFB and SDZFZ.

The alignment of thermal springs and geothermal prospect zones following the WFB (Fig. 5.6) implies that thermal resources within the MER are highly linked to and controlled by rift structures (Engdawork Admasu and Selamawit Worku, 2015). Combined with geological and structural studies (Boccaletti, 1999; Corti, 2009; Engdawork Admasu and Selamawit Worku, 2015), the horizontal derivative map (Fig. 5.6) significantly contributes with regard to mapping geologic structures favoring the occurrence of geothermal resources. Most of the geothermal prospects within the central sector of the MER are related to the central rift volcanoes (Tulumoye, Gedemsa and Boku). However, there are also thermal spring manifestation zones which occur far from the central volcanoes: Geregendi thermal spring is a classic example which is supposed to get its heat source from its nearby caldera (Gedemsa) through subsurface weak zones related to quaternary faults of the WFB.

The quaternary NE to NNE faults and fractures within the floor of the rift (WFB and SDFZ) are clearly mapped (revealed) by their gravity response in the HDR map (lines in white color, Fig. 5.6). Closely examining the orientation and interaction of these structures with the volcanic centers provides a key constraint on the occurrence of potential geologic sources associated with geothermal resources. The border faults in the SE flanks of the rift and the MKSH (western rift margin) are characterized by elongated NE oriented responses in the HDR map (Fig. 5.6).

5.1.4 Analytical Signal gravity map

Analytical signal (AS) or total derivative is a powerful technique of interpretation in potential field data (Dentith and Mudges, 2014). According to Dentith and Mudges (2014), the AS enhances the effect of shallow seated source bodies at the expense of the effect of deep seated bodies. In addition, it highlights the edge of source bodies and geologic contacts. The amplitude (A) of AS is expressed mathematically as:

$$\mathrm{A}(\mathrm{x},\mathrm{y}) = \sqrt{(\frac{\partial \Delta g}{\partial x})^2 + (\frac{\partial \Delta g}{\partial y})^2 + (\frac{\partial \Delta g}{\partial z})^2} \qquad (5.8)$$

The purpose of constructing AS map (Fig. 5.7) is to make the HDR map (Fig. 5.6) more informative through capturing gradients in all directions, further enhancing detection of geologic boundaries and structures. The discontinuity in the AS gravity map is highly correlated with the geological boundaries (Fig. 2.5). Consequently, interpretation of the AS map (Fig. 5.7) has been made in conjunction with the geological map (Fig. 2.5) of the area.

The maximum gradient in the AS map (Fig. 5.7) shows the source body and geologic contacts. In the Analytical signal map (Fig. 5.7), the effect of shallow seated bodies is enhanced.

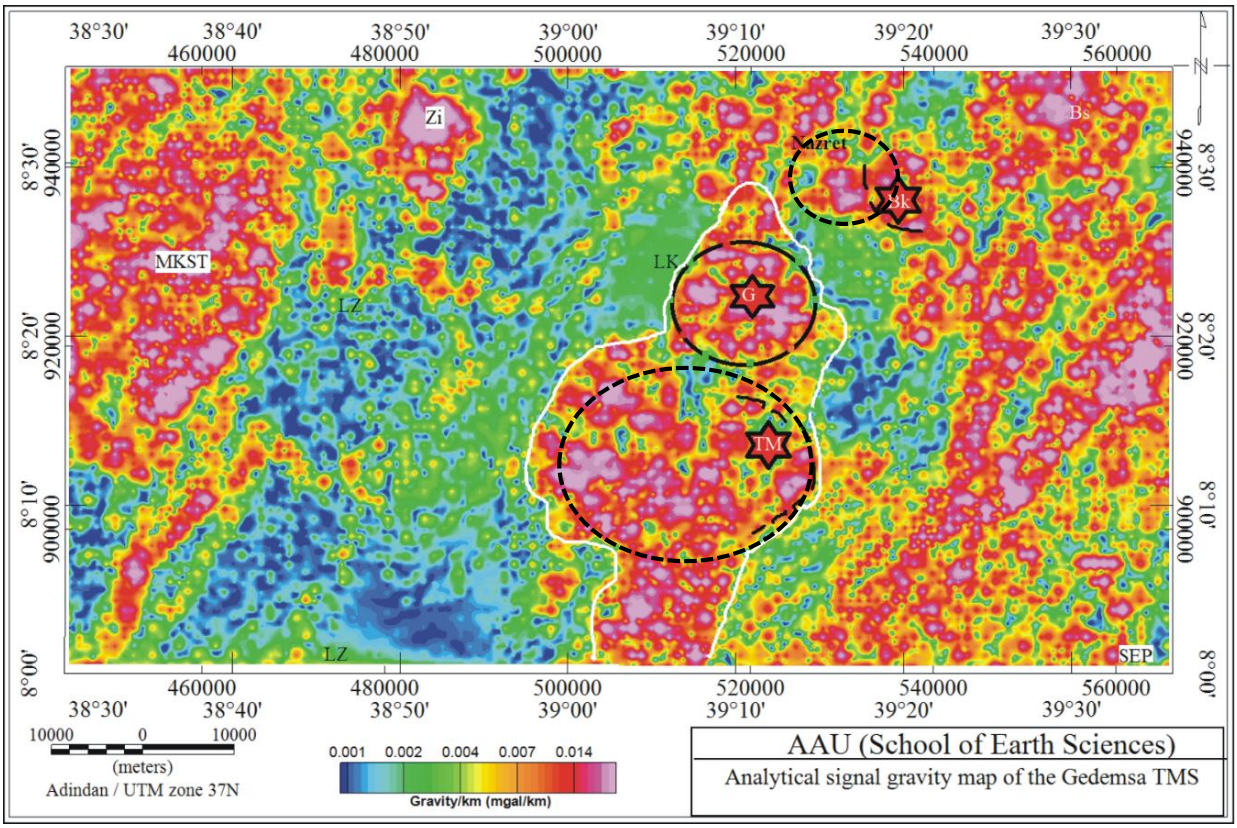

Figure 5.7 Analytical signal gravity map. Labels: MKSH= Midre Kebd structural high, SEP= Southeastern plateau, LZ=lake Ziway, LK=lake Koka, the star's field with red colors are geothermal prospect sites (TM=Tulumoye, G=Gedemsa and Bk=Boku), Bs=Boseti, Zi=Ziquala volcano, the polygon enclosed with white line shows the Gedemsa TMS. The circular polygons with black broken line represents the expected caldera.

The Gedemsa TMS (polygon enclosed with white line, Fig. 5.7) is characterized by a cumulate of maximum gradients in the analytical signal map. This is because the quaternary volcanics covering the TMS is denser than the surrounding equivalent rift floor quaternary sediments. In this regard, the AS map (Fig 5.7) reasonably agrees with the geological map (Fig. 2.5) of the area as the lithological discontinuities are clearly reflected by gravity signal discontinuities. The lacustrine sediments extensively cover the largest portion of the geological map especially at the western margin of the rift following the western part of the Gedemsa TMS. The area covered by this lithology is characterized by low values in the AS (Fig. 5.7) whereas the volcanic rocks both in the rift floor and its flanks are characterized by low gradients. Alkaline

basalts, Gash Megal rhyolite and welded pyroclastics in the SE flank and west ward to the western margins of the rift are reflected by a maximum gradient in the AS map. The rift floor volcanic centers (Gedemsa, Tulumoye, Boku and Boseti) and off rift regions (Ziquala and Chilalo volcano) are reflected by circular shaped gradient maxima in the AS.

5.1.5 Tilt derivative gravity map

Edge detection in gravity data is a common technique of interpretation where faults and fractures with a significant density contrast can be detected (Putri et al., 2019). Adequate information on edges of structural bodies can be obtained by a potential field data filtering technique called Tilt derivative (TDR). According to Miller and Singh (1994), TDR normalizes the vertical derivative by the horizontal derivative and uses the zero-point (zero-crossing) location to approximate the edge of the causative geological bodies. The mathematical computation of the filter for tilt derivative can be expressed as:

$$\mathrm{TA}\,(\mathrm{x},\mathrm{y}) = tan^{-1}\left[\frac{\frac{\partial \Delta g}{\partial z}}{\left[(\frac{\partial \Delta g}{\partial x})^2+(\frac{\partial \Delta g}{\partial x})^2\right]^{1/2}}\right] = tan^{-1}\left[\frac{VDR}{THDR}\right] \qquad (5.9)$$

Where, *VDR*=vertical derivative *THDR*=total horizontal derivative (Miller and Singh, 1994).

Tilt derivative (TDR) value is positive for source body, zero for the edge next to the source, and negative for other responses. The edge of the source can be fault, dip, and rock density contrast (Putri et al., 2019). TDR is based on the ratio of the derivatives in Equation 5.9 and it enhances both short and long wavelength anomalies, lithological boundaries as well as fault locations. Consequently, the TDR map (Fig. 5.8) is more detail than the residual map (Fig. 5.4) and the AS map (Fig. 5.7) as the former enhances both short and long wavelength anomalies simultaneously. The legend provided by the color scale assists to identify the boundary (edge) of source bodies in such a way that the red, yellow, green to blue-black colors represents the source body, edge and the outside source bodies respectively.

Figure 5.8 shows the location of SW-NE, SSW-NNE and N-S striking faults which are the orientation of boundary faults or WFB respectively (yellow colors). The SE-NW (west of Tulumoye) oriented fault structures are also detected which are not clearly delineated in the HDR and AS techniques. These NW-SE structures represent cross rift structures especially at the location of quaternary volcanoes as reported by Corti (2009). The difficulty in HDR (Fig.

5.6) and AS (Fig. 5.7) gravity maps is to identify the lithological and structural discontinuity at the same time, the additional advantage in TDR technique of interpretation (Fig. 5.8).

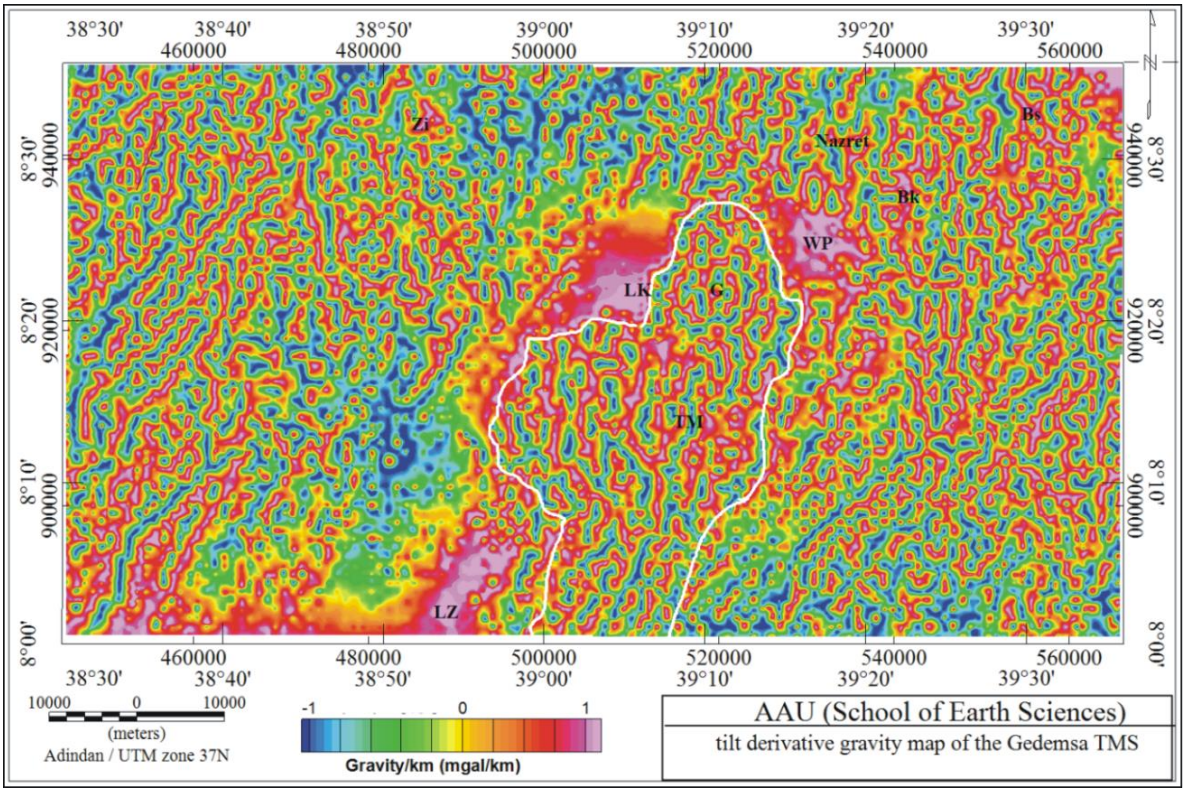

Figure 5.8 Tilt derivative gravity map of the Gedemsa TMS and its environs. Labels: LZ=lake Ziway, LK=lake Koka, TM=Tulumoye, G=Gedemsa, Bk=Boku, Bs=Boseti, Zi=Ziquala volcano, WP=Wonji plantations the polygons enclosed with the white line demarcate the Gedemsa TMS.

According to Putri et al. (2019), TDR sharpens the peak of gravity anomalies and widens weak anomalies signal, an effective way in localizing the deep sources. The area at Wonji, Lake Koka and SW of Gedemsa are characterized by minima in the AS (Fig. 5.7) and maxima in the TDR (Fig. 5.7) map. This is due to the fact that the former method enhances shallow seated bodies and the latter enhances both deep and shallow seated bodies.

5.1.6 Band pass filtered gravity map

The residual magnetic anomaly map (Fig. 5.4) is limited in that it contains the total effect of geologic bodies buried beneath the upper 20 km depth of the crust. As a result, the effect of shallow seated low density bodies is masked by deep seated high density bodies response. This

results an ambiguity in the interpretation of the gravity field response with respect to the geology of the area. Band pass filtering is a powerful tool to examine the gravity response of geologic bodies with in specific depth ranges. The band pass filtered gravity anomaly map (Fig. 5.9) of the Gedemsa TMS and its environs is compiled by applying band pass filtering on the CBA grid with shorter and longer wavelengths of 0.5 km and 48 km respectively.

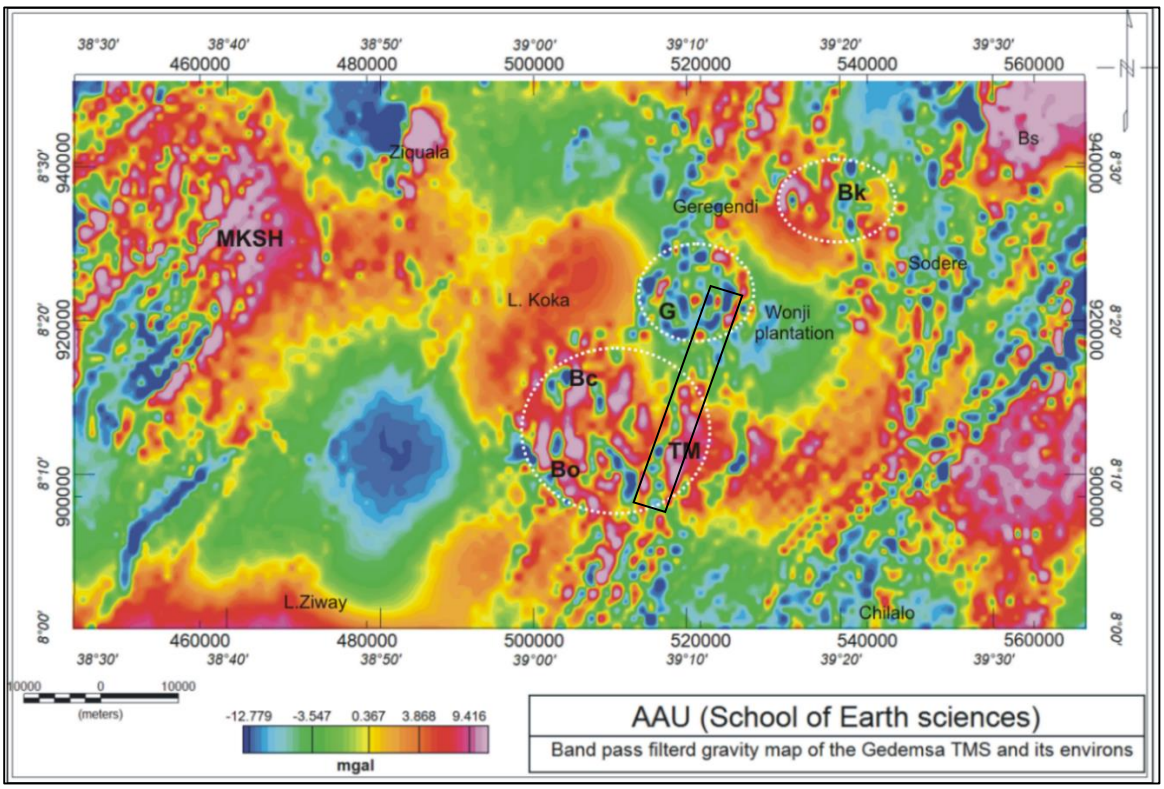

Figure 5.9 Band pass filtered gravity map of the Gedemsa TMS and its environs compiled by applying band pass filtering where wavelength between 0.5 km and 48 km are passed. Labels: TM=Tulumoye, G=Gedemsa, Bk= Boku, Bs= Boseti. The circular polygon with white broken line denote expected calderas. The rectangular polygon is the Salen range.

The band pass filtered gravity anomaly map (Fig. 5.9) is attributed to reveal the gravity signal response of geologic bodies buried within an approximate depth range of 0.125-12 km of the upper crust. The gravity response in the band pass filtered map (Fig. 5.9) is highly correlated with the geology (Fig. 2.5) of the area. The volcanic rocks at the rift flanks (MKSH, Chilalo and Ziquala) and volcanic complexes (Tulumoye, Boku and Boseti) are characterized by positive gravity responses. However, the lacustrine sediments over the floor of the rift (North of lake Ziway, Wonji plantation, north of Boku) are characterized by negative gravity

responses. The boundary faults and the rift floor quaternary faults are demarcated by elongated negative anomalies parallel to the rift axis (Fig. 5.9).

The SW-NE aligned rectangular polygon with black line shows the tectonic and structural setup of Salen range within the Tulumoye-Gedemsa volcanic complex. It is the most active volcano-tectonic segment in the area which is replaced by Boku volcanic complex further north (Birba and Varlet, 2018). Geologic studies (e.g. Birba and Varlet, 2018) reported the presence of persistent magmatic heat sources along this presently reactivating volcano-tectonic segment. Continuous gravity minima following the Salen range reveals the extensional fractures and faults within this tectonically active zone. On the other hand, local gravity lows at this spreading and diking segment could be attributed to the presence of thermal zones which are reflected by their low density contrast with the surrounding rocks.

5.1.6 Euler Deconvolution gravity map

The most universal application of potential field methods has been to determine the depth to the top of the geologic sources that produce observed anomalies. Towards this end, an attempt has been done to estimate the sources depth, nature and location of causative bodies beneath the study area using a mathematically established procedure (Thompson, 1982) known as Euler Deconvolution (ED). It works based on the rate of change of gravity field with distance. For an anomalous 3D geologic body buried at a point p (x_o, y_o, z_o), the Euler homogeneity equation (ED) at the surface of point Q (x, y, and z) is given by:

$$(x - x_o)\frac{\partial g}{\partial x} + (y - y_o)\frac{\partial g}{\partial y} + (z - z_o)\frac{\partial g}{\partial z} = N(\Delta g - \beta) \qquad (5.10)$$

where β=regional gravity value, N=structural index (SI) which is the degree of homogeneity of the anomalous source known as measure of the rate change with distance of a potential field.

Table 5.1 gravity and magnetic structural index for different source geometries (Reynolds, 1997)

Geological model	No of infinite dimension	Magnetic SI	Gravity SI
Sphere	0	3	2
Pipe	1 (z)	2	1
Horizontal cylinder	1 (x or y)	2	1
Dyke	2 (z and x or y)	1	0
Sill	2 (x and y)	1	0
contact	3 (x, y and z)	0	NA

The source location p (x_o, y_o, z_o) and the regional gravity anomaly (β) can be computed by observing four or more neighboring observations concurrently (Thompson, 1982). Structural index (SI) specification permits the equation to be solved for specific source location of specific field (Table 5.1). Choosing SI should be done using prior knowledge of source geometry. ED outline different geologic structures generating the residual anomalies in both gravity and magnetic surveys (Table 5.1). Depth estimation for various anomaly sources of the Gedemsa TMS and its environs has been made using the ED interpretation. In this thesis, Euler 3D deconvolution map (Fig. 5.10) has been compiled from the residual gravity maps using the oasis montaj software. The map informs us the spatial distribution (longitude, latitude), nature and depth of the causative bodies with in the study area. SI values of 2 (Fig. 5.10) which represent a sphere in case of gravity were chosen after Visual inspection of clustering of depth solution for several depth solutions.

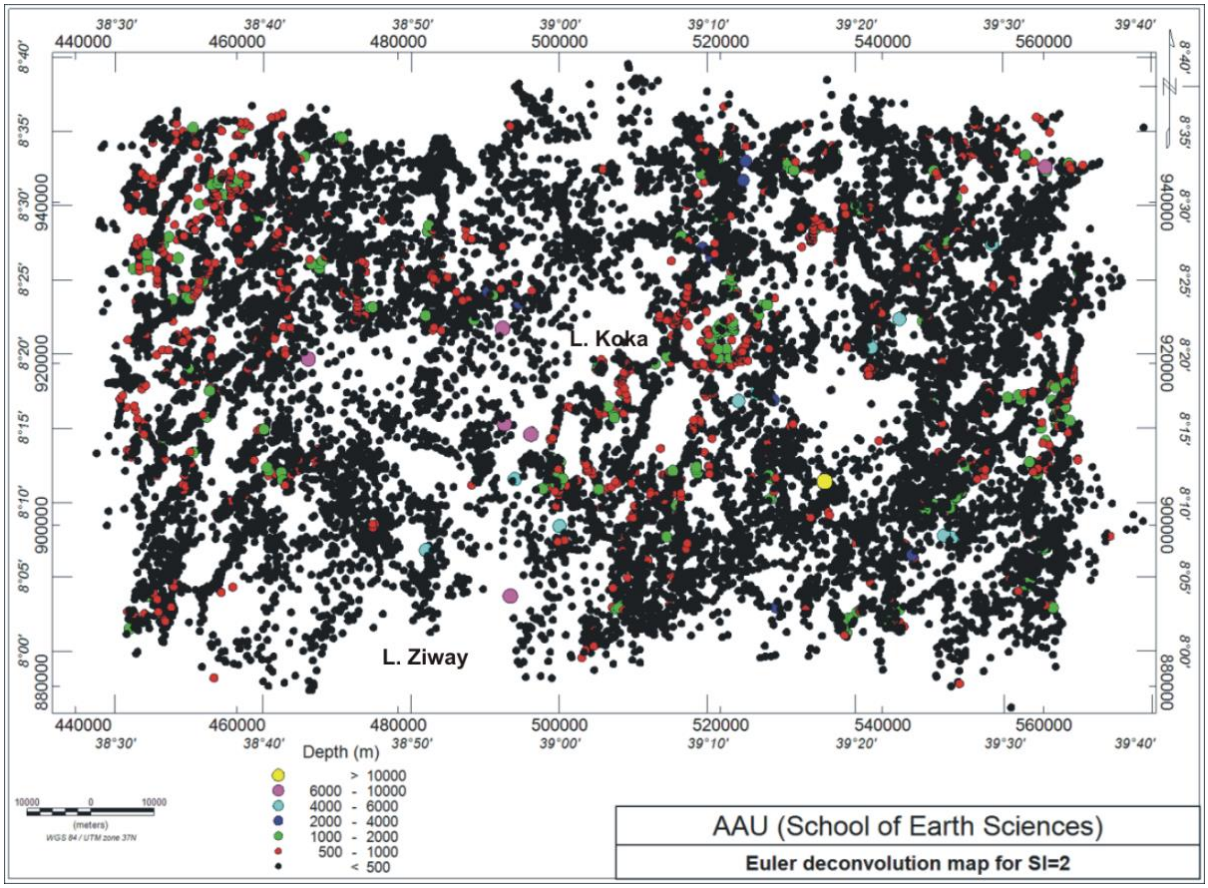

Figure 5.10 Euler deconvolution map of the study area for SI=2.

Figure 5.10 shows the depth solutions of spherical bodies with structural index of 2. There is no solution for source bodies with depth greater than 10 km (yellow color) except near the

eastern rift margin. This is because the occurrence of 3D geologic bodies at this great depth is mostly unlikely due to unbalanced geopressure and extensional stress effects. However, the occurrence of 3D geologic bodies at depth 6-10 km (purple) is detected within the rift floor close to the western margin and eastern margin. There is no similar solution for source bodies at this depth range beneath the Gedemsa TMS. This is a good evidence for the volcanic complex of the Tulumoye-Gedemsa-Boku region in such a way that their magma chambers should be shallower than 6 km. Between 4-6 km (blue color) the effect of such bodies is detected at the Tulumoye-Gedemsa volcanic complex and eastern margin. At depth ranges of 2-4 km (blue black color), spherical bodies exist at the northern termination of the Gedemsa TMS and western rift margin. It is interesting that the Tulumoye Gedemsa region is characterized with 1-2 km and 0.5-1km 3D geologic bodies. This is supported by the band pass filtered gravity map (Fig. 5.9) which shows the occurrence of abundance discrete circularly shaped gravity lows at Gedemsa and Tulumoye. This could be attributed to shallow magma chambers which results multi-vents within the floor of the larger calderas which is an attractive target from geothermal resource exploration point of view.

5.2 Magnetic data result, analysis and interpretation

The Magnetic survey of this study was conducted to identify anomalous regions within the shallow crust of the study area which assist and support the interpretation of the gravity data. This can be achieved through interpretation of the magnetic signal response within the context of lithological and structural contacts and anomalously hot areas. Interpretation of magnetic data in equatorial areas is an ambiguous as smaller field intensity and horizontally directed ambient inducing field produces several complications (Beard et al., 2000).

According to Beard et al. (2000), magnetic anomalies over magnetically susceptible bodies tend to be negative instead of positive. In addition, long north-south striking structures can be magnetically invisible, except where the structures are broken or terminate. However, an ambiguity in interpretation of magnetic data can be precluded (Beard et al., 2000; Lingerew Nebere, 2015) using appropriate data enhancement techniques: Either enhancing features associated with depth (wave length filtering, continuation and trend analysis) or locations (reduction to the pole). All the magnetic data processing of the present study has been done using Oasis montaj software (version 8.4). The MER is located near the magnetic equator

where interpretation of magnetic data is much more difficult. To avoid this ambiguity, all of the magnetic anomaly maps in the present study were generated after applying reduction to pole (RTP) data enhancement technique on the observed total magnetic anomaly. In addition, analytical signal, tilt derivative and upward continuation enhancement techniques were applied to the observed total magnetic anomaly in order to assist and reduce the ambiguity in the interpretation of the magnetic data considered in this study.

5.2.1 Reduction to the pole of the magnetic anomalies

Due to the dipolar nature of the geomagnetic field, magnetic anomalies observed anywhere rather than the magnetic poles are asymmetric (Ansari and Alamdar, 2009). This property complicates the interpretation of magnetic data and the problem is worse for magnetic inclinations within 20 north and south of the magnetic equator (Rajagopalan, 2003). Reduction to the pole (RTP) is a technique that converts magnetic anomaly to symmetrical pattern which would have been observed with vertical magnetization. It reduces dipole filed of equatorial region anomalies to monopole field by translating the magnetic anomaly directly above the causative body as gravity (Yaogauo and Oldenberg, 2001). RTP operator is expressed as:

$$L(\theta) = \frac{1}{[\sin(I) + icos(I)\cos(D-\theta)^2]} \tag{5.11}$$

Where, θ is the wave number direction D=Declination and *I* is the inclination

The processed magnetic data in this study has been reduced to the magnetic pole to avoid complications involved in the interpretation of the magnetic data. The reduction to pole filtering operation of this work has been made using an average inclination and declination of 0.3^0, and 1.94^0 as well as an amplitude correction inclination of 1.94^0. In the present study, interpretation of the magnetic data has been made by considering as if we observe the subsurface of the area at the magnetic pole.

5.2.1 The total magnetic intensity map

The total magnetic intensity (TMI) map (Fig. 5.11) is generated by plotting all the magnetic data points which were corrected for diurnal variation. Figure 5.11 shows the spatial distribution of the magnetic data points superimposed on the variation in intensity of magnetization with in the area. The map is supposed to shows the combined effect of rock magnetization and dipole field of the Tulumoye-Gedemsa volcanic complex. The area is local

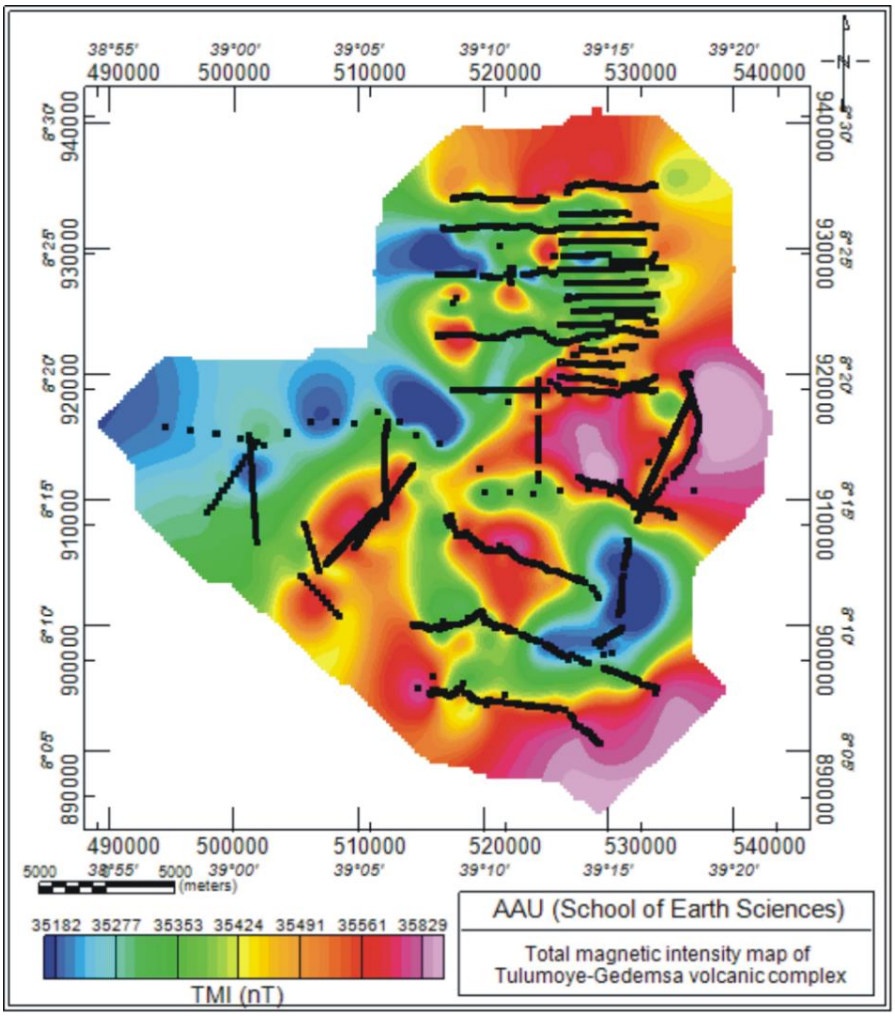

Figure 5.11 Total magnetic intensity map of the Tulumoye Gedemsa-volcanic complex. The black dots represent the geographic distribution of the magnetic data.

scale so that the geology of the area results a significant variation in the TMI map (Fig. 5.11) of the area than the dipole field (IGRF value) effect. Accordingly, three magnetic intensity regions can be identified on closely examining the TMI map of the area: 1) Low magnetic intensity responses (up to 35000 nT) at the west and north west of the area; 2) Intermediate magnetic intensity response (35400 nT) at the central part of the area and 3) High magnetic intensity response (up to 35800 nT) are observed at the southern and eastern part of the area.

From geologic point of view it is known that the thickness of lacustrine sediments increase towards the rift axis (west and north west of the area). Therefore, the low magnetic response could be associated with this thick accumulation of sediments with in the west and northwest of the area. On the contrary, the high magnetic response within the eastern and southeastern

part of the area can be associated with shallow depth basements covered by quaternary volcanics. However, to interpret the magnetic data confidently interms of geology, it is better to isolate the effect of dipole field from rock magnetization.

5.2.2 The total magnetic anomaly map

The total magnetic anomaly (TMA) map (Fig. 5.12) of the area is compiled by removing the dipole field from the total magnetic intensity by IGRF correction using oasis montaj software (version 8.4). The IGRF value of the area has been obtained automatically using oasis montaj software. Figure 5.12 contains the response in rock magnetization of the area generated after

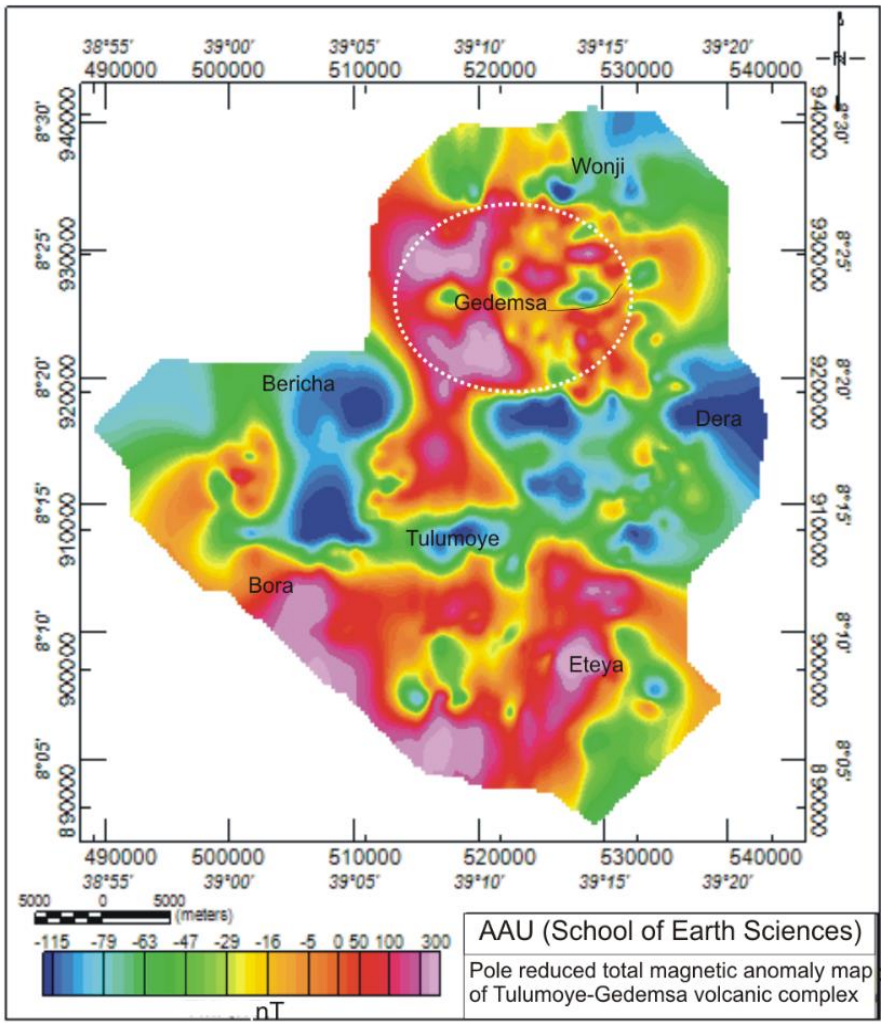

Figure 5.12 Total magnetic anomaly map of the Tulumoye Gedemsa-volcanic complex. The elliptical shaped polygon enclosed with white broken line is the Gedemsa caldera.

applying RTP filtering to the TMA grid that precludes the effect of the IGRF field. Rock magnetization occurs up to an approximate depth of 20 km within the crust where rocks lose their magnetization below this depth (considering the effect of geothermal gradient, 30 ^{0}C/km). This is approximately the same as the thickness of the upper crust within the MER.

Examining the TMA map (Fig. 5.12) of Tulumoye-Gedemsa volcanic complex reflects the presence of prominent magnetic lows (as low as -115 nT) and highs (up to 300 nT) in different parts of the area. The southern part of the area including Bora volcano is characterized by positive magnetic anomaly. In addition, Gedemsa volcano and its surrounding is also demarcated by positive total magnetic anomaly. This can be attributed to the response of thick accumulation of volcanic rocks close to the volcanic centers. The Volcanic centers (Gedemsa, Bora and Tulumoye) are characterized by succession of pyroclastics with interbedded basaltic flows, scoria fallout and peralkaline rhyolite (Fig. 2.5) which results positive magnetic anomaly complicates interpretation of the pole reduced TMA map (Fig. 5.12). The eastern part of Bericha and Tulumoye volcanic complex as well as Dera area is characterized by negative magnetic anomaly. This can be attributed to the presence of thick lacustrine sediments (Fig. 2.5). Figure 5.12 reveals the combined effect of shallow and deep seated causative bodies beneath the study area. Separating the effects of shallow and deep seated causative bodies based on their respective wavelengths is attempted here to map the subsurface geological and structural units of the study area.

5.2.3 The regional magnetic anomaly map

Isolating the effect of deep seated bodies with an appropriate filtering technique provide relevant information associated with the regional structural setup of the area. In this regard, the regional magnetic anomaly (Fig. 5.13) map has been compiled by applying Gaussian regional residual separation technique of low pass filter with cutoff wavelength of 30 km. The regional magnetic anomaly map (Fig. 5.13) reflects the spatial distribution in magnetization of rocks buried at depths less than 7 km beneath the surface of the Tulumoye-Gedemsa volcanic complex. It shows a magnetization contrast forming a banding feature which reflects the presence of prominent variation in composition of the subsurface geology. High magnetic anomaly response is observed at the Gedemsa volcano and in the southern part of the area. The central and northeastern part of the area is characterized by intermediate magnetic anomaly.

Eastern part of Bericha volcanic complex, Dera area and the northeastern part of the area is reflected by negative magnetic responses. Since the data is reduced to the magnetic pole,

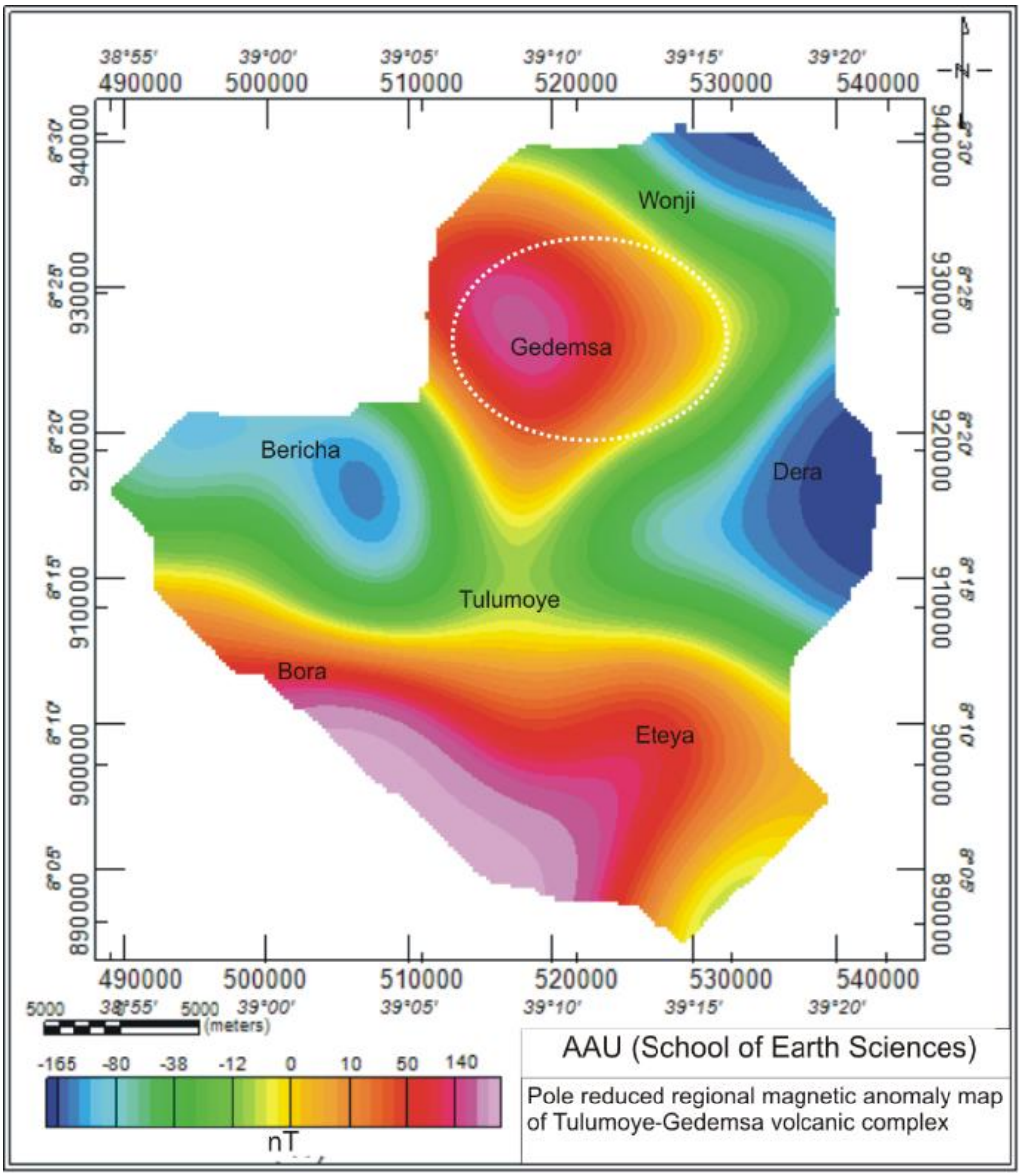

Figure 5.13 Regional magnetic anomaly maps of the Tulumoye Gedemsa-volcanic complex.

positive anomalies could be a response of magnetically high susceptible bodies. On the contrary, loss of magnetization due to the anticipated increase in temperature with depth could result in negative magnetic anomalies. The most notable feature of this map is the circular negative anomaly further east of the Bericha complex which could be a reflection of demagnetization of rock materials due to heat source. Basement rocks without significant thermal effect may result anomaly responses observed over the southern and southwestern

parts of the study area (Fig. 5.13). Interpretation of the circularly shaped deeper root positive magnetic response at Gedemsa volcano needs to consider the geological setup and previous geologic evidences. We expect negative magnetic response beneath an active volcano but it is the opposite case in Gedemsa. The positive magnetic response over the Gedemsa volcano might be an indication that it is a dormant/extinct volcano. But this inference needs supportive geochemical and volcanological evidences to constrain this ambiguity.

5.2.4 The residual magnetic anomaly map

The residual magnetic anomaly map (Fig. 5.14) of this study has been compiled after subtracting the regional magnetic anomaly grid from the total magnetic anomaly grid. The interpretation of the residual anomaly has been made after RTP filtering which makes the anomaly peaks to occur directly above the causative bodies as in the case of gravity data interpretation. Geological information (Section 2.2.5) of the area is the most optimal assistance in the interpretation of the residual magnetic anomaly map. Figure 5.14 displays the magnetic response of the shallow subsurface in the Tulumoye-Gedemsa volcanic complex (approximately less than 7 km) with prominent spatial magnetic anomaly variation. The anomaly variation (from -170 to 200 nT) in the residual magnetic anomaly map (Fig. 5.14) could be primarily due to the effect of variation in geology and buried intrusions/shallow magma chambers at shallow depths.

The linear positive magnetic anomaly trend observed north of the Tulumoye volcano (Fig. 5.14) could be the response (up to 180 nT) of scoria fallout observed on the geologic map (Fig. 2.5). The scoria fallout has a higher magnetic susceptibility contrast than the surrounding rock units which consist of obsidian, pyroclastic and pumice fallout. Similarly, local magnetic lows observed east of Eteya could be a responses of alluvium, soil, fluvial, colluvium, slope scree and debris deposits occur as caldera, crater as well as graben floor fillings having lower magnetic susceptibility values. This rock unit is also characterized similarly at NE of Wonji plantation and Dera regions with Lacustrine sediments as a surrounding rock units. The Bofa basalts and scoria fallout observed SE of the Gedemsa volcano on the geologic map are reflected by high magnetic anomaly values. The lacustrine sediments and alluvium deposits are reflected by magnetic anomaly lows (up to -170 nT) (Fig. 5.14). The Caldera floors (e.g. Gedemsa) are also characterized by both negative and positive anomaly responses as they

contain low susceptibility reworked materials with lacustrine sediments and exposed lithologic units respectively. However, very high magnetic response at the western margin of the Gedemsa volcano could be a response of peralkaline rhyolite. Pyroclastic lava flows at Bora volcano reflects high magnetic anomaly (Fig. 5.14). Magnetic lows occurring east of Bericha volcanic center are attributed to be the response of low susceptibility pumice and obsidian lava flows and domes. Porphyritic rhyolite lava flows and domes at the Eteya locality reflect high magnetic anomaly responses.

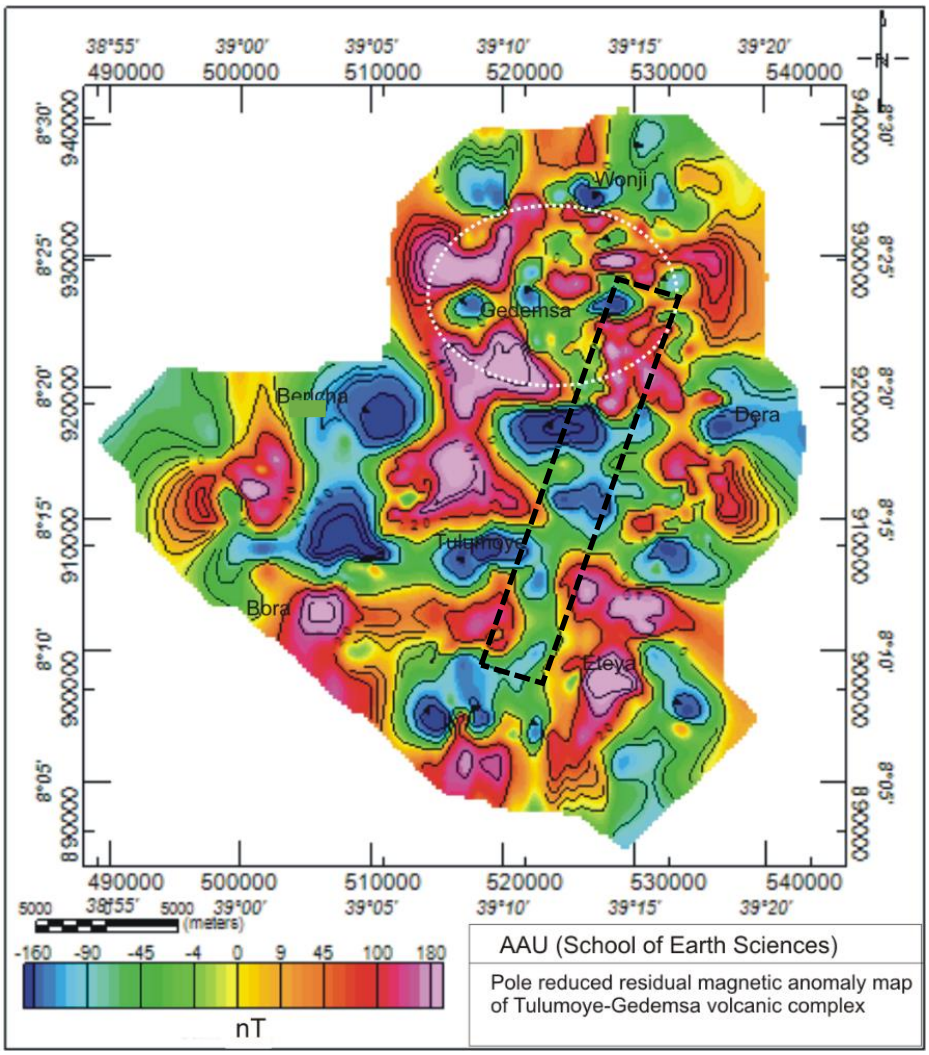

Figure 5.14 residual magnetic anomaly map of Tulumoye-Gedemsa volcanic complex. The circularly shaped polygon with white broken line represent the Gedemsa volcano and the NE-SW aligned rectangular polygon represents the Salen range.

The residual magnetic anomaly map (Fig. 5.14) reflects a SW-NE aligned minima following

the Salen range. These magnetic lows following this active volcano-tectonic range represent intensive or thick hydrothermally demagnetized geologic units due to heat treatment. It is known that, hydrothermally demagnetized rocks have a negative susceptibility contrast with respect to the surrounding volcanic rocks.

5.2.5 Upward continuation map of the residual magnetic anomaly

The Upward continuation map (Fig. 5.15) of the residual magnetic anomaly is compiled by applying upward continuation filter on the residual magnetic anomaly grid. The pole reduced residual magnetic field map (Fig. 5.14) consists of the combined effects of causative bodies buried within a depth of less than 7 km. However, to understand the structure of the subsurface at which the causative bodies could occur it would be better to investigate the subsurface at discrete depths. Figure 5.15 shows the upward continuation of the residual magnetic anomaly grid to 2 km, 4 km and 8 km to image the subsurface at the corresponding depth of 1 km, 2 km and 4 km respectively.

Comparison of the pole reduced residual magnetic anomaly map (Fig. 5.14) and its upward continuation to 2 km map (Fig. 5.15) reveals removal of the short wavelength anomalies and enhancement of the long wavelength anomalies in the latter irrespective of their sign (either positive or negative anomalies). The effect of shallow source bodies such as the reworked materials on caldera floors and small volcanic centers within the larger caldera (e.g. Gedemsa caldera) disappears. Upward continuation of the observation point to 4 km in order to see the effect of the causative bodies occurring at 2 km depth below the surface further enhances the long wavelength anomalies by suppressing the effect of the shallower bodies. Upward continuation of the field further to 8 km upward to see the effect of the sources buried at 4 km reveals the extreme suppression of shorter wavelength anomalies at the expense of a progressive enhancement of the longer wavelength anomalies (irrespective of their sign).

Generally, Figure 5.15 provides an important insight on the spatial location, lateral extent and depth of the source bodies within the volcanic complex. Separate magnetic low peaks (e.g. east of Bericha volcanic complex) and high peaks (e.g. western flank of Gedemsa volcano) are merged to a single anomaly peak through subsequent upward continuation filtering. Looking at the 8 km upward continued anomaly map (Fig. 5.15) in detail shows three regions of magnetic maxima: Gedemsa Caldera, Bora volcanic center and the eastern part of Tulumoye.

On the contrary, the southern end of Lake Koka, the North eastern and the central eastern ends of the area are characterized by magnetic lows which are likely to be the effects of relatively deeper sources. The remaining part of the area within the Tulumoye-Gedemsa volcanic complex is characterized by intermediate magnetic responses.

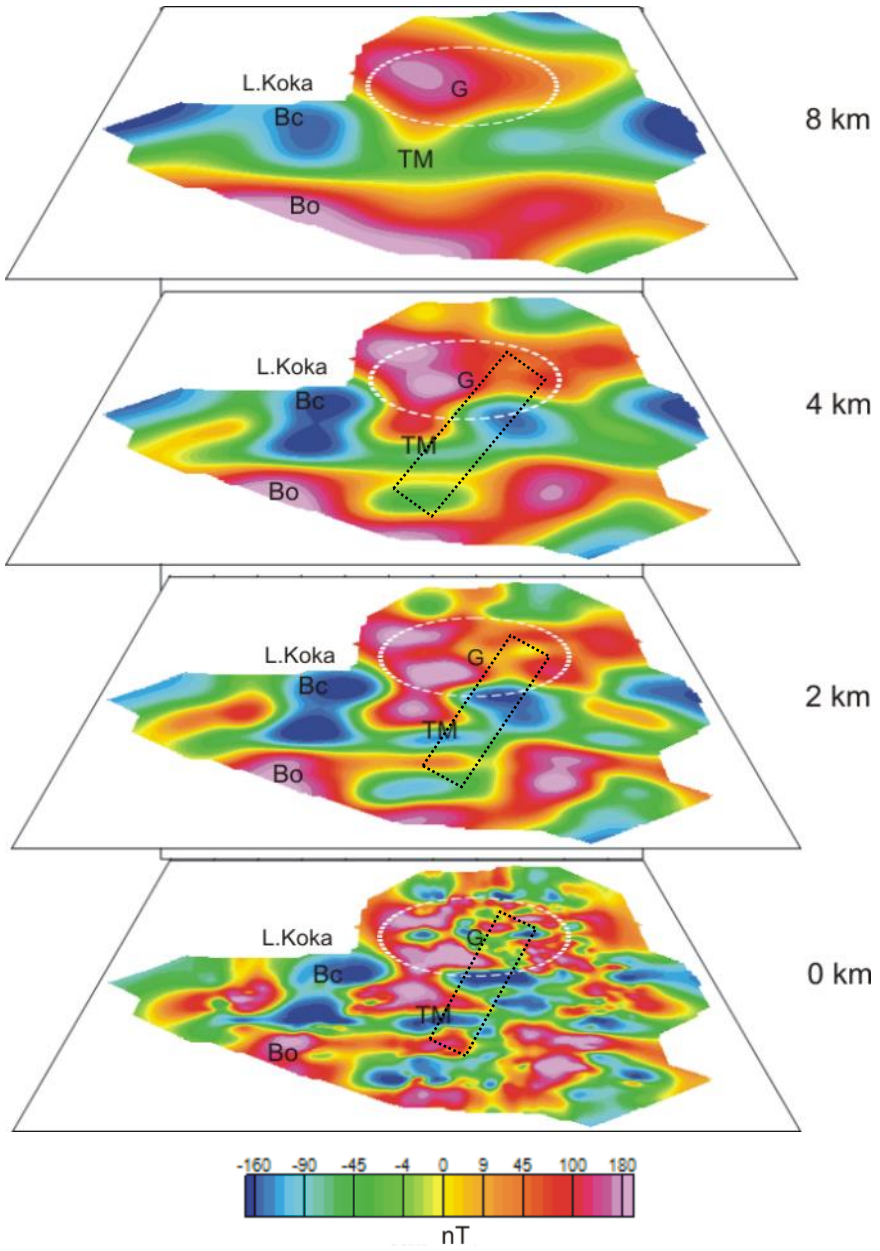

Figure 5.15 upward continuation of the residual magnetic anomaly map to 2 km, 4 km and 8 km. Labels: G=Gedemsa, TM=Tulumoye, Bo=Bora, Bc=Bericha. The rectangle with black broken line is the Salen range. The circle with dashed white line is the Gedemsa caldera.

The Salen range is demarcated by SW-NE magnetic lows in the upward continuation map (Fig. 5.15). Subsequent upward continuation for different continuation distances reflects the disappearance in short wavelength magnetic lows which may indicate the hydrothermal alteration zones following the Salen range. Upward continuation of the residual magnetic anomaly to 4 km shows a circularly shaped magnetic low at the SE of Gedemsa volcano which this might depict a loss in magnetization of hydrothermal altered zones. The residual magnetic anomaly lows (Fig. 6.15) following the Salen range support the presence of thick hydrothermally demagnetized geologic units which is consistent with geologic evidence (Birba and Varlet, 2018).

5.2.6 Analytical signal magnetic anomaly map

Equatorial region magnetic anomalies are complex to interpret as the earth's magnetic field intensity depends on magnetization direction. To overcome this problem, analytical signal (AS) filter which doesn't depend on direction but on strength of magnetization (Lingerew Nebere, 2015 and references there in) is needed. AS Filter removes the effect of magnetization and attitude: makes the identification of source boundaries easy but removing all dip information (Ansari and Alamdar, et al., 2009). The amplitude of AS is expressed as:

$$|\mathrm{A}(\mathrm{x},\mathrm{y})| = \sqrt{(\frac{\partial M}{\partial x})^2 + (\frac{\partial M}{\partial y})^2 + (\frac{\partial M}{\partial z})^2} \qquad (5.12)$$

Where M is observed magnetic field.

The AS magnetic map (Fig. 5.16), obtained from the residual map, shows maxima at the edge of the source body i.e., it shows structural/lithological discontinuity regardless of the direction of magnetization. It is easier to infer source position from AS (Fig. 5.16) map as it enhances short wave length anomalies. It shows high peaks (maxima) over the volcanic complexes (Bora, Tulumoye, Gedemsa, etc.) which could be a reflection of effects of the volcanic rocks.

The AS map (Fig. 5.16) is highly related to the geology of the area and low peaks within the map are attributed to the response of lacustrine sediments. The floor of the Gedemsa volcano is reflected by high values. This can be related with the presence of volcanic vent within the larger caldera. The Salen range is characterized by cumulate of positive and negative peaks in the AS map (Fig. 5.16).

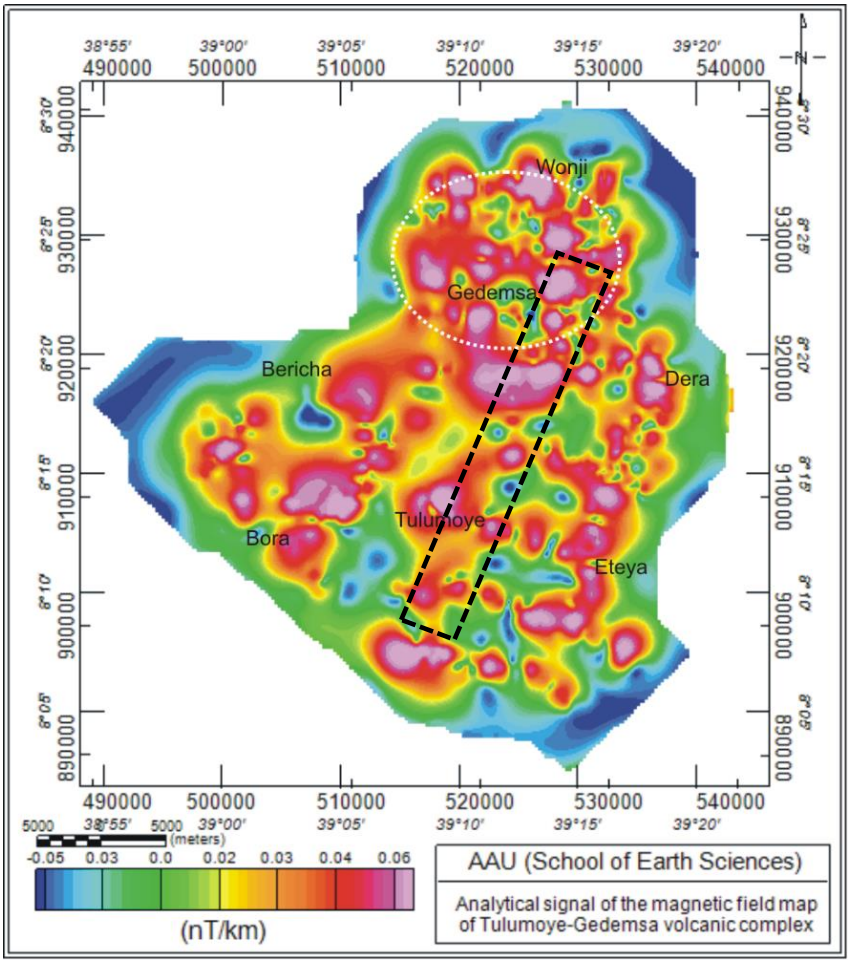

Figure 5.16 Analytical signal magnetic map. The circular shaped polygon enclosed with white broken line is the Gedemsa volcano and its surrounding. The NE-SW aligned rectangular polygon shows the Salen ridge across Tulumoye and the eastern part of Gedemsa volcano.

5.2.7 Tilt derivative magnetic field map

The Analytical signal map (Fig. 5.16) is limited in that it doesn't signify the type of source edge and it only enhance the effect of shallow seated bodies. Aiming at displaying the effect of deep and shallow source bodies and the structural as well as lithological discontinuities at the same time, the Tilt derivative (TDR) map (Fig. 5.17) has been produced. As discussed in the gravity section (section 5.1.6), the positive values in tilt derivative reflect source bodies, values close to zero shows the discontinuity and the negative values are bodies outside of the source body. In the tilt derivative map, structural features are more enhanced and a striking feature which could be the response of NW-SE structures with in the southwest region (in the vicinity of Tulumoye, Bora and Bericha) becomes more clear and visible. Closely examining

Figure 5.17 reveals additional information on the structural and lithological discontinuities in the study area in conjunction with the geological map (Fig. 2.5) and pole reduced residual magnetic anomaly map (Fig. 5.14). The Salen range is characterized by a dominance in negative peaks where reactivation of the volcano-tectonic segment causes demagnetization of rocks by hydrothermal alteration.

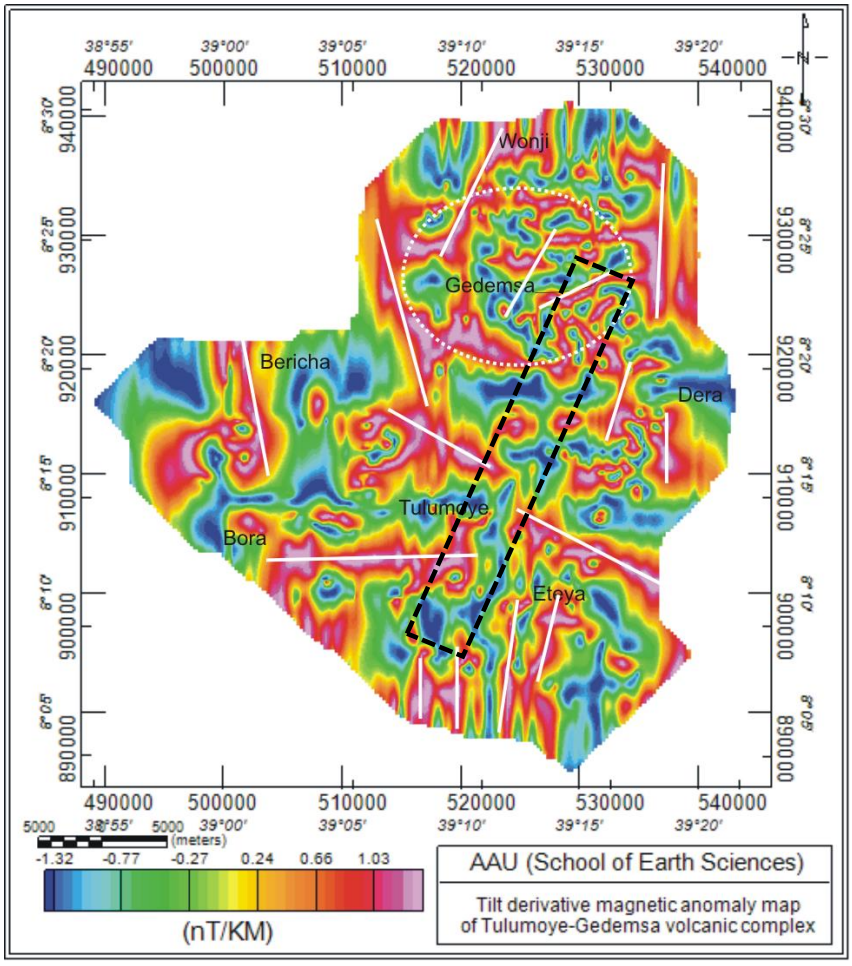

Figure 5.17 tilt derivative magnetic map. The white strike line represents the location of source bodies and the rectangular polygon enclosed with black broken line represents the Salen range.

CHAPTER SIX

GRAVITY MODELLING

6.1 Gravity field of the Central-northern MER

It is determined that relevant information about a study area in a local environment can be extracted by examining the variation in gravity field of a region consisting the study area. To accomplish this task, this research has considered about 37,074 gravity data points provided by the IGB and covering the central-northern MER in which the study area is embedded. This regional gravity data set has been processed to compile the complete Bouguer anomaly (CBA) map (Fig. 6.1) and its enhanced components (Fig. 6.2, 6.3 and 6.4). The aim of examining the compiled CBA and its enhanced components on a regional scale is to investigate the nature and structure of the Gedemsa TMS within the framework of the central to northern MER transition zone. Furthermore, 2D gravity models have been constructed along two profiles (AA and BB) running along and across the rift axis and intersecting at the Gedemsa TMS (Fig. 6.1) for sampling the entire crustal structure.

Figure 6.1 shows the CBA map of the central MER and the transition zone to the northern MER. The floor of the rift is characterized by gravity maxima where a sudden increase in gravity value (> -210 mgal) is evident after the northern termination of the Tulumoye-Gedemsa volcanic complexes. Further south of the Tulumoye-Gedemsa volcanic complexes, the Aluto volcanic complex is characterized by relatively positive gravity anomaly (about -210 mgal). The elevated platforms corresponding to the Guraghe escarpment on the west flank and the Chilalo volcanic range on the eastern flank of the rift are characterized by relatively negative gravity anomalies (< -245 mgal). The western margin is not characterized with a clear boundary fault where the Midre Kebd Structural High (MKSH) is clearly reflected by intermediate gravity response. Since the CBA map (Fig. 6.1) is the response of lithospheric scale materials existing beneath the central-northern MER and the adjacent plateaus, it doesn't provide information on the depth of the individual source bodies. Consequently, wavelength filtering and band pass filtering techniques are applied to the gridded CBA map (Fig. 6.1) in order to obtain the anomaly components that would be employed to get information regarding depths of the individual causative bodies.

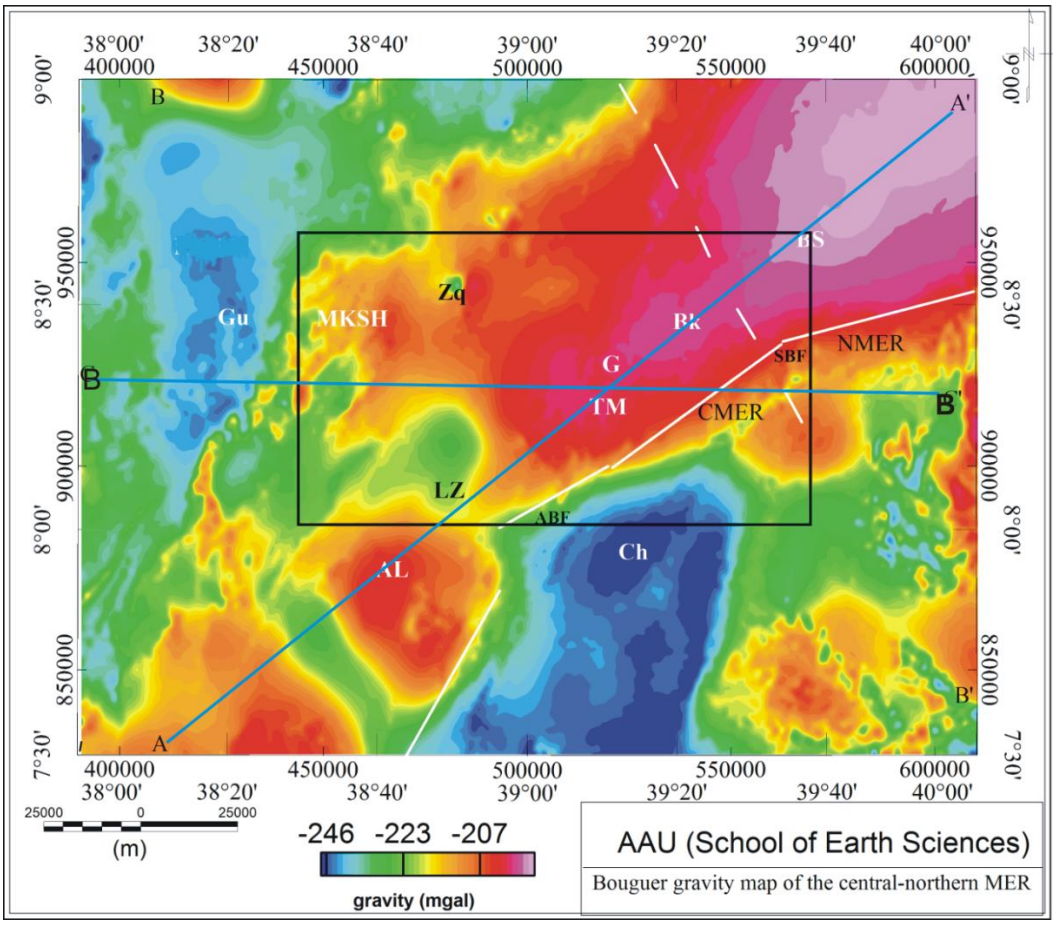

Figure 6.1 Complete Bouguer anomaly map of the central-northern MER. Labels: Al=Aluto, TM=Tulumoye, G=Gedemsa, Bk=Boku, Bs=Boseti, Gu=Guraghe escarpment, MKSH=Midre Kebd Structural High, Ch=Chillalo mountain, ABF=Asela border fault, SBF=Sire border fault, LZ=Lake Ziway. The black rectangle shows the extent of the study area. The white solid line represents border faults. The white broken line shows the expected boundary of the CMER and NMER. The line along AA' and BB' are model profile lines.

The residual gravity anomaly map (Fig. 6.2) of the central to northern MER transition is compiled by applying a high pass filter with 10 km cutoff wavelength to the CBA map (Fig. 6.1). The compiled map (Fig. 6.2) reveals an important insight on architecture of the tectonomagmatic segmentation along the protoridge axis zone in the MER and the off rift volcanic regions on the rift flanks occurring at depths less than 2.5 km. The TMSs of the mapped region (Fig. 6.2) include the A-TMS, G-TMS and B-TMS named after the associated central volcanoes (Aluto, Gedemsa and Boseti). Several authors (e.g. Wolfenden et, al., 2004; Casey et al., 2006) suggest that the Aluto-Gedemsa region belongs to a single TMS named

Aluto-Gedemsa TMS. However, the gravity anomaly signatures compiled in this study (Fig. 6.2 and Fig. 6.4) do not support the suggestion forwarded by the authors as the anomalies of the Aluto and Gedemsa regions are distinct and totally different from each other.

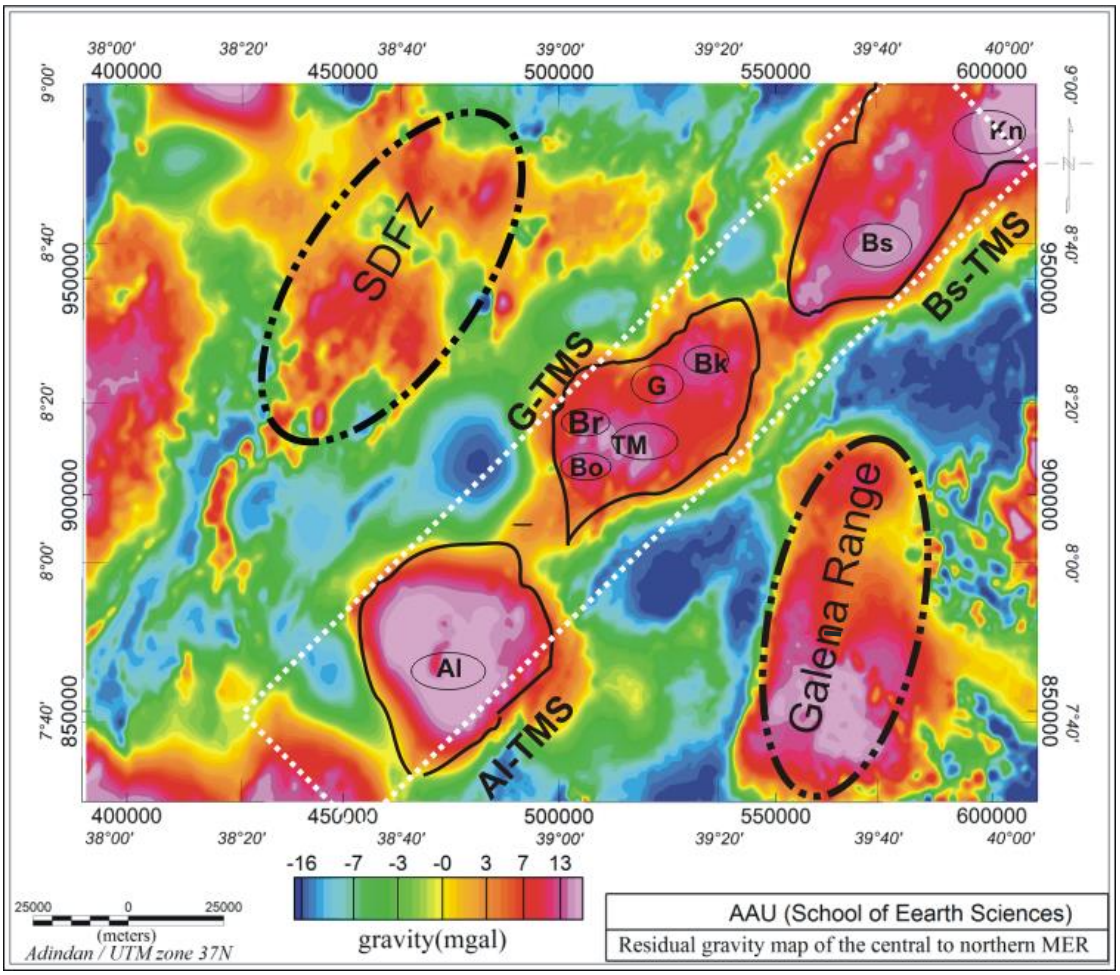

Figure 6. 2 Residual gravity anomaly map of the central-northern MER compiled using a high pass filter with cutoff wavelength 10 km. The NE aligned rectangle with white broken line is zone of the protoridge axis of the MER. The elliptical shaped broken line are the off rift volcanic regions; the elliptical shaped solid line represents the quaternary volcanic centers with in the WFB. Labels: Al=Aluto, Bo=Bora, Br=Bericha, TM=Tulumoye, G=Gedemsa, Bk=Boku, Bs=Boseti, Ko=Kone and Al-TMS, G-TMS, and Bs-TMS represent Aluto, Gedemsa and Boseti Tectono-magmatic segments respectively.

The suggestion by the previous authors that the two TMSs constitute a single TMS is based on evidences coming from surface manifestations and surface data. However, evidences coming from investigation of the subsurface based on gravity data do not support that the two volcanic

complexes are formed by a single magmatic source occurring at a specific depth (Fig. 6.2, 6.3 and 6.4). Investigation results based on surface structural studies (e.g. Corti, 2009) confirms that the two TMSs are different from each other and reinforce the geophysical investigation results of this MSc research work. These TMSs are associated with one or more than one of the quaternary rift volcanoes (Bora, Bericha, Tulumoye, Gedemsa, Boku, Boseti and Kone). For example, the G-TMS is associated with the five rift volcanoes (Bora, Bericha, Tulumoye, Gedemsa and Boku). The off rift volcanoes forming the SDFZ on western rift flank and the Galema range on the southeastern rift flank are clearly identified.

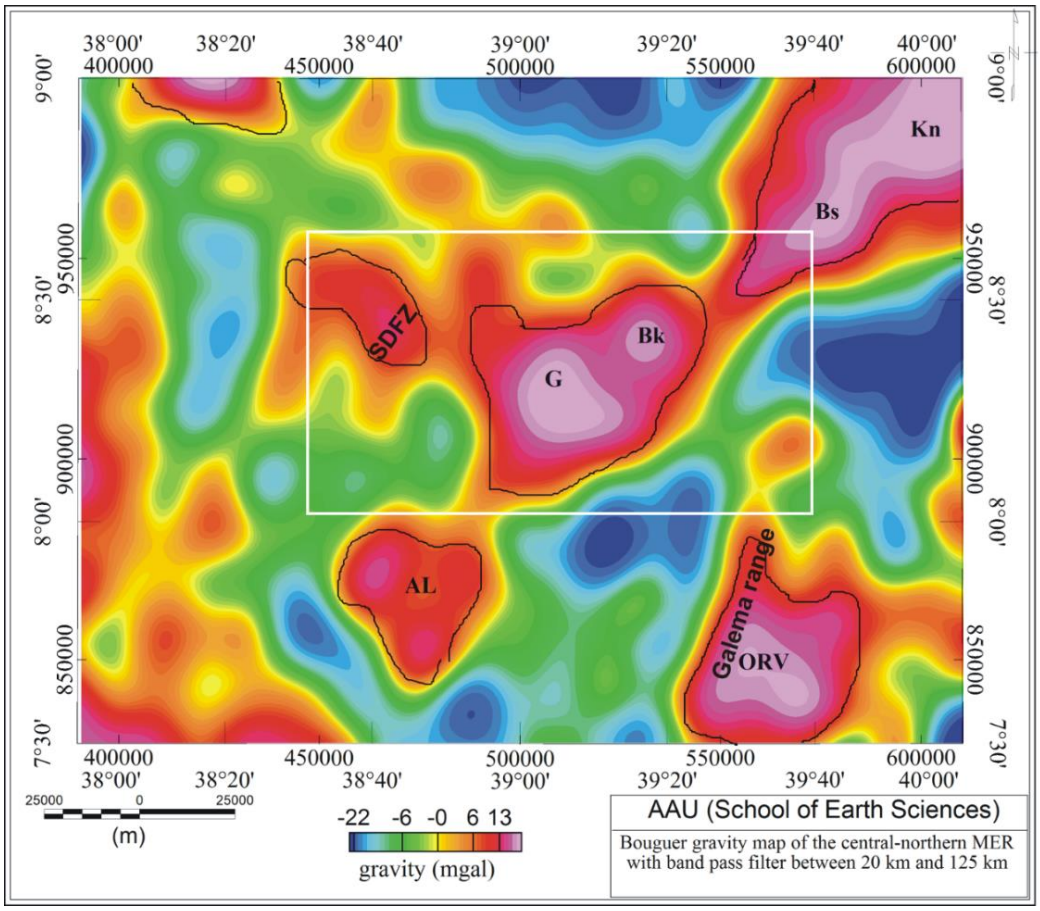

Figure 6.3 Band pass filtered regional gravity anomaly map of the central-northern MER where wavelengths between 20 and 125 km are passed. Labels: Al=Aluto, G=Gedemsa, Bk=Boku, Bs=Boseti, Ko=Kone, ORV=off rift volcano, SDFZ=Silte Debrezeyit Fault zone. The polygon enclosed in black and white lines represent the TMSs and the study area.

The regional anomaly map (Fig. 6.3) of the central-northern MER is compiled by filtering the CBA map (Fig 6.1) with a band pass filter of wavelengths 20 km and 125 km. The compiled

map (Fig. 6.3) enables to extract information on anomaly source bodies occurring within a depth range of 5 to 31.5 km. Figure 6.3 shows a trend of high gravity anomalies caused by the rift floor volcanic complexes (Aluto, Gedemsa, Boku, Boseti and Kone) and off rift volcanic regions (SDFZ and Galema range) occurring at depths less than 2.5 km (Fig. 6.2) (appear) persist to occur at deeper depths between 5 km and 31.5 km. Figure 6.4 is regional anomaly

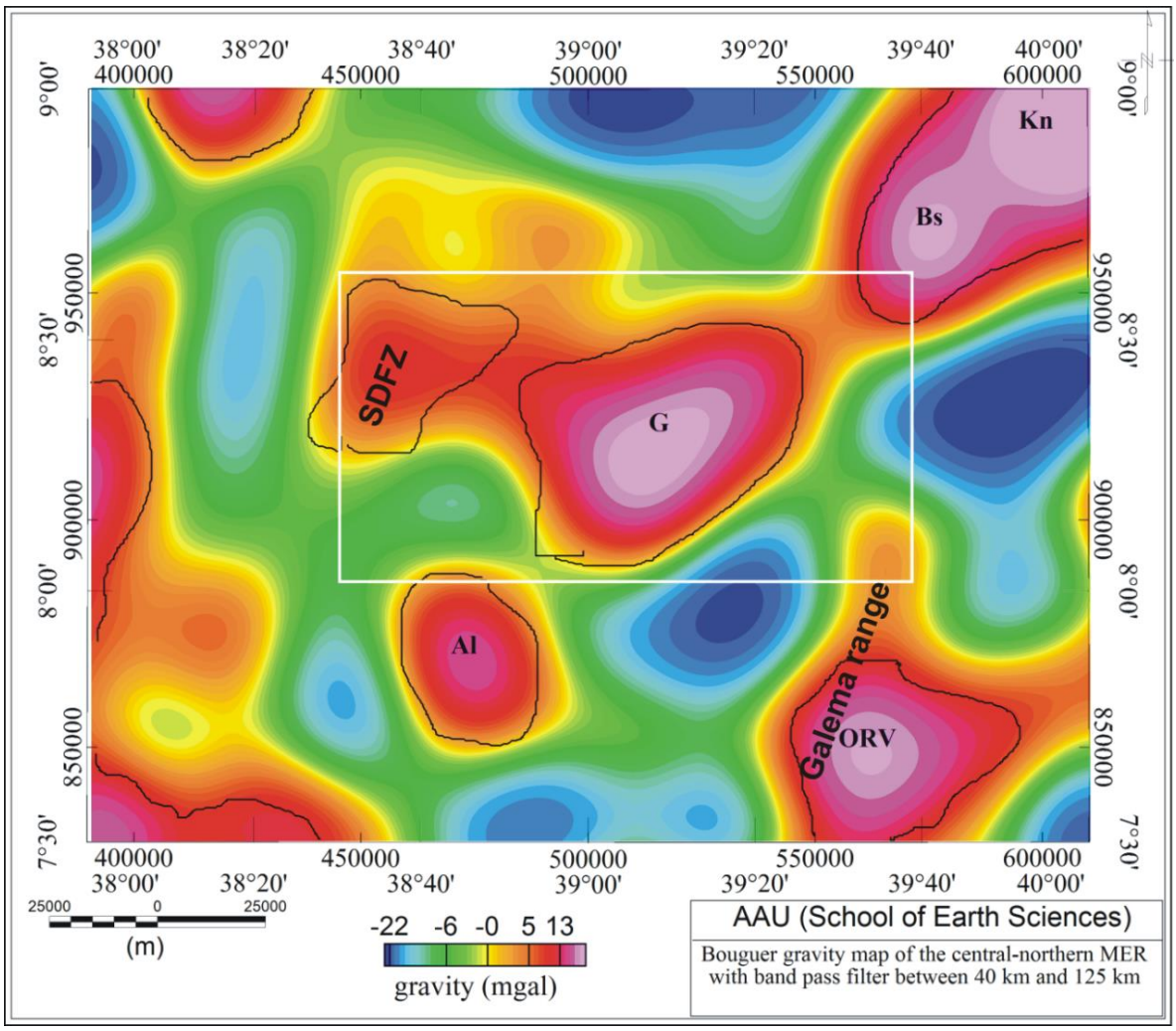

Figure 6. 4 Band pass filtered regional gravity anomaly map of the central-northern MER where wavelengths between 40 and 125 km are passed. Labels: Al=Aluto, G=Gedemsa, Bk=Boku, Bs=Boseti, Ko=Kone, ORV=off rift volcano and SDFZ=Silte Debrezeyit Fault zone. The irregular polygon enclosed in black lines represent the magmatic segments and the rectangle enclosed in white line represents the study area.

map compiled by filtering the CBA map (Fig. 6.1) with a band pass filter of wavelengths 40 km and 125 km. The short wavelength band when compiling this map (Fig. 6.4) is increased to 40 km in order to see the anomaly signature of the subsurface between 10 km and 31.5 km. The map (Fig. 6.4) reveals the appearance of positive circular anomalies occurring over the above mentioned rift volcanoes disappears over the Boku volcano. This implies that the positive circular gravity anomaly over the Boku volcanic complex reflects the high density causative body (probably of magma chamber) occurs at depths less than 10 km.

6.2 2D Gravity models over the Gedemsa TMS within the framework of the MER

Geophysical understanding of the subsurface at a regional scale has an invaluable implication on shallow subsurface studies as the former is a result of key geologic processes originating in a deeper environment. Within this understanding, two 2D gravity models constrained by seismic/geologic data are constructed using Bouguer gravity map (Fig. 6.1). The observed anomaly values are extracted along profile BB (Fig. 6.1) running across the rift axis and along profile AA (Fig. 6.1) running along the rift axis and intentionally selected to intersect at the Gedemsa TMS. The 2D gravity models are constructed for the purpose of sampling the entire crustal structure of the study area.

Although gravity data in isolation are suffered from non-uniqueness, they are a powerful tool when used in conjunction with seismic data; refine the resolution of the seismic data itself or provide additional constraint on lithospheric structure. In the present study, results of seismic data from the EAGLE (Maguire et al, 2006) line 1 and Line 2 along the rift axis (Fig. 2.2) with additional information from previous geological and geophysical studies were incorporated to constrain the gravity data.

6.2.1 Gravity forward modeling

As discussed in section 3.1.6, forward modeling is a process of calculating the geophysical response of an earth model from a hypothetically constructed model. In this work, a 2D modelling software called GYM-SYS, an interactively user interface program, has been used to calculate the gravity responses from a user defined geologic model based on least square best fit.

6.2.1.1 Initial density model

The initial density model has been constructed from the seismic model by converting each seismic layer into density layer using Nafe-Drake density velocity relationship given by:

$$\rho = -168.03 + 1765v_p - 481.72v_p^2 + 60.973v_p^3 - 2.6861v_p^4 \qquad (6.1)$$

Where ρ is the density of subsurface in kg/m^{-3} and v_p is p wave velocity in km s^{-1} (Nafe and Drake, 1957).

From the seismic data basically five density layers have been identified for the initial model:

1. The upper volcanics and sediments which include the Mesozoic sediment, tertiary volcanics, the quaternary sediment and the quaternary volcanics
2. The upper crust
3. The lower crust
4. The upper mantle

In addition to the above main layer's, mafic intrusions under TMS and magma cumulate beneath the lower crust called underplate were also considered (Table 6.1).

Table 6. 1 summary of the model layer velocity (V_p) and density (ρ) property

Layer description	V_p (km/sec) range	Mean V_p (km/sec)	Intial model ρ (g/cm^3)	Final model ρ (g/cm^3)	Thickness (km)
Volcanics and sediment	5-5.2	5.1	2.57	2.57	<6
Upper crust	6.07-6.40	6.25	2.79	2.81	6-21
Lower crust	6.31-6.83	6.57	2.94	2.94	21-38
intrusion	6.65-6.75	6.70	2.93	3.00	-
Under plate	7.38	7.38	3.16	3.16	35-45
Upper Mantle	7.5-8.10	7.75	3.29	3.27	<38

6.2.2 2D gravity model across the MER over the Gedemsa TMS

The aim of selecting profile section (BB' in Fig. 6.1) for this model is to cross the rift floor and its flanks (N-S to SSW-NNE structures). This enables us to verify the distribution of anomalous source bodies within the entire crust including the Gedemsa TMS and its environs within the framework of the central-northern MER. For the constructed 2D model (Fig. 6.5) where five density layers were considered, the error or misfit between the observed and calculated gravity is less than two mGal.

Figure 6.5 shows a lower crust of density 2.94 g/cm^3 overlay the upper mantle beneath the SE plateau and the floor of the rift. Whereas, west wards from the rift axis, a high density (3.16 g/cm^3) material that is different from the upper mantle density (3.27 g/cm^3) is considered. This material is interpreted as an underplate by previous authors (Tiberi et al., 2005; Maguire et al., 2006; Tilahun Mammo, 2013). The upper mantle with density of 3.27 g/cm^3 varies in depth from (41 km) beneath the rift floor to (38 km) beneath the adjacent plateaus.

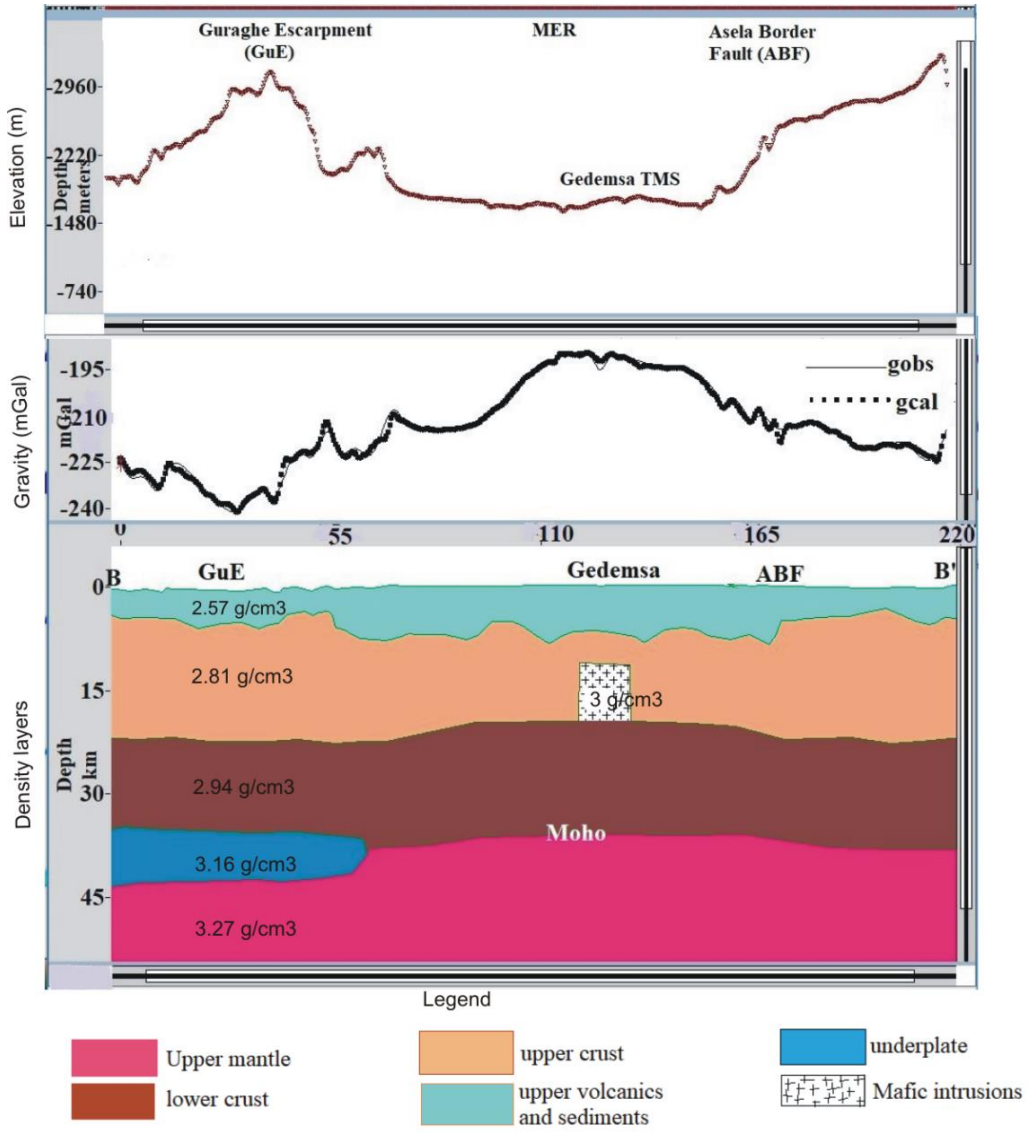

Figure 6. 5 2D gravity model across the MER crossing the Gedemsa TMS. Where, gobs represent the observed gravity and gcalc represent the calculated gravity.

As can be seen from the 2D density model (Fig. 6.5), the depth to moho changes from 41 km beneath the western plateau to 38 km beneath the rift floor which seems to agree with previous

seismic studies (Keranen et al., 2009; Fig. 2.1). The first layer with a density of 2.57 g/cm^3 is attributed to the upper volcanics and sediments which include the Mesozoic sediments overlying the Precambrian basement, the Cenozoic volcanics as well as the quaternary volcanics and sediments. This density layer varies in thickness which may reach up to 6 km beneath the floor of the rift (Fig. 6.5; Table 6.1). Underlying the upper volcanics and sediments, a higher density body (2.81 g/cm^3) has been imaged to a depth of up to 21 km which most probably corresponds to thickness of the upper crust. The thinning of this density layer at the floor of the rift could be due to the effect of the first phase of rifting by mechanical deformation or faulting as it is brittle in nature.

The long wavelength positive anomaly observed across the rift floor is a reflection of a shallow depth to the Moho and occurrence of high density mafic intrusions. The mafic intrusion modeled in Figure 6.5 occurs beneath the Gedemsa TMS and its occurrence extends to an approximate depth range of 10-20 km. This result is comparable with the results of previous works (Keranen et al, 2004; Daly et al., 2008) who imaged most of the mafic intrusions that occur within a depth range of 12-25 km.

6.2.3 2D gravity model along the MER axis crossing the Gedemsa TMS

To characterize nature of the crust beneath the Gedemsa TMS and its environs, an attempt has been made to model the subsurface both across (Fig. 6.5) and along (Fig. 6.6) the rift axis. The two modeled sections intersect each other at the location of the Gedemsa TMS. The density values assigned to the corresponding layers of the two models are the same but the interfaces of the corresponding density layers occur at different depths. Because, the intensity of deformation and uplift of the lithospheric setup along the protoridge axis is higher than that of the cross rift areas. Figure 6.6 displays the elevation profile and gravity profile along with the 2D density model for ease of visualization.

There is no a clear agreement among researchers on the exact boundary of the central and northern segments of the MER. Bonin et al. (2005) reported that the Boru Tora structural high that occurs at the southern termination of the Boseti TMS (Fig. 6.2) is the boundary of the two rift segments. On the other hand, Corti (2009) suggested the Gedemsa region as the place where boundary of the two segments of the rift occurs. Figure 6.6 reveals that gravity increase with decrease in elevation from SW to NE which reflects the difference in stage of evolution for the

central and northern segments of the MER. A closely visualization of the gravity profile and the model (Fig. 6.6) in conjunction with the gravity map (Fig. 6.1) provide reliable information on the separation of the central and northern MER. The Bouguer gravity map (Fig 6.1), the extracted gravity profile and density layers (Fig. 6.6) reflect a sudden change in the anomaly level towards a broad anomaly maximum. This result is in fair agreement with report of Bonin et al. (2005) that the boundary of the central and northern segments of the MER occurs along the Boru Tora structural high immediately south of the Boseti TMS.

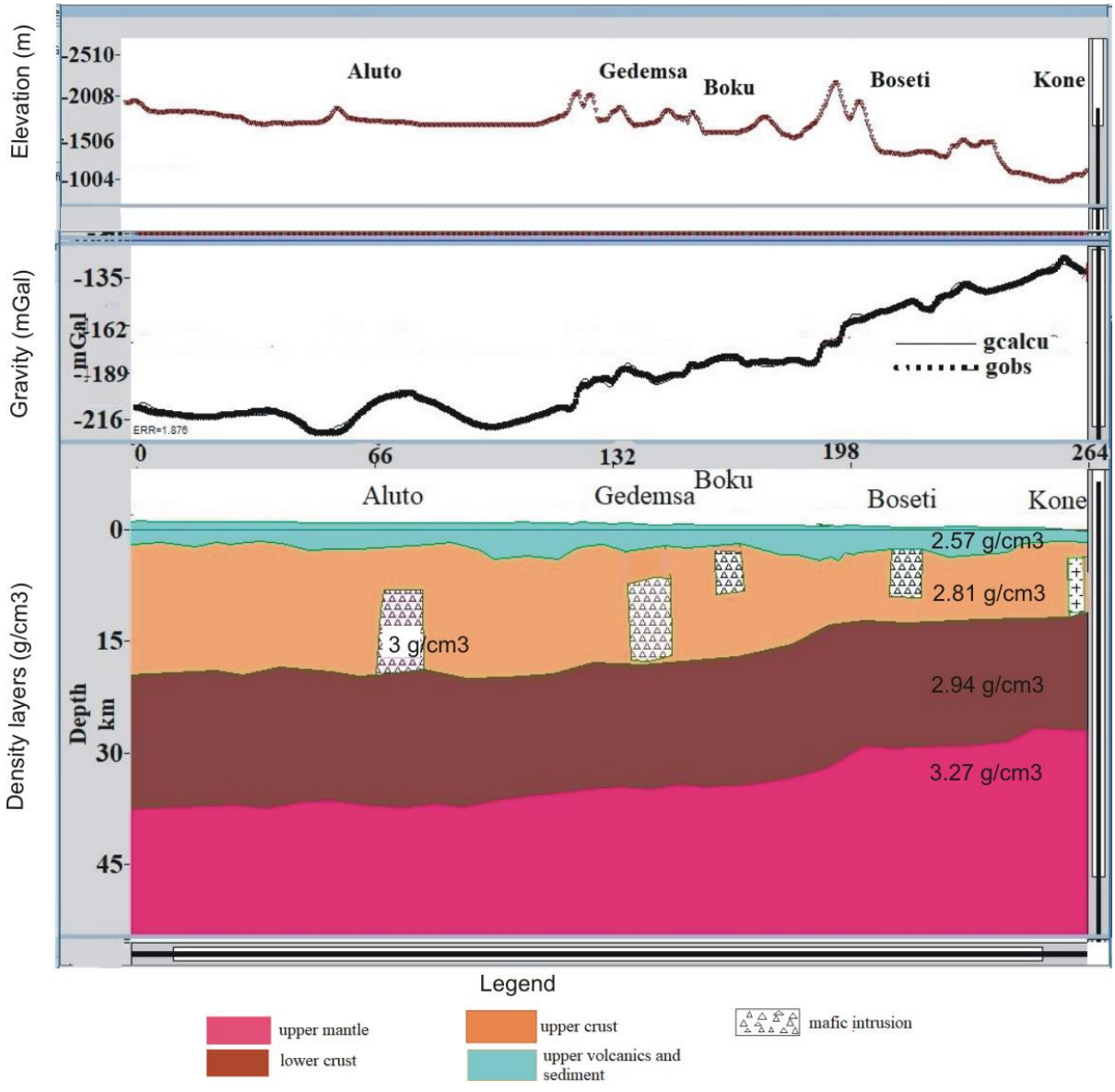

Figure 6. 6 2D gravity model along the axis the MER crossing the Gedemsa TMS..

6.3. Structure of the shallow crust beneath the Gedemsa TMS

Shallow subsurface of an extensional environment is characterized by its brittle nature due to the dominancy of mechanical deformation type where fractures and faults are abundant. Gravity method integrated with magnetic survey is a powerful tool to detect buried structures within such geologic environment. In this regard, two 2D gravity models (Fig. 6.7, 6.8) constructed using residual gravity map (Fig. 5.4) with the observed residual anomaly values extracted along profile P1 and Profile P2. The 2D gravity models are constructed to understand a 3D view (Fig. 6.9) of the shallow crust beneath the Gedemsa TMS.

In this study, an attempt is made to model the density layer of the shallow subsurface constrained by the existing seismic and geologic data. This is aimed to have an implication on detecting the geothermal heat sources in the form of geologic structures (intrusions and shallow magma chambers). There is no clear scaled stratigraphic column for the central sector of the MER to constrain the geophysical data. Consequently, emphasis is given to fill and strengthen this information gap by interrelating the results of this study with the results of the previous efforts in determining stratigraphic columns of the central sector of the MER (Table 2.1; Tsegaye Abebe et al, 2005; Soliva and Schultz, 2008). In addition to this information on depth of the lithologic units, the initial density model for the different lithologic units is summarized in Table 6.2.

Table 6. 2 density of common rocks (Telford et al., 1990)

Rock type	Density range (g/cm3)	Average density (g/cm3)
Sandstone	1.61-2.72	2.2
Shale	1.77-3.20	2.5
Limestone	1.93-2.90	2.42
basalt	2.70-3.30	3
Acidic igneou rocks	2.30-3.11	2.71
Methamorphic rocks	2.40-3.10	2.75
Basic igneous rocks	2.09-3.17	2.63
Mafic intrusions	-	3.00

After having the information in density of common rocks (Table 6.2) and other relevant information from previous studies in the initial model, the following density layers were produced in the final model of the shallow crust beneath the Gedemsa TMS and its environs:

1. The quaternary sediments with an approximate density of 2.38 g/cm^3.
2. Syn and pre-rift volcanic rocks with an average density of 2.6 g/cm^3 which varies in thickness from 2 km at the flank of the rift to 5 km at the rift floor.
3. Variegated shale and clay stone with an average density of 2.49 g/cm^3.
4. Antalo limestone with an average density of 2.42 g/cm^3 and an approximate thickness of up to 200 m.
5. Adigrate sandstone having an average density of 2.17 g/cm^3 having an average thickness of 200.
6. Crystalline basement of density 2.69 g/cm^3.

6.3.1 2D gravity model of the shallow crust across the Gedemsa TMS

Figure 6.7 displays the architecture of the shallow crust constructed using the residual gravity map (Fig 5.4) compiled for the study area constrained by the existing seismic and geologic data. The residual gravity values extracted along profile P1 are used as an input to construct the 2D gravity profile (Fig. 6.7). The profile is selected to run beginning from south west of the Ziquala mount towards the Chilalo mount so that it crosses the Tulumoye volcano which is claimed to be the most promising geothermal prospective site in the study area. The aim of constructing this model is to characterize structure of the shallow crust beneath the magmatic segment interms of geologic structures suitable for geodynamic studies and geothermal resources exploration. Interpretation of the fault patterns from gravity signal response (Fig. 6.7) has been assisted and constrained by geological studies (Corti, 2009; Tsegaye Abebe et al., 2005).

Visualizing the model gives a clear picture of the lateral and vertical discontinuity of geological formations and structures including buried weak zones and faults in addition to mapping the mafic intrusion. The top density layer is the quaternary rift sediment (ρ=2.38 g/cm^3) which covers the surface of most of the rift floor as can be observed from the geological map (Fig. 2.5). The second layer, consists of both pre-rift volcanics (Eocene-Oligocene) and syn rift volcanics (ρ=2.6 g/cm^3) (Miocene–Pliestocene) (Corti, 2009). Although there is no sharp knowledge on their thickness within the central sector of the MER, the presence of Mesozoic sediments is reported by different authors (e.g. Tsegaye Abebe, 2005; Giday Weldegebriel., 1990). Variegated shale and clay stone (ρ=2.49 g/cm^3) overly the Antalo formation (ρ=2.42

g/cm^3) which inturn is underlied by the adigrat formation (ρ=2.17 g/cm^3). The adigrat formation uncomformabily overly the crystalline basement (ρ=2.69 g/cm^3) (Fig. 6.7).

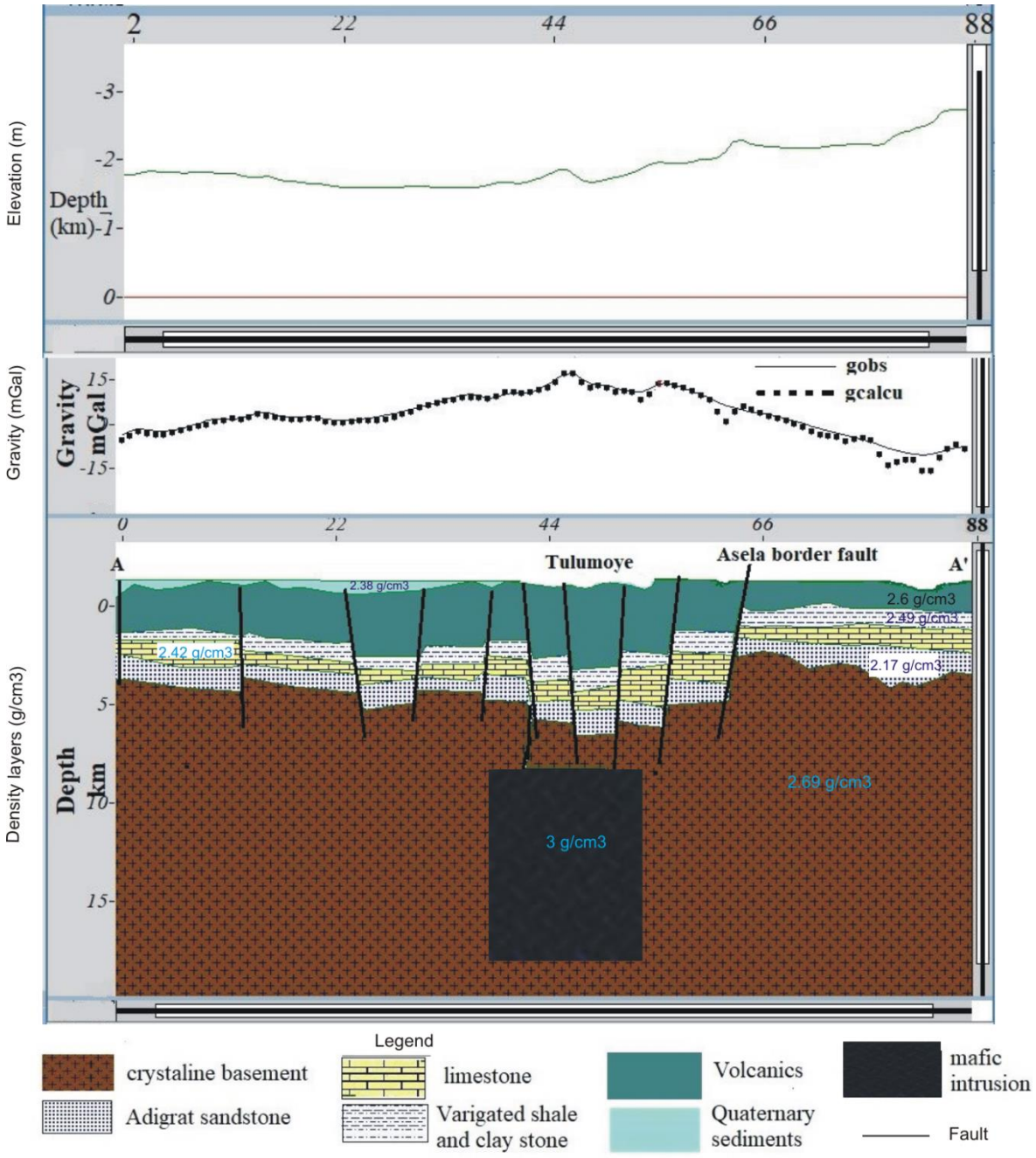

Figure 6.7 2D gravity model across the Gedemsa TMS including the Tulumoye volcano.

Closely examining Figure 6.7 reveals the interaction of intrusion and fault structures which could act as conduits for the transport of a melt system. The anomaly profile consists shorter wavelength anomalies superimposed on the longer wavelength ones. The maximum value

along the gravity anomaly profile (Fig. 6.7) occurs over the Tulumoye volcano which forms part of the Gedemsa TMS. The long wavelength positive residual anomaly observed over the Tulumoye volcano is the response of a mafic intrusion (ρ=3 g/cm3) occurring beneath the Gedemsa TMS which was also detected by previous regional gravity (Mickus et al., 2007; Tiberti et al., 2005; Cornwell et al., 2006) and seismic studies (Keranen et al., 2004; Maguire et al, 2006). The result of 2D gravity modeling compiled in this study (Fig. 6.7) is also in fair agreement with the previous results and infers that depth of the intrusion is as shallow as 10 km with an approximate lateral extent of 25 km wide and 60 km long. The presence of shorter wavelength anomalies superimposed on the longer wavelength anomalies on the gravity anomaly profile (Fig. 6.7) could be attributed to the effect of several shallow depth bodies (e.g. volcanic centers). The sudden change in gravity anomaly observed at places along the gravity profile (Fig. 6.7) could be attributed to the effects of the WFB and the border faults. This effect is highly pronounced on the eastern rift margin where the Asela border fault (ABF) tends to cause a sudden drop in the gravity anomaly signature. The alternation in the short wavelength anomalies (positive to negative) along the gravity profile (Fig. 6.7) could be thought to be attributed to the presence of grabens and horsts in the crystalline basement.

The previous regional gravity studies neglected characterizing the shallow subsurface structures and their interaction with the intrusions especially within the context of geothermal resources occurrence. The present study results (Fig. 6.7) fairly show the interaction of quaternary faults of the WFB with the mafic intrusion which is a good indication for understanding a deeper melt supply to the shallow magma chambers which creates favorable conditions for the occurrence of geothermal resources. Figure 6.7 provides important information regarding the density distribution within the shallow crust beneath the floor of the rift across the Gedemsa TMS with respect to a 2D perspective only. Imaging the subsurface along the TMS (Fig. 6.8) significantly aids to understand the 3D geologic setting (Fig. 6.9) of the area when combined with Figure 6.7

6.3.2 2D Gravity model of the shallow crust along the Gedemsa TMS

Figure 6.8 displays the architecture of the shallow crust along the Gedemsa TMS constructed using the residual gravity map (Fig. 5.4). The residual gravity values extracted along profile P2 (Fig. 5.4) are used as an input to construct the 2D gravity profile (Fig. 6.8). The profile is

selected to run beginning from southeast of the Tulumoye volcano towards the Boku volcanic complex so that it crosses the Boku volcano which is claimed to be the other promising geothermal prospective site in the study area. The density layers are the same with those of the 2D model across the rift axis beneath Tulumoye volcanic center. However, thicknesses of each

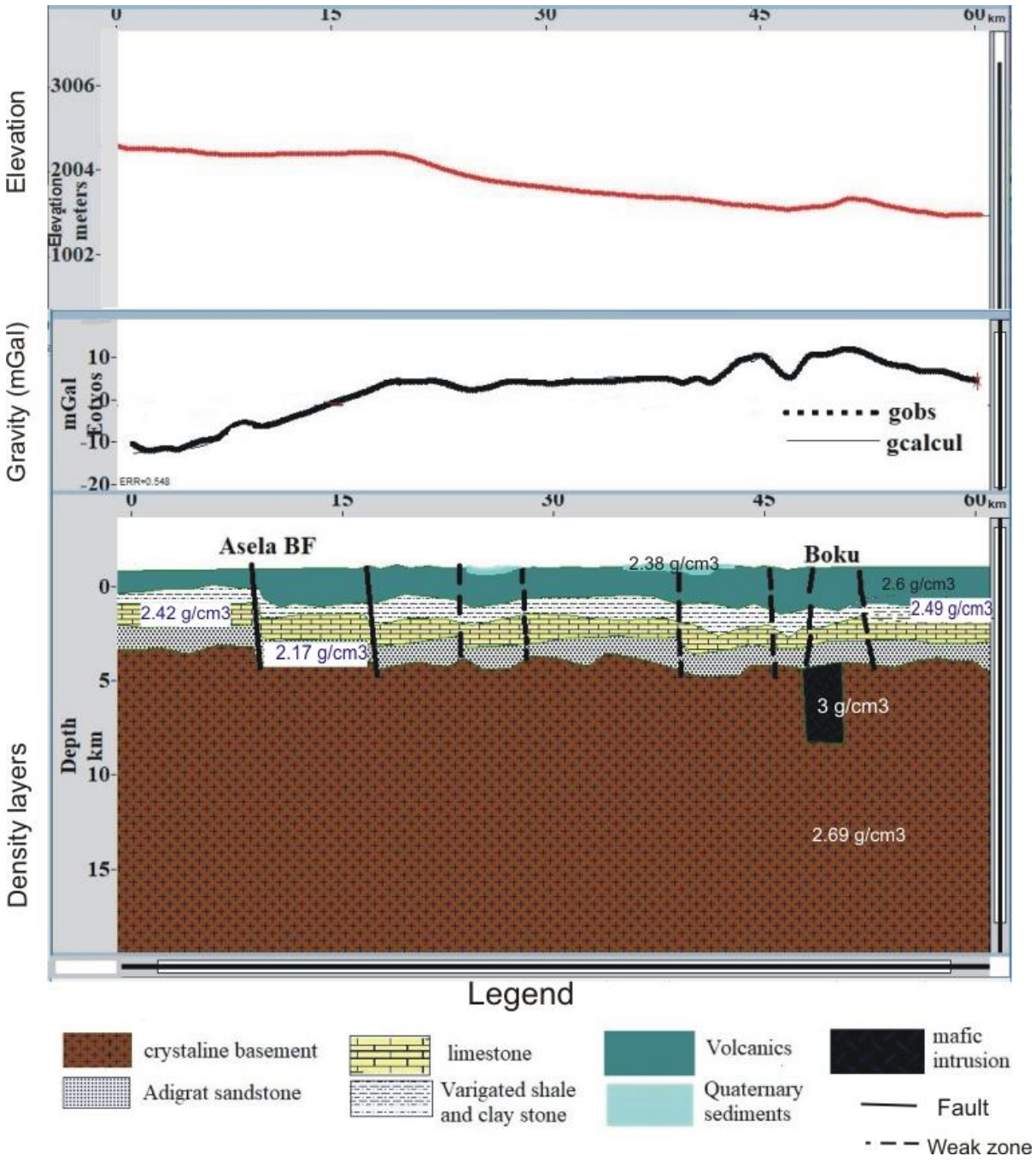

Figure 6. 8 2D gravity model along the Gedemsa TMS including the Boku volcano. The solid black line are faults and the Broken lines are weak zones.

density layer and the structural patterns do not match. Since the direction of the profile is parallel to the quaternary structure of the WFB, most of the fault and fractures are not dissected by the model section. As a result, it is difficult to identify the signal discontinuity reflected by the fault zones. In this regard, the sudden change in anomaly signatures on the gravity profile which may be the response of fault plane, fracture or other discontinuities are generalized to be weak zones in the modeling section marked with black broken lines (Fig. 6.8).

Similar to the 2D gravity model constructed across the Tulumoye volcanic center (Fig. 6.7), six density layers have been identified when sampling the upper crust along the Gedemsa TMS (Fig. 6.8): The upper layer having a density of 2.38 g/cm^3 is attributed to the response of quaternary sediments filling the floor of the rift. These density layers don't occur throughout the model section as their distribution can be seen on the geological map (Fig. 2.5) exposed north east of Tulumoye and east of Dera town. A density of 2.6 g/cm^3 underlying the sediments is needed which is attributed to the pre and post rifting volcanics with an increase in thickness (up to 4 km) of the succession towards the rift axis as volcanic activity is high there. Variegated shale intercalated with clay stone (p=2.5 g/cm^3), limestone (p=2.42 g/cm^3) and sandstone (p=2.2 g/cm^3) have been detected to be the successive underlying density layers, uncomfortably overlying the crystalline basement (p=2.69 g/cm^3).

Figure 6.8 shows a shallow mafic intrusion beneath the Boku volcano with its upper interface as shallow as 5 km. This study could be the first to map the heat source beneath the Boku volcanic complex to be a mafic intrusion existing apart from the Gedemsa TMS. Similar with the deeper mafic intrusion beneath the Gedemsa TMS, Quaternary faults and fractures of the WFB create favorable conditions for the interaction of this mafic intrusion with shallow magma chambers. Imaging the subsurface along the TMS (Fig. 6.8) is thought to significantly contribute to the understanding of the 3D geologic setting of the area (Fig. 6.9) when combined with the results of Figure 6.7.

6.3.3 3D geological setting of the shallow crust beneath the Gedemsa TMS

The 2D gravity models of the upper crust (Fig. 6.7 and 6.8), crossing at the south eastern part of Tulumoye, provide a vital geophysical information in understanding the subsurface geology. Invoking a knowledge of surface geology to these 2D geophysical models results in a clear architecture of the upper crust beneath the Gedemsa TMS in 3D perspective (Fig. 6.9).

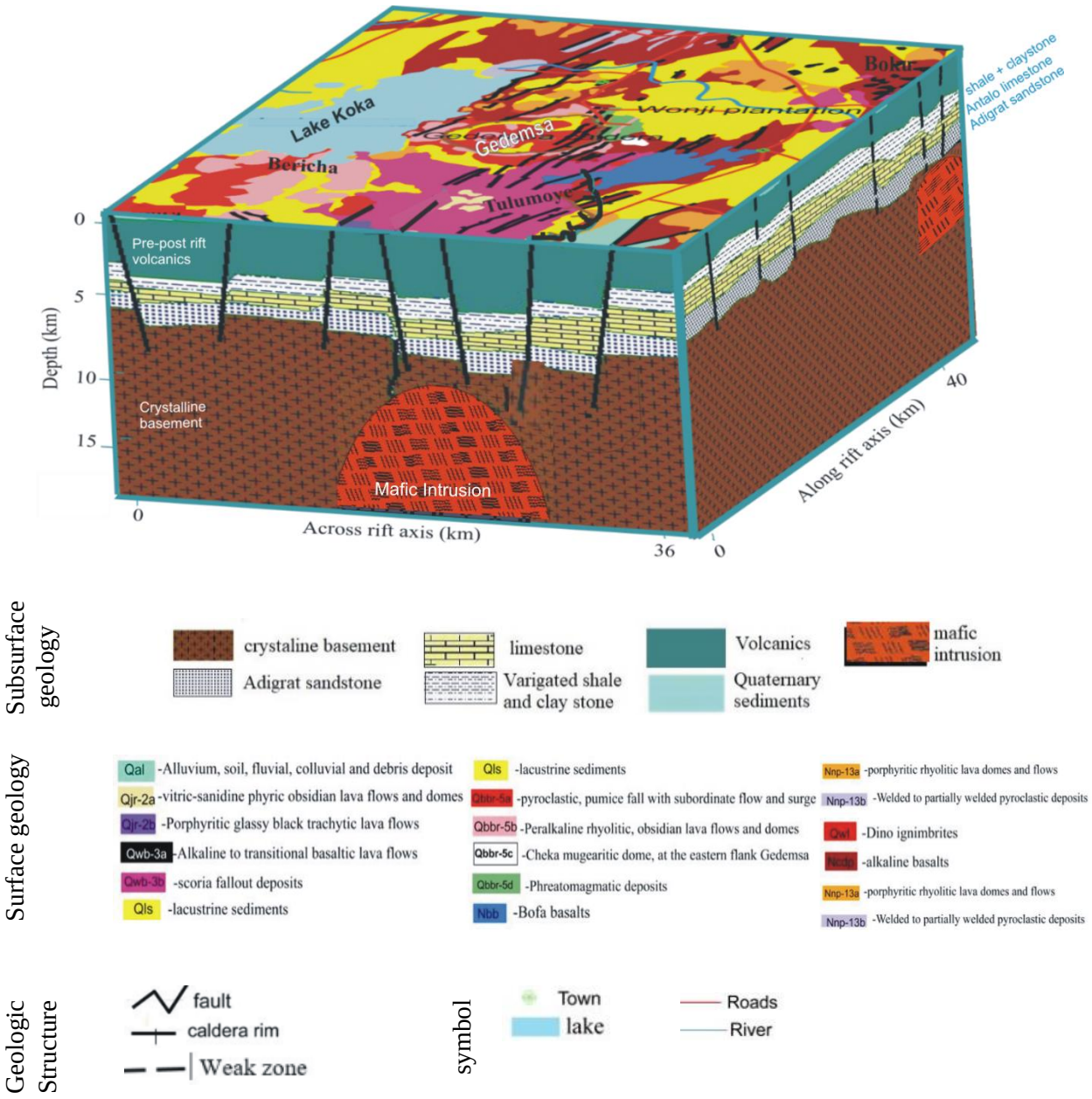

Figure 6. 9 3D architecture of the upper crust beneath the Gedemsa TMS.

It is thought to provide better information on the surface and subsurface geology as well as the associated geological structures within the Gedemsa TMS and its environs. Situated within the rift floor, the area is characterized by an intense deformation where faults and fractures should be more frequent than explained by Figure 6.9. It is clear that the resolution of imaging the subsurface decrease with extent in area of study. But the Geologic model (Fig. 6.9) constructed here is sufficient to characterize the nature and structure of the subsurface at a semi-regional scale with a special emphasis put on the upper crust beneath the Gedemsa TMS and its

environs. It is clear to understand the extent of geologic structure and their interaction to the subsurface geology.

The most notable feature of Figure 6.9 is that it gives a complete view for the magmatic addition to the crust and the corresponding response of the shallow crust, the deformation induced by this diking effect. The addition of mafic material to the lower-upper crust results in opening of fault planes and fractures within the brittle shallow crust. The melt migrates to the shallow subsurface resulting in ponding of a melt to form shallow magma chambers which in turn form different volcanic centers with in the area. A discontinuity or absence of melt supply from deep seated melt reservivour results in different caldera features (Boku. Gedemsa and Tulumoye).

CHAPTER SEVEN

DISCUSSION AND IMPLICATION

Results of this study including gravity and magnetic anomaly maps, profiles and models are translated in to geology of Gedemsa TMS and its Environs. Analyzing these results in conjunction with the existing geological and geophysical data could give a better understanding about the area from structural (section, 7.1), geodynamic (section, 7.2) and geothermal resource occurrence (section, 7.3) view points. Previous gravity (Mickus et al., 2007; Tiberti et al., 2005; Cornwell et al., 2006) and seismic studies (Keranen et al., 2004; Maguire et al., 2006) reported the general crustal structure of the MER and its segmentation along its axis. Investigation results of this study are briefly discussed in this section with the aim of constraining and adding up resolution to the subsurface architecture of the study area with a special emphasis given to the Gedemsa TMS within the framework of the MER.

7.1 The nature, extent and crustal structure of the Gedemsa TMS

The study area is the transition zone from the central to northern MER (Corti, 2009) where initial mechanical phase of rifting shifted to magma assisted rifting as observed from the tectono-magmatic segmentation (Ebinger and Casey, 2001; Casey et al, 2006, Kurtz et al, 2007). In this regard, understanding the subsurface structure of such geologically dynamic environment is invaluable from geodynamic and structural view points. The gravity and magnetic maps, 2D gravity models with profiles and 3D geologic model of this study reveal crustal structure of the study area in different ways with an emphasis given to the upper crust.

7.1.1 The extent and nature of the Gedemsa TMS

The residual (Fig. 5.4 and 6.2), the upward continued (Fig. 5.5), and the band pass filtered (Fig., 6.3 and 6.4) gravity maps reveal the en echelon arrangement of TMSs of the MER in support of seismic (Keranen et al., 2004); gravimetric (Mickus et al., 2007) and geologic (Ebinger and Casey, 2001; Corti, 2009) studies. The residual (Fig. 6.2) and the band pass filtered (Fig. 6.3 and 6.4) gravity anomaly maps of the central-northern MER reveal subsurface reflections of TMSs in the region including the A-TMS, G-TMS and B-TMS. Several authors (e.g. Wolfenden et al., 2004; Casey et al., 2006) consider that the Aluto-Gedemsa region belongs to a single TMS. Contrary to results of these previous works, the present work is the

first in mapping the Al-TMS and G-TMS as distinct TMSs evidenced from their gravity signatures (Fig. 6.2).

The lateral extent of the Gedemsa TMS can be deduced from the residual gravity anomaly maps (Fig. 5.4 and 6.2), the upward continued gravity map (Fig. 5.5) and the band pass filtered gravity maps (Fig. 6.3 and 6.4). From the gravity signature of this maps the lateral extent of the Gedemsa TMS is approximated to be 25 km wide and 60 km long. This value is almost similar with the previous studies (Wolfenden et al., 2004; Casey et al., 2006; Kurtz et al., 2007) who approximated the extent of TMS s with in the MER (20 km wide and 50 km-long).

In the present study, quantitative interpretation through gravity modelling (Fig. 6.5, 6.6 and 6.7) supported by upward continuation (Fig. 5.5) and band pass filtered gravity maps (Fig. 6.3, 6.4. and 6.5) suggested that the Gedemsa TMS occur at approximate depth ranges of 10-20 km. This result is in fair agreement with previous seismic (Keranen et al., 2004; Daly et al., 2008), and electrical (Whaler and Hautot, 2006) studies which map the mafic intrusions at a depth of 12–25 km. However, Mickus et al. (2007) from gravity study reported that the upper interface for the mafic intrusion beneath the Gedemsa TMS as shallow as 7 km and continues to be a depth of up to 15 km. If we accept this suggestion to be true, the signal response of the mafic intrusion should be reflected on the band pass filtered gravity map (Fig. 5.9) and the regional magnetic map (Fig. 13) of this study. However, the effect of this mafic intrusion is not reflected on the above cited maps. Therefore, the interface for mafic intrusion beneath the Gedemsa TMS should be deeper than 7 km as demonstrated on entire crust gravity models (Fig. 6.5 and 6.6) and upper crustal gravity model (Fig. 6.7) of this study. The recent explanation to date on the Gedemsa TMS is the work of Samrock et al. (20018) who image a magma plumbing system sourced from at about 9 km depth using 3D inversion of magnetotellurics data. This result is in fair agreement with results of the present study.

The most challenging dilemma in taking the nature of the Gedemsa TMS in to consideration is that the alignment (shape and orientation) of the TMS with respect to the Protoridge axis of the MER. Surface based studies including structural (Corti, 2009), geological (Ebinger and Casey, 2001; Wolfenden et, al., 2004; Casey et al., 2006) and remote sensing (Kurtz et al., 2007) studies are all in agreement in that the shape and orientation of the TMSs is oblique to the protoridge axis of the MER. Results from structural and shallow source enhancing gravity

data including the HDR gravity map (Fig. 5.6), AS gravity map (Fig. 5.7) and the TDR gravity map (Fig. 5.8) supports the above surface base studies in that the Gedemsa TMS is oriented in an oblique to the protoridge axis of the MER. But, if we consider the subsurface evidence from gravity data, the residual anomaly (Fig. 5.4 and 6.2), the upward continued (Fig. 5.5) and the band pass filtered (Fig. 6.3 and 6.4) gravity maps all support that the Gedemsa TMS is oriented not in an oblique but parallel to the protoridge axis of the MER. Boccaletti et al. (1999) suggested that oblique structures of the MER are a result of the change in the extension direction (NW-SE to E-W or orthogonal to oblique) of Nubia Somalia kinematics. If we accept this hypothesis to be true, the most possible justification for the above difference in surface and subsurface orientation of the Gedemsa TMS can be given as follow: After a magmatic addition to the lower-upper crust along the protoridge axis of the MER, a change in extension direction can result in an oblique structure (WFB) shallower than the mafic intrusion. The other additional finding in this study is that the Boku magmatic segment is a result of magmatic addition to the subsurface which can be as shallow as 5 km (Fig. 6.6).

Researchers are in debate on the nature and formation of TMSs with in the MER. Ebinger and Casey (2001), proposes TMSs as intrusion of magma to the upper crust and horizontal migration of a melt through pre-existing weak zones. However, this geological interpretation may not consider the fact that laterally migrated melt couldn't have a tendency of forming magma ponding that could make collapsed caldera. On the other hand, seismic imaging (Keranen et, al., 2004) of the upper crust within the central-northern MER proposes that TMSs are the result of magmatic addition to the upper crust. In this study, gravity data analysis of three TMSs (A-TMS, G-TMS and B-TMS) within the central MER supports the latter suggestion where an ongoing dyke intrusion to the shallow subsurface can take place through quaternary fractures which assists the ongoing process towards an oceanic environment.

7.1.2 Crustal structure

The 2D gravity models (Fig. 6.5 and 6.6) display crustal structure of the MER along and across the Gedemsa TMS and its environs. The 2D gravity model (Fig. 6.5) across the axis of the MER implies that the crustal thickness in the central MER decreases to the rift axis (up to 38 km) from its adjacent flanks (up to 41 km) which is comparable with previous studies (Dugda et al., 2005; 2007; Maguire et al., 2006; Stuart et al., 2006; Mickus et al., 2007; Keranen et al.,

2009). Examining Figure 6.6 suggested that the deformation intensity increase northward as it can be deciphered from the NE ward decrease in crust-mantle interface. This result is reflected by the CBA maps (Fig. 5.2 and 6.1) and the regional gravity anomaly pattern (Fig. 5.3) with an increase in gravity anomaly maxima to the rift axis and towards the NMER.

Underplating beneath the NW plateau has been detected by seismic (Maguire et al., 2006) and gravimetric (Cornwell et al., 2006) studies. 3D gravity inversion by Tilahun Mammo, (2013) results a more refined solution on underplating with a density of 3.05-3.08 g/cm^3 and 8-13 km approximate thickness. According to Tilahun Mammo, (2013), underplating/magmatic addition is the result of partial melt when afar plume impinged in to the lithosphere and melt migrated through crust mantle interface. The result of the present study (Fig. 6.5) is in agreement in that density of the underplating is about 3.16 g/cm3 with an average thickness of 11 km pinching out westward of the Gedemsa TMS. Most results from previous geophysical studies (e.g. Cornwell et al., 2006; Tilahun Mammo, 2013) documented the location of underplating beneath the NW plateau and pinch out at the western margin of the MER. However, Tiberi et al., 2005 reported the presence of underplating beneath the Aluto-Gedemsa region. In support of the first suggestion, underplating has been mapped in this work after the western margin of the MER towards the western plateau.

Restricting the gravity modeling (Fig. 6.7 and 6.8) to only the Gedemsa TMS and its environs results a high resolution and more informative image of the structure of the shallow crust within the area. Combining the Geophysical evidence in this study with the existing knowledge in surface geology results in a complete 3D view of the upper crustal structure (Fig. 6.9) of the Gedemsa TMS. It is evident that the MER shifts from mechanical rifting to magma enhanced rifting (Ebinger and Casey, 2001; Kurtz et al., 2007). The 2D gravity models (Fig. 6.7 and 6.8) in conjunction with the complete 3D geologic view (Fig. 6.9) reveal a subsurface evidence in support of the hypothesis that the MER is not only in magmatic segmentation but it is on the stage of tectonomagmatic segmentation (Kurtz et al., 2007). The HDR, AS and TDR gravity maps (Fig. 5.6 and 5.7, 5.8) and magnetic (Fig. 5.16 and 5. 17) maps verify the SSW-NNE oriented quaternary Wonji faults and the SW-NE oriented boundary faults. Magnetic low evidences from magnetic maps (Fig. 5.14, 5.15 and 5.17) show a SW-NE structural features following the Salen range in support of Birba and Varlet (2018) who suggested that the Salen

range is the most active volcano-tectonic zone in the area. This volcano-tectonic segment is replaced by Adama-Boku volcanic complex further north (Birba and Varlet, 2018; Fig. 5.5).

7.2 Geodynamic implication

The individual TMS of the MER are poorly known within the context of geodynamic setting (Rooney et al., 2005) although it is a key aspect in understanding the evolution of the MER. Understanding geodynamic setting of an area is difficult as most of the geologic activities are not only hidden from human direct view but are also very slow processes which do not complete within the age of humans. However, analysis of density distribution from gravity data reinforce information from seismic, geologic and geodetic evidences.

The residual gravity map (Fig. 6.2) and a band pass filtered gravity maps (Fig. 6.3 and 6.4) clearly display the en echelon arrangement of TMSs (Aluto, Gedemsa, Boseti) and off rift volcanic ranges (Galema range and SDFZ). This evidence shows the process of a magmatic addition to the crust not only on the rift axis but also on its flanks as an off rift volcano. Although the axial part of the MER is accepted to be the locus of strain in existing rift models, there is an increasing evidence in the off rift extension from petrologic studies (Chiasera et al., 2018; Rooney et al., 2007) and gravity data analysis in this study (Fig. 6.2, 6.3 and 6.4). The occurrence of bilateral of off rift volcanic ranges (e.g. Ziquala and Galema) implies a broad distribution of strain and complex geodynamic setting of the MER.

Aluto-Gedemsa region is attributed to be the most dynamic locale along the MER (Abebe et al., 2007; Bastow et al., 2010; Kendall et al., 2006). This is supported by extreme gravity maxima over Aluto revealed in Figure 6.2. The Gedemsa TMS within the MER is attributed to be one of the most geodynamically active areas where the two “en echelon” spreading and diking segments of Tulumoye (Salen Range) and Boku-Adama coexist (Birba and Varlet, 2018). Demagnetization trend (Fig. 5.14 and 5.17) following the Salen range supports the reactivation of the Salen range within this active TMS zone. One of the important concept which makes the geodynamic setting of the area ambiguous is the dilemma discussed in section 7.1.1. According to the surface structural studies, the TMSs within the WFB resulted from oblique extension to the protoridge axis. However, the subsurface evidence from gravity data in this study supports the magmatic addition in the same orientation of the rift axis. This argument needs further geochemical and geophysical evidence to refine the ambiguity.

Most of the rift TMSs reflects SW-NE positive gravity highs (Mehatsente et al., 1999; Tiberi et al., 2005) and high seismic velocities (Keranen et., 2004) within the WFB. However, Gedemsa TMS show unique anomaly feature with a perturbation/shift of high velocity beneath the SDFZ (Fig. 2.1a) but not on gravity anomaly maps (Fig. 5.4, 6.2, 6.3 and 6.4). In fact, SDFZ shows positive gravity anomaly but is not as high as that occurs over the Gedemsa TMS (Fig. 6.2, 6.3 and 6.4). Despite seismic evidences show shift in velocity highs towards SDFZ in the vicinity of Gedemsa, subsurface evidence from gravity signal response shows gravity highs consistent with surface location of the TMS (Fig. 5.5, 6.3 and 6.4). The diversion of gravity anomaly of the Gedemsa TMS to the NW from the normal NE-SW to the SDFZ zone could be attributed to be a pre-existing weak zones for the later coming melt flow. However, this dilemma needs further geochemical and geophysical evidences and it is better to left out it as an open problem.

The direct link between tectonics and magmatism has been suggested from the association of basaltic cinder cones and flows to tail cracks of faults/fractures within the WFB and SDFZ (Tesfaye korme et al., 1997; Tesfaye korme et al., 2004). The maximum depth of faults and fractures within the WFB is remain a controversial. Structural evidences suggested an estimated maximum depth of 2 km (Acocella et al., 2003) and seismic results further suggests up to 14 km (kier et al., 2006) depth. In support of the second hypothesis, the gravity models (Fig. 6.7 and 6.8) reveal the occurrence of faults and fractures greater than 11 km depth. All this results accepts the presence of brittle as well as dynamic crust within this depth ranges.

The formation of faults and fractures as well as the transport of a melt with in the shallow crust of the area is continued to be an answered question. Some authors proposed that a segment centered magmatic system feed dykes emplaced laterally along the rift axis within the pre-existing openings (Kurtz et al., 2007; Ebinger et al., 2001). A more advanced explanation on geodynamic activity beneath the TMSs is an ongoing dyke intrusion (Casey et al., 2006; Keranen et al., 2004; Keranen et al., 2009). The occurrence of the majority of seismic activity (Keranen et al., 2004; Keranen et al., 2009) during dyke intrusion supports an intrusion induced normal fault up on reaching the tensile limit of the lithosphere within the vicinity of the TMS (Acocella et al., 2003). In strengthening the second argument, the result of this study is in agreement that the geodynamic activity of the upper crust beneath the Gedemsa TMS and its environs is governed by an intrusion induced faulting and fracturing followed by swarm of

dykes. Concentrated stress at the leading tip of the intrusion induce surface fracturing and faulting within WFB which propagate upward from the upper crustal zone of intrusion (Casey et al., 2006; Keranen et al., 2004; Keranen et al., 2009; Fig. 6.5, 6.6, 6.8 and 6.9). Faulting/fracturing followed by magmatic addition to the upper crust of the region induce a frequent earthquake to the region. These interdependent geologic processes control the geodynamic activity of the transition zone of the central to northern MER.

7.3 Geothermal resource implication

The high temperature geothermal resource of Ethiopia is located within and associated with the MER development related with shallow magma chambers following the axis of the rift (Greenfield et al., 2019; Samrock et al., 2018). These resources are mainly controlled by the quaternary structures within the rift floor (Selamawit Worku and Engdawork Admasu, 2015) which is an ambiguous in constraining the occurrence of this resource. These ambiguities generate substantial uncertainties in hydrothermal resources explorations.

The Tulumoye-Gedemsa region and its environs consist of prospective geothermal sites including Tulumoye, Gedemsa, Geregendi, Boku and soderie (Fig. 6.6). Gravity anomaly alone is not an indicative of geothermal resource occurrence. However, results of gravity data in conjunction with magnetic data provides a vital information on key elements of the resource (e.g. heat source) in the form of geological structures. These combined potential methods in the present study provided an insight on the deep heat sources which supply heat for shallow magma chambers/intrusions. In this study, interpretations of maps, profiles and models assisted by geologic information's reveals a good constraint not only on the deep heat sources but also the role of geological structures in melt transport to the shallow magma chambers.

Gravity maxima on the CBA (Fig. 5.2) and upward continued (Fig. 5.3) maps in conjunction with existing geological (Ebinger et al., 2001; Bekele Abebe et al., 2007) and geophysical (Samrock et al., 2018; Greenfield et al., 20019; Bastow et al., 2010) studies indicate the presence of deep sourced melt supply beneath the Aluto-Gedemsa region. An ongoing dyke intrusion (Keranen et al., 2004; Casey et 2006; Keranen et., 2009) in this environment create a favorable condition for the occurrence of potential geothermal system. Deep seated body beneath the Gedemsa and Tulumoye is inferred from the upward continued map (Figure 5.5) as the anomaly signal response increase with upward continuation height. These anomaly

signatures might be the reflections of intrusions at depth which supply melt to the shallow magma chambers of the volcanic fields. On the other hand, the anomaly source beneath the Boku volcano could be of shallow origin as its effect is observed to disappears on the upward continuation and band pass filtered gravity maps (Fig. 5.3 and 6.4). This is also in a good agreement with the result of Tamiru Alemayahu and Tigistu Haile, (2008) who suggest that the heat source of the Boku geothermal area is a shallow seated magma chamber. Tigistu Haile and Tamiru Alemayahu, (2012) reported the occurrence and interference of deep thermal system between Soderie and Geregendi thermal springs (Fig. 5.6). This can be possible through very near surface hydrothermal transportation system but there is no evidence coming from the gravity data for the occurrence of buried weak zones accommodating melt/hydrothermal conduit between the two thermal fields.

The short wavelength circular shaped anomalies (Fig. 5.4) occurring over the Boku, Gedemsa and Tulumoye volcanoes (Fig. 5.4) could be attributed to be effects of shallow intrusion and magma chambers. The horizontal derivative map (Fig. 5.6) reveals that the quaternary fractures and faults of the WFB might have played a great role to act as hydrothermal fluid pathways from the heat sources of shallow magma chambers to the geothermal sites. Pliminary studies proposed the Gedemsa caldera as the heat source for the Gergedi thermal spring. This could be possible as the HDR map (Fig. 5.6) shows a series of striking linear feature running from the Gedemsa volcano to the Gergedi thermal spring which may act as a conduit for the thermal manifestation. The AS gravity map (Fig. 5.7) shows gravity maxima over the thermal fields of Gedemsa, Tulumoye and Boku geothermal prospect with in the central sector of the MER. It is possible to suggest that this anomaly features could possibly the effects of shallow magma chambers occurring beneath these geothermal prospect areas which act as hot spots or heat sources. This is supported by the ED map (Fig. 5.10) which shows the occurrence of 3D bodies (e.g. hot spots and craters) buried beneath the Gedemsa, Tulumoye and Boku caldera.

The magnetic data also reveal the presence of persistent magmatic heat sources along the Salen range in support of geological views (Birba and Varlet, 2018). The residual magnetic anomaly map (Fig. 5.14) reflects a SW-NE aligned anomaly minima following the Salen range. These magnetic lows following this active volcano-tectonic range indicate the existence of thick hydrothermal demagnetization zone. It is known that, hydrothermally demagnetized rocks have a negative magnetic susceptibility contrast. Intersection zones of SSW-NNE and NW-SE

structures evidenced from magnetic (F.g. 5.17) and gravity (F.g. 5.8) TDR maps and surface structural data at the Tulumoye volcanic complex are attributed to create a favorable condition for the occurrence of hydrothermal fluid zones.

A casual glance of the gravity models (Fig. 6.7 and 6.8) in conjunction with the gravity (Fig. 5.4, 5.7, 5.8, and 5.9) and magnetic (Fig. 5.14, 5.15 and 5.17) anomaly maps provide important background to understand the heat sources. A more detail look at the 2D density model (Fig. 6.7) illustrates that addition of mafic materials to the upper crust provides melt for the shallow magma chambers through the quaternary faults acting as conduits. The presence of shallow magma chambers is reflected by the circularly shaped gravity and magnetic anomaly peaks. The melt which is highly buoyant and less dense than the host rock (crystalline basement in this case) enforced by the geopressure rises through the faults and fractures to the shallow subsurface to form shallow magma chambers. Absence of a melt supply from the deeper intrusion to the shallow magma chambers may result in collapse of the magma pond forming a caldera feature (Gedemsa, Tulumoye, Boku). This process tends to create a favorable condition that favors the occurrences of geothermal resources in the central sector of the MER, specifically beneath the Gedemsa TMS.

Finally, closely examining the 3D geologic model (Fig. 6.9) and the topographic map (Fig. 4.1) could be thought to act as a mindset conceptual model for understanding the geothermal system of the region. Addition of magma to the upper crust could induce faults and fractures which intern results in a swarm of dykes and shallow magma chambers. The downward percolation of surface water from nearby highlands (Chilalo, Ziquala) including the existing ground water interact with the buried heat sources (shallow magma chambers) to form hydrothermal fluids. The younger shallow faults and cracks might have acted as pathways for the hydrothermal fluids detected at the surface as thermal spring, fumaroles or as altered grounds observed over the Tulumoye geothermal prospect area (Birba and Varlet, 2018). It should also be noted that faults and fractures of the WFB in the area could have played a triple fold role: 1) Transporting a melt from the deep intrusion to shallow magma chambers. 2) Acting as pathways for migration of the surface and groundwater to the shallow magma chambers and intrusions. 3) Transporting the thermal fluids to the surface to be detected as thermal manifestations.

CHAPTER EIGHT

CONCLUSION AND RECOMMENDATION

8.1 Conclusion

Interpretation of combined potential field (gravity and magnetic) data in conjunction with pervious geological and geophysical data in this study have provided important contributions regarding the geodynamic setting, crustal structure and geothermal resources of the study area. The following conclusions have been forwarded based on interpretations made and results obtained from geologically constrained geophysical studies conducted over the Gedemsa TMS and its environs:

The 2D gravity models of the entire crust across and along the Gedemsa TMS reveal three density layers (upper volcanics/sediments, upper crust with mafic intrusion and lower crust) overlying the upper mantle with underplating beneath the NW plateau. The along axis gravity model combined with high pass and band pass filtered gravity maps show the tectono-magmatic segmentation (A-TMS, G-TMS and B-TMS) of the MER along its axis. In this study, the Aluto and Gedemsa regions are identified to belong to two distinct TMSs as evidenced by the gravity data. The bilateral occurrence of off rift volcanic zones (e.g. Ziquala and Galema) evidenced from previous petrological data reinforced by the gravity data in this study show the distribution of deformation beneath the MER including its flanks and the complex geodynamic setting of the MER.

The 2D gravity models of the Upper crust show the occurrence of intrusions (ρ=3 g/cm^3) extending to an approximate depth range of 10-20 km and 5-10 km beneath the Tulumoye-Gedemsa and Boku Volcanic complex respectively. This magmatic addition to the upper crust is attributed to an ongoing dyke intrusion where concentrated stresses at the leading tip of the intrusion induce surface fracturing/faulting. Gravity data analysis of the present study suggests that at deeper depths the Gedemsa TMS is oriented and elongated parallel to the protoridge axis of the MER and changed its orientation oblique to the rift axis at the near surface. The lateral extent of the Gedemsa TMS is approximated to be 25 km wide and 60 km long.

The shallow crust 2D gravity models and 3D geologic interpretation combined with the gravity and magnetic anomaly maps reveal the occurrence of potential geothermal heat sources (at

Tulumoye and Boku): A melt supply of deeper mafic intrusion acting as a magmatic source is interconnected with shallow magma chambers through quaternary faults. Magnetic lows following the Salen range and circularly positive gravity maxima over the Tulumoye and Boku volcanoes combined with surface thermal manifestations are indicators for the presence of hydrothermal resources. Intersection zones of SSW-NNE and NW-SE structures revealed by magnetic and gravity TDR maps and surface structural data at the Tulumoye volcanic complex are attributed to create a favorable condition for the occurrence of hydrothermal fluid zones.

Quaternary faults of the WFB play a three fold role in the geothermal system of the Gedemsa TMS: 1) Transporting melt from the deep intrusion to shallow magma chambers. 2) Acting as pathways for migration of surface or groundwater to the shallow magma chambers and intrusions. 3) Transporting thermal fluid to the surface so as to be detected as thermal manifestations.

8.2 Recommendation

- Previous seismic studies show a perturbation of high seismic velocity from the axial part of the rift (Gedemsa) to the rift margin (SDFZ). However, the gravity anomaly map shows gravity maxima at the axial part (Gedemsa), without perturbation. Therefore, semi-regional magnetotellurics data is recommended to refine this dilemma.
- Surface based studies indicate that the surface segmentation of the WFB into TMSs is persistent to the subsurface with oblique to the MER axis. However, results from gravity data of this study show subsurface image of the Gedemsa TMS oriented parallel to the MER axis. High resolution seismic data is needed to refine the gravity data result.
- The limitation in areal coverage of the magnetic data, complex topography to conduct ground magnetics, preclude interpretation of the two potential field data in conjunction for the whole area. Airborne magnetic survey is vital to construct Curie point temperature map (ultimate use of magnetic survey in geothermal resource exploration).
- Finally, as there is no superior method, interpretation of the above recommended geophysical methods should be made being integrated with the existing geophysical, geological and geochemical data to come up with an optimal constraint on subsurface information for the whole area.

REFERENCES

Acocella, V., Tesfaye Korme and Salvini, F. (2003). Formation of normal faults along the axial zone of the Ethiopian rift, *J. Structural. Geol*., **25**: 503–513.

Agostini, A., Bonini, M., Corti, G., Sani, F. and Manetti, P. (2011). Distribution of quaternary deformation in the central Main Ethiopian Rift, East Africa, retrieved from https://dx.doi. Org/101029/2010TC002833 on 03.01.2020.

Ansari, A. and Alamdar, k. (2009). Reduction to the Pole of magnetic anomalies using Analytic Signal. *World Applied Sciences Journal* ***7***: 405-409.

Baker, J.A., Thirlwall, M.F. and Menzies, M.A. (1996). Sr-Nd-Pb isotopic and trace element evidence for crustal contamination of plume-derived flood basalts: Oligocene flood volcanism in western Yemen, *Geochimica et Cosmochimica* Acta, **60**:2559–2581.

Bastow, I.D., Stuart, G.W., Kendall, J.M. and Ebinger, C.J. (2005). Upper mantle seismic structure in a region of incipient continental breakup: Northern Main Ethiopian rift, *Int. Journal of Geophysics*, **162**: 479–493.

Bastow, I.D., Nyblade, A.A., Stuart, G.W., Rooney, T.O. and Benoit, M.H. (2008). Upper mantle seismic structure beneath the Ethiopian hot spot: Rifting at the edge of the African low-velocity anomaly, retrieved from http://dx.doi:10.1029/2008GC002107 on 20.09. 2019.

Bastow, I. D., Pilidou, S., Kendall J.M., and Stuart, G. W. (2010). Melt induced seismic anisotropy and magma assisted rifting in Ethiopia: Evidence from surface waves, *Geochem. Geophy., Geosys*. **11**: 05-11.

Bastow, I., and Keir, D. (2011). The protracted development of the continent-ocean transition in Afar. *Nat. Geosci*. **4**: 248–250.

Beard, L. (2000). Detecting and identification of north south trending magnetic structures near the magnetic equators. *Geophysical prospecting*, **48**: 745-761.

Bekele Abebe, Acocella, V., Tesfaye Korme and Dereje Ayalew (2007). Quaternary faulting and volcanism in the Main Ethiopian Rift, *J. Afr. Earth Sci*. **48**: 115–124.

Bilham, R., Bendick, R., Larson, K., Mohr, P., Braun, S., Tesfaye Korme, and Lakemaryam Asfaw (1999). Secular and tidal strain across the Main Ethiopian Rift, *Geophys. Res. Lett*. **26**:2789–2792.

Birba, E. and Varet, J. (2018). Tulumoye geothermal project (Oromia, Ethiopia). **In:** *proceedings of the 7th African rift geothermal conf.* pp. 231-235, Kigali, Rwanda 13 pp.

Blakely, R.J. and Simpson, R.W. (1986). Approximating edges of source bodies from magnetic or gravity anomalies. *Geophysics*, **51**:1494–1498.

Blakely, R.J. (1995). *Potential Pheory in Gravity and Magnetic Applications.* Cambridge University Press, Cambridge, 321pp.

Boccaletti, M., Getaneh, Assefa. and Tortorici, L. (1992). The Main Ethiopian Rift: an example of oblique rifting, *Annales Tectonicae*, **6**:20–25.

Boccaletti, M., Bonini, M., Mazzuoli, R., Bekele Abebe, Piccardi, L. and Tortorici, L. (1998). Continental rift architecture and patterns of oblique extensional tectonics in the Ethiopian Rift (Horn of Africa), *Tectonophysics,* **287**: 97–116.

Boccaletti, M., Mazzuoli, R., Bonini, M., Trua, T. and Bekele Abebe (1999). Plio-Quaternary volcano-tectonic activity in the northern sector of the Main Ethiopian Rift (MER): relationships with oblique rifting, *J. Afr. Earth Sci*. **29**:679–698.

Bonini, M., Souriot, T., Boccaletti, M. and Brun, J.P. (1997). Successive orthogonal and oblique episodes in a rift zone: laboratory experiments with application to the Ethiopian Rift, *Tectonics,* **16**: 347–362.

Bonini, M., Corti, G., Innocenti, F., Manetti, P., Mazzarini, F., Tsegaye Abebe and Pecskay Z. (2005). Evolution of the Main Ethiopian Rift in the frame of Afar and Kenya rifts propagation, retrieved from http://dx.doi:10.1029/2004TC001680 on 20.11.2019.

Casey, M., Ebinger, C.J., Keir, D., Gloaguen, R. and Mohamad, F. (2006). Strain accommodation in transitional rifts: extension by magma intrusion and faulting in Ethiopian magmatic segments, *Geol. Soci.* **259**:143–163.

Chiasera, B., Rooney, T.O., Girard, G., Gezahegn Yirgu, Grosfils, E., Dereje Ayalew, Mohr, P., Zimbelman, J., and Ramsey, M.S. (2018). Magmatically assisted off-rift extension: The case for broadly distributed strain accommodation, *Geosphere*, **14**: 1544–1563.

Cornwell, D.G., Mackenzie, G.D., England, R.W., Maguire, P.K.H., Lakemaryam Asfaw and Befekadu Oluma (2006). Northern main Ethiopian rift crustal structure from new high-precision gravity data, *Geol. Soci. Special Publ*. **259**: 307–321.

Cornwell, D., Maguire, P., England, R. and Stuart, G. (2010). Imaging detailed crustal structure and magmatic intrusion across the Ethiopian Rift using a dense linear broadband array, retrieved from http://dx.doi:10.1029/2009GC002637 on 20.11.2019.

Corti, G., Manetti, P., Tsegaye Abebe, Bonini, M., and Mazzarini, F. (2003). The volcano-tectonic activity of the main Ethiopian rift (East Africa): insights into the evolution of continental rifting, *Acta Vulcanologica*, **17**: 134-144

Corti, G. (2009). Continental rift evolution: from rift initiation to incipient break-up in the Main Ethiopian Rift. *East Afr. Earth Sci.* **96**:1–53.

Corti, G., Sani, F., Minissale, A. and Montanari, D. (2014). Volcano-tectonic and hydrothermal activity in the soddo area. **In:** *proceedings of the 5th African rift geothermal conf.* pp. 231-235, Arusha, Tanzania.

Corti, G., Sani, F., Agostini, S., Philippon, M., Sokoutis, D. and Willingshofer, E. (2018). off-axis volcano-tectonic activity during continental rifting: Insights from the transversal Goba-Bonga lineament, Main Ethiopian Rift, *Tectonophysics*, **729**: 75–91.

Daly, E., Keir, D., Ebinger, C. J., Stuart, G. W., Bastow, I. D., and Atalay Ayele (2008). Crustal tomographic imaging of a transitional continental rift: The Ethiopian rift, *Geophys. J. Int*. **172**:1033–1048.

Dentith, M. and Mudge, S. (2014). *Geophysics for the Mineral Exploration Geoscientist.* Cambridge university press, New York, 426 pp.

Di Paola, G.M. (1972). The Ethiopian Rift Valley (between 7^0 and 8^0 40' lat. North). *Bulletin of Volcanology*, **36**: 517–560.

Dugda M. T., Nyblade A. A., Julia J., Langston C. A., Ammon C. J., and Simiyu S. (2005). Crustal Structure in Ethiopia and Kenya from Receiver Function Analysis, *J. Geophys, Research, B, Solid Earth and Planets*, **110**: 1303-1339.

Dugda, M., Nyblade, A.A., and Julia, J. (2007). Thin lithosphere beneath the Ethiopian Plateau revealed by a joint inversion of Rayleigh wave group velocities and receiver functions, retrieved from http://dx. doi:10.1029/2006JB004918 on 22.11.2019.

Ebinger C. J. and Casey M. (2001). Continental breakup in magmatic provinces: An Ethiopian example. *Geol.* **29**: 527-530.

Electric Power Research Institute (EPRI), (1978). Geothermal energy prospects for the next 50 years. Unpublished Special report (ER-611-SR), EPRI, Alto, California, 150pp.

Engdawork Admasu and Selamawit Worku (2015). Characterization of Quaternary Extensional Structures: Tulumoye Geothermal Prospect, Ethiopia. *GRC Transact.* **39**: 25-32.

Giday Woldegebrel, Aronson J. L., and Walter R. C. (1990) Geology, geochronology, and rift basin development in the central sector of the Main Ethiopia Rift, *Geol. Society of America Bulletin* **102**: 439-458.

Greenfield, T., Keir, D., Kendall, J.M. and Atalay Ayele (2019). Seismicity of the Bora-Tulumoye volcanic field, 2016– 2017, *Geochem. Geophys. Geosyst.* **20**: 548–570.

Hayward, N.J. and Ebinger, C. J. (1996). Variations in the along-axis segmentation of the Afar Rift system. *Tectonics*, **15**: 244-257.

Hinze, W.J., von Frese, R.R. and Saad, A.H. (2013). *Gravity and Magnetic Exploration: Principles, Practices, and Applications,* Cambridge University Press, New York, 550 pp.

Hirt, C., Claessens, S.J. Fecher, T., Kuhun, M., Pail, R. and Rxer, M. (2013). New ultra high resolution picture of Earth's gravity field, *Geophysical research letter*, **140**: 4279-4283.

Hochstein, M.P. (1990). *Classification and assessment of geothermal resources*. Geothermal institute, University of Auckland, New Zealand, 155 pp.

Hoffman, C., Courtillot, V., Féraud, G., Rochette, P., Gezahegn Yirgu, Ketefo, E. and Pik, R. (1997). Timing of the Ethiopian basalt event and implications for plume birth and global change, *Nature*, **389**: 838–841.

Hutchison, W.A., Mother, T.A., Pyle, D.M., Biggs, J. and Gezahegn Yirgu (2015). Structural controls on fluid pathways in an active rift system: A case study of the Aluto volcanic complex, *Geosphere*, **11:** 1-21.

Jacobsen, B.H., (1987). A case for upward continuation as a standard separation filter for potential-field maps. *Geophysics,* **52**:1138–1148.

Kazmin, V., Seifemichael Berhe, Nicoletti, M. and Petrucciani, C. (1980). Evolution of the northern part of the Ethiopian Rift. *Accad.* **47**: 275–291.

Kearey, P. Brooks. M. and Hill, I. (2002). *An Introduction to Geophysical Exploration*, 3rd ed., Blackwell Science Ltd. Britain, 257 pp.

Keir, D., Kendall, J. M. and Ebinger, C., (2005). Variations in late syn-rift melt alignment inferred from shear-wave splitting in crustal earthquakes beneath the Ethiopian rift, retrieved from http://dx.doi.org/10.1029/2005GL024150 on 10.03.2020.

Keir, D., Ebinger, C.J., Stuart, G.W., Daly, E. and Atalay Ayele (2006). Strain accommodation by magmatism and faulting as rifting proceeds to breakup: seismicity of the northern Ethiopian rift, retrieved from http://dx.doi.org/10.1029/2005JB003748 on 06.02. 2020.

Keir, D., Pagli, C., Bastow, I. D., and Atalay Ayele (2011a). The magma-assisted removal of Arabia in Afar: Evidence from dike injection in the Ethiopian Rift captured using InSAR and seismicity, retrieved from http://dx.doi:10.1029/2010TC002785 on 08.02. 2020.

Keir, D., Manahloh Belachew, Ebinger, C. J., Kendall, J.M., Hammond, J. O. S., Stuart, G., Atalay Ayele and Rowland, J. V. (2011b). Mapping the evolving strain field during continental breakup from crustal anisotropy in the Afar Depression, retrieved from http://dx.doi:10.1038/ncomms1287 on 08.03.2020.

Kendall, J.M., Pilidou, S., Keir, D., Bastow, I.D., Stuart, G.W. and Atalay Ayele (2006). Mantle upwelling, melt migration, and the rifting of Africa: insights from seismic anisotropy, *Geol. Society Special Publ*. **259**: 55-72.

Keranen, K., Klemperer S. L., Gloaguen R. and the EAGLE working group (2004). Three dimensional seismic imaging of a protoridge axis in the Main Ethiopian rift, *Geol.* **32**:949-952.

Keranen, K., Klemperer, S.L., Julia, J., Lawrence, J.L. and Nyblade, A. (2009). Low lower-crustal Velocity across Ethiopia: Is the Main Ethiopian Rift a narrow rift in a hot craton?, retrieved from http://dx.doi.org/10.1029/2008GC002293 on 11.03.2019.

Kieffer, B., Arndt, N., LaPierre, H., Bastien, F., Bosch, D., Pecher, A., Gezahegn Yirgu, Dereje Ayalew, Weis, D., Jerram, D., Keller, F. and Meugniot, C. (2004). Flood and shield basalts from Ethiopia: Magmas from the African Superswell, *J. Petrology* **45**: 793–834.

Kurz, T., Gloaguen, R., Ebinger, C., Casey, M. and Bekele Abebe (2007). Deformation distribution and type in the Main Ethiopian Rift: A remote sensing study, *J. Afr. Earth* Sci. **48**: 100-114.

Lavayssière, A., Rychert, C., Harmon, H., Keir, D., James O., Hammond, J., Kendall, J., Doubre, C., and Leroy., S. (2018). Imaging lithospheric discontinuities beneath the northern East African Rift using S-to-P receiver functions, retrieved from http://dx. doi: 10.1029/2018GC007463 on 09.10 2019. .

Lavayssière A. (2019). Interactions between tectonic and magmatic processes in the East African Rift. Doctoral Dissertation, Southampton University, Southampton, England, 167 pp.

Lingerew Nebere (2017). Reduction to the pole and analytic signal interpretation technique of magnetic data in equatorial area, Ethiopia. International journal of scientific Engineering and research, **5**: 466-468.

Lowrie, W. (2007). *Fundamentals of Geophysics*. 2nd ed., Cambridge University Press, New York, 357 pp.

Mackenzie G., Thybo H., and Maguire P. (2005). Crustal velocity structure across the Main Ethiopian Rift: Results from 2-dimensional wide-angle seismic modeling, *Geophys. J. Int.* **162**: 996–1006.

Maguire, P.K.H., Ebinger, C.J., Stuart, G.W., Mackenzie, G.D., Whaler, K.A., Kendall, J.M., Khan, M.A., Fowler, C.M.R., Klemperer, S.L., Keller, G.R., Harder, S., Furman, T., Mickus, K., Lakemariam Asfaw, Atalay Ayele and Bekele Abebe (2003). Geophysical project in Ethiopia studies continental breakup, *American Geophysical Union*, **84**: 337–340.

Maguire, P.K.H., Keller, G.R., Klemperer, S.L., Mackenzie, G.D., Keranen, K., Harder, S., O'Reilly, B., Thybo, H., Lakemariam Asfaw, Khan, M.A. and Mulugeta Amha (2006). Crustal structure of the Northern Main Ethiopian Rift from the EAGLE controlled source survey: A snapshot of incipient lithospheric break-up, *Geol. Soc. Spec. Publ.* **84**: 337-340.

Martin-jones, C.M., Lane, C.S., Pearce, N.J.G., Smith, V.C., Lamb, H.F., Schaebitz, F., Viehberg, F., Brown, M.C., Frank U. and Asfawossen Asrat (2017). Lake sediments provide the first eruptive history for Corbetti, A high risk Main Ethiopian Rift volcano, *Geophysical research*, **45**: 1127-1130.

Mazzarini, F., Tsegaye Abebe, Innocent, F., Manetti, P. and Pareschi, M.T. (1999). Geology of the Debre Zeyt area (Ethiopia) (with a geological map at scale 1:100.000). *Acta Vulcanologica*, **11**: 131–141.

Mege, D., and Tesfaye Korme (2004). Dyke swarm emplacement in the Ethiopian Large Igneous Province: Not only a matter of stress. *Journal of Volcanology and Geothermal Research* **132**: 283–310.

Mehatsente R., Jentzsch G., and Jahr T. (1999). Crustal structure of the Main Ethiopian Rift from Gravity data: 3-dimensional modeling, *Tectonophysics,* **313**:363-382.

Meseret Teklemaryam and Kibret Beyene (2000). Geochemical monitoring of the Aluto-Langano Geothermal Field. Unpublished internal report, Geological Survey of Ethiopia, Addis Abeba, Ethiopia, 10pp.

Mickus, K., Ketsela Tadesse, Keller, G.R. and Befekadu Oluma (2007). Gravity analysis of the main Ethiopian rift, *J. Afr. Earth Sci.* **48**: 59–69.

Miller, H.G. and Singh, V. (1994). Potential field tilt-a new concept for location of potential field sources. *J. Appl. Geophys,* **32**: 213–217.

Mohr, P. (1962). The Ethiopian Rift System. *Bulletin of the Geophysical Observatory of Addis Ababa,* **5**:33-62.

Mohr, P. (1967). The Ethiopian Rift System. *Bulletin of the Geophysical Observatory of Addis Ababa,* **11**: 1–65.

Mohr P. (1971). Outline of tectonics of Ethiopia. *Tectonics of Africa,* **4**: 445- 458.

Mohr, P. and Zanettin, B. (1988). The Ethiopian flood basalt province. *Kluwer Academic Publishers,* **4***:* 63–110

Nafe J.E. and Drake C. L. (1957). Variation with depth in shallow and deep water marine sediments of porosity, density and the velocities of compressional and shear waves. *Geophysics*. ***22***: 523-552.

Pierrick, A. (2015). Gravimetry for geothermal exploration. Doctoral Dissertation, University of Neuchâtel, Switzerland, 223 pp.

Pizzi, A., Coltorti, M., Bekele Abebe, Disperati, L., Sacchi, G. and Salvini, R. (2006). The Wonji fault belt (main Ethiopian Rift): Structural and geomorphological constraints and GPS monitoring, *Geological Society Special Publication,* **259**:191–207.

Putri, D., Nanda, M., Rizal S., Idroes, R., and Ismail, N. (2019). Interpretation of gravity satellite data to delineate structural features connected to geothermal resources at Bur Ni Geureudong geothermal field, **In**: *proceedings of the 3rd International Conference on Natural and Environmental Sciences,* pp.6, Syiah Kuala, Indonesia.

Rajagopalan, S. (2003). Analytic Signal vs. Reduction to Pole: Solutions for Low Magnetic Latitudes. Retrieved from DOI: 10.1071/ASEG2003ab136 on 03.7.2020.

Reynolds, J.M. (1997). *An Introduction to Applied and Environmental Geophysics*. John Wiley and Sons Ltd, England, UK, 799 pp.

Rooney, T., Furman, T., Gezahegn Yirgu and Dereje Ayalew (2005). Structure of the Ethiopian lithosphere: Evidence from mantle Xenoliths, *Geochem. ET Cosmochimica Acta*, **69**: 3889–3910.

Rooney, T. (2006). Continental rifting in central Ethiopia: geochemical and isotopic constraints from lavas and xenoliths. Doctoral Dissertation, Pennsylvania State University, Pennsylvania, 158 pp.

Rooney, T., Furman, T., Bastow, I., Dereje Ayalew and Gezahegn Yirgu, (2007). Lithospheric modification during crustal extension in the Main Ethiopian Rift, *J. Geophys. Research* **112**: 10201-10222.

Samrock F., Grayver, A. V., Eysteinsson, H. and Saar, M. (2018). Magnetotelluric image of transcrustal magmatic system beneath the Tulumoye geothermal prospect in the Ethiopian Rift, *Geophys. Research Letters*, **45**: 847–855.

Soliva R, and Schultz R. A. (2008). Distributed and localized faulting in extensional settings: Insight from the North Ethiopian Rift–Afar transition area. Retrieved from http://dx.doi.org/10.1029/2007TC002148 on 07.04.2020.

Solomon Kebede (2016). Country update on geothermal exploration and development in Ethiopia. **In:** *Proceedings of the 6th African Rift Geothermal Conference* pp.1-15, Addis Ababa, Ethiopia.

Stuart, G.W., Bastow, I.D. And Ebinger, C. J. (2006). Crustal Structure of the northern Main Ethiopian Rift from receiver function studies, The Afar Volcanic Province within the East African Rift System, *Geol. Soc. Spec*. **259**:253–267.

Tadiwos Chernet, Hart, W. K., Aronson, J. L. and Walter, R. C. (1998). New age constraints on the timing of volcanism and tectonism in the northern main Ethiopian rift–southern Afar transition zone, Ethiopia, *Journal of Volcanology and Geothermal Research*, **80**: 267-280.

Tamiru Alemayahu and Tigistu Haile (2008). Geophysical exploration of Boku Geothermal area, central main Ethiopia rift. *Geothermic*s. **37**: 586-596**.**

Telford, W.S, Geldart, L.P. and Sheriff, R.E. (1990). *Applied Geophysics*, 2nd ed., Cambridge University Press, Cambridge, UK, 784 pp.

Tesfaye Korme, Chorowicz J, Collet B., and Bonavia F. (1997). Volcanic vents rooted on extension fractures and their geodynamic implications in the Ethiopian Rift, *J. Volcanol. Geotherm. Res*.**79**: 205-222.

Tesfaye Korme, Acocella, V., and Bekele Abebe (2004). The role of pre-existing structures in the origin, propagation and architecture of faults in the Main Ethiopian Rift, *Gondwana Research*, **7**: 467–479.

Tester, J.W., Drake, E.M., Driscol, M.J. and Peters, M.A. (2005). *Sustainable Energy Choosing Among Options*. 2nd ed. the MIT press, Cambridge, 500 pp.

Thompson D.T. (1982). A new technique for making computer-assisted depth estimates from magnetic data. *Geophysics*, **47**: 31–37.

Tiberi, C., Ebinger, C., Ballu, V., Stuart, G. and Befekadu Oluma (2005). Inverse models of gravity data from the Red Sea–Aden–East African rifts triple junction zone. *Geophysical Journal International*, **163**: 775–787.

Tigistu Haile and Tamiru Alemayahu (2012). The interference of a deep thermal system with a shallow aquifer: the case of Sodere and Gergedi thermal springs, Main Ethiopian Rift, Ethiopia, *Hydrogel.* **20**: 561-570.

Tilahun Mammo (2004). Mapping the crust-mantle boundary beneath the Afar depression. *Gondwana Research*, **7**: 855–861.

Tilahun Mammo (2010). Delineation of sub-basalt sedimentary basins in hydrocarbon exploration in North Ethiopia. *Marine and petroleum geology*, **27**: 895–908.

Tilahun Mammo (2013). Crustal Structure of the Flood Basalt Province of Ethiopia from Constrained 3-D Gravity Inversion. Retrieved from http://dx.doi10.1007/s00024-013-0663-0 on 11.10.2019.

Tsegaye Abebe, Manetti, P., Bonini, M., Corti, G., Innocenti, F., Mazzarini, F. and Pecskay, Z. (2005). Geological map (scale 1: 200,000) of the northern Main Ethiopian Rift and its implication for the volcano-tectonic evolution of the rift, *Geol. Soc. Am.* **821**: 51-97.

Tsegaye Abebe (2014). The occurrence of a complete continental rift type of volcanic rocks suite along the Yerer–Tullu Wellel Volcano Tectonic Lineament, Central Ethiopia. *J. Afr. Earth Sci.*, **99**: 374-385.

Whaler, K. A., and Hautot, S. (2006). The electrical resistivity structure of the crust beneath the northern Main Ethiopian Rift. *Geol. Society Special Publ*. **259**: 293–305.

Williams, C.F., Reed, M.J. and Anderson, A.F. (2011). Updating the classification of geothermal resources. **In**: *Proceedings in the 36th Workshop on Geothermal Reservoir Engineering*, pp 1-12, Stanford, California.

Wolfenden, E. (2003). Evolution of the southern Red Sea Rift: Birth of a magmatic margin. PhD thesis, Royal Holloway, University of London, UK, 150 pp.

Wolfenden, E., Ebinger, C., Gezahegn Yirgu, Deino, A. and Dereje Ayalew (2004). Evolution of the northern Main Ethiopian rift: birth of a triple junction, *Earth and Planetary Science Letters*, **224**: 213–228.

Yaogauo, L., and Oldenberg, D.W. (2001). Stable reduction to the pole at the magnetic equator. *Geophysics*. 66: 571-578.

Zanettin, B., Justin-Visentin, E., Nicoletti, M. and Piccirillo, E.M. (1980). Correlations among Ethiopian volcanic formations with special references to the chronological and stratigraphical problems of the Trap Series, *Atti Convegni Lincei*, **47:**252-257.

APPENDIXES

Appendix A Magnetic survey data from Geological survey of Ethiopia

Date									
NP17	2/12/2012								
	Easting	Northing	Elevation	Dial Reading	Time	hr.	min.		Corr.Dial Reading
Bsi1		926372	1656	35064	8:40	0	40	40	35064
	514990	928493	1593	35130	9:35	1	35	95	35105.21
	516998	928495	1633	35182	10:11	2	11	131	35140.98
	517253	928518	1636	35131	10:15	2	15	135	35088.17
	517497	928499	1643	35127	10:20	2	20	140	35081.92
Bf1	516082	926372	1661	35119	10:42	2	42	162	35064
Date	3/12/2012								
Np16									
Bi2	524474	934534	1545	35639	8:18	0	18	18	35639
	524611	934929	1542	35565	8:39	0	39	39	35550.84
	524753	934972	1543	35421	8:42	0	42	42	35404.81
	526822	935164	1577	35595	10:17	2	17	137	35514.73
	527268	935101	1591	35819	10:33	2	33	153	35727.94
Bf2	524473	934536	1556	35753	11:07	3	7	187	35639.01
Date	4/12/2012								
NP16									
Bi2	524511	934534	1547	35571	7:05	0	5	5	35571
	530503	935016	1601	35588	9:10	2	10	130	35480.71
	530754	935063	1661	35459	9:22	2	22	142	35341.41
	530989	935011	1711	35502	9:32	2	32	152	35375.83
Bf2	524486	934538	1545	35777	11:05	4	5	245	35571.01
Date	5/12/2012								
NP14									
Bi2	524467	934553	1538	35705	7:40	0	40	40	35705
	527252	932984	1540	35364	9:57	2	57	177	35295.5
	527497	932988	1540	35334	10:03	3	3	183	35262.5
	527752	932995	1540	35313	10:13	3	13	193	35236.5
	528006	932940	1540	35350	10:18	3	18	198	35271
	528259	933001	1543	35402	10:28	3	28	208	35318
	528513	933004	1540	35460	10:31	3	31	211	35374.5
	528769	933010	1543	35491	10:36	3	36	216	35403
	529001	932957	1542	35567	10:41	3	41	221	35476.5
Bf2	524482	934537	1552	35803	10:56	3	56	236	35705
Date	6/12/2012								
NP12									

Bi2	524483	934533	1612	35713	7:12	0	12	12	35713
	529320	930987	1542	35380	9:47	2	47	167	35349
	529541	930849	1543	35364	10:02	3	2	182	35330
	529803	930920	1542	35357	10:20	3	20	200	35319.4
	530054	930890	1540	35365	10:25	3	25	205	35326.4
Bf2	524491	934535	1543	35760	11:07	4	7	247	35713
Date	7/12/2012								
NP11									
Bi2	524477	934521	1583	35727	7:13	0	13	13	35727
	530104	929479	1543	35475	9:46	2	46	166	35414.37
	530399	929487	1543	35438	9:52	2	52	172	35374.99
	530755	929522	1542	35542	9:57	2	57	177	35477.01
	530871	929741	1542	35536	10:02	3	2	182	35469.03
	531004	929954	1543	35654	10:16	3	16	196	35581.48
Bf2	524484	934533	1547	35813	10:50	3	50	230	35727
Date	8/12/2012								
NP10									
Bi2	524487	934541	1542	35737	7:11	0	11	11	35737
	529203	928939	1543	35391	9:03	2	3	123	35341.35
	529447	928945	1541	35390	9:06	2	6	126	35339.02
	529696	928952	1543	35367	9:22	2	22	142	35308.93
	529953	928960	1541	35386	9:26	2	26	146	35326.15
	520197	928963	1543	35431	9:30	2	30	150	35369.38
	520450	928972	1547	35405	9:33	2	33	153	35342.05
	530704	928986	1540	35384	9:37	2	37	157	35319.28
	530993	928990	1535	35367	9:42	2	42	162	35300.06
	531312	929002	1541	35384	9:48	2	48	168	35314.4
	531624	929016	1544	35435	9:52	2	52	172	35363.63
Bf2	524493	934538	1560	35823	10:25	3	25	205	35737
Date	9/12/2012								
NP9									
Bi2	524487	934528	1565	35760	7:09	0	9	9	35760
	529412	927926	1542	35347	9:21	2	21	141	35324.48
	529658	927933	1540	35328	9:25	2	25	145	35304.8
	529905	927931	1538	35331	9:41	2	41	161	35305.07
	530213	927953	1541	35460	9:45	2	45	165	35433.39
	520199	927945	1543	35739	9:49	2	49	169	35711.7
Bf2	524484	934545	1566	35796	10:40	3	40	220	35760
Date	10/12/2012								
NP8									
Bi2	524486	934538	1538	35734	7:10	0	10	10	35734

	530302	926940	1542	35390	10:20	3	20	200	35344.44
	530551	926947	1541	35338	10:21	3	21	201	35292.2
	530810	926957	1541	35335	10:24	3	24	204	35288.48
	531116	926967	1540	35465	10:27	3	27	207	35417.76
Bf2	524472	934538	1549	35787	10:51	3	51	231	35734
Date	11/12/2012								
NP5									
Bi2	524485	934527	1563	35740	7:07	0	7	7	35740
	526006	924010	1541	35036	8:15	1	15	75	35029.18
	525749	923939	1547	35118	8:19	1	19	79	35110.78
	525485	923801	1556	35158	8:24	1	24	84	35150.28
	525241	923744	1564	35164	8:29	1	29	89	35155.78
Bf2	524485	934527	1563	35774	1:46	5	46	346	35740
Date	12/12/2012								
NP5									
Bi2	524482	934517	1542	35748	7:19	0	19	19	35748
	526002	923997	1546	35046	7:56	0	56	56	35028.76
	530017	924152	1564	35499	9:07	2	7	127	35448.67
	530268	924111	1565	35491	9:12	2	12	132	35438.34
	530515	924115	1566	35504	9:16	2	16	136	35449.48
	530775	924116	1559	35489	9:21	2	21	141	35432.15
	531003	924002	1564	35521	9:28	2	28	148	35460.89
Bf2	524466	934538	1547	35837	10:30	3	30	210	35747.99
Date	13/12/2012								
NP6									
Bi2	524482	934517	1542	35725	7:19	0	19	19	35725
	529859	925401	1541	35410	10:22	3	22	202	35357.24
	530139	925411	1541	35423	10:24	3	24	204	35369.66
	530305	925177	1535	35493	10:49	3	49	229	35432.46
	530523	924977	1549	35549	10:56	3	56	236	35486.44
	530793	925014	1552	35314	11:00	4	0	240	35250.29
	530960	925030	1553	35516	11:03	4	3	243	35451.42
Bf2	524482	934517	1542	35806	12:00	5	0	300	35724.99
Date	16/12/2012								
NP5									
Bi3	516261	926726	1656	35732	7:45	0	45	45	35732
	514993	923985	1690	35199	8:42	1	42	102	35477.38

Appendix B Gravity data from the International Gravity Bureau

Easting	Northing	Longitude	Latitude	Elevation	Free air correction	Bouguer correction	Simple B anomaly	Complete B anomaly

560460.91	943000.07	39.5485	8.5295004	1429.24	0.85	-6.076	-167.372	-166.518
560462.33	942005.13	39.5485	8.5205004	1440.49	1.27	11.934	-150.627	-149.358
560463.74	941010.18	39.5485	8.5115004	1301.51	0.94	-26.617	-173.558	-172.616
560465.15	940015.24	39.5485	8.5025004	1295.05	0.53	-28.573	-174.788	-174.261
560466.55	939020.3	39.5485	8.4935004	1298.1	0.37	-33.295	-179.852	-179.478
560467.96	938025.35	39.5485	8.4845004	1386.43	0.62	-21.2	-177.686	-177.067
560469.36	937030.41	39.5485	8.4755004	1310.87	0.24	-35.081	-183.074	-182.833
560470.77	936035.47	39.5485	8.4665004	1322.2	0.25	-35.848	-185.115	-184.861
560472.17	935040.52	39.5485	8.4575004	1332.95	0.38	-37.294	-187.77	-187.389
560473.57	934045.58	39.5485	8.4485004	1369.9	0.33	-41.056	-195.685	-195.353
560474.97	933050.64	39.5485	8.4395004	1451.89	0.36	-21.718	-185.56	-185.196
560476.37	932055.7	39.5485	8.4305004	1461.56	0.24	-19.199	-184.127	-183.884
560477.76	931060.76	39.5485	8.4215004	1464.71	0.28	-23.392	-188.673	-188.393
560479.16	930065.82	39.5485	8.4125004	1519.35	0.23	-23.795	-195.213	-194.987
560480.55	929070.88	39.5485	8.4035004	1512	0.24	-23.029	-193.621	-193.385
560481.94	928075.94	39.5485	8.3945004	1543.77	0.27	-36.19	-210.35	-210.077
560483.33	927081	39.5485	8.3855004	1560.54	0.38	-27.581	-203.623	-203.244
560484.72	926086.06	39.5485	8.3765004	1587.19	0.7	-25.923	-204.957	-204.252
560486.11	925091.13	39.5485	8.3675004	1634.75	1.51	-30.012	-214.383	-212.874
560487.49	924096.19	39.5485	8.3585004	1773	1.76	-24.315	-224.192	-222.43
560488.88	923101.25	39.5485	8.3495004	1929.43	1.47	17.991	-199.414	-197.94
560490.26	922106.32	39.5485	8.3405004	1919.5	0.85	9.36	-206.933	-206.079
560491.64	921111.38	39.5485	8.3315004	2000.69	1.01	14.148	-211.237	-210.225
560493.02	920116.45	39.5485	8.3225004	2091.75	1.41	40.981	-194.594	-193.186
560494.4	919121.51	39.5485	8.3135004	2024.29	0.97	13.095	-214.931	-213.958
560495.77	918126.58	39.5485	8.3045004	2095.73	1.35	22.273	-213.747	-212.393
560497.15	917131.64	39.5485	8.2955004	2111.8	2.62	1.964	-235.854	-233.238
560498.52	916136.71	39.5485	8.2865004	2379.21	3.35	55.717	-211.99	-208.638
560499.89	915141.78	39.5485	8.2775004	2187.2	2.77	12.195	-234.056	-231.285
560501.27	914146.84	39.5485	8.2685004	2338.98	1.7	30.765	-232.45	-230.749
560502.63	913151.91	39.5485	8.2595004	2484.1	0.82	69.979	-209.439	-208.618
560504	912156.98	39.5485	8.2505004	2461.93	0.36	75.568	-201.376	-201.019
560505.37	911162.05	39.5485	8.2415004	2462.93	0.19	63.207	-213.848	-213.658
560506.73	910167.12	39.5485	8.2325004	2483.5	0.17	72.585	-206.766	-206.594
560508.1	909172.19	39.5485	8.2235004	2436.9	0.2	56.834	-217.316	-217.115
560509.46	908177.26	39.5485	8.2145004	2452.83	0.14	67.079	-208.848	-208.711
560510.82	907182.33	39.5485	8.2055004	2482.27	0.08	74.994	-204.22	-204.144
560512.18	906187.4	39.5485	8.1965004	2475.58	0.16	57.858	-220.609	-220.449
560513.54	905192.47	39.5485	8.1875004	2506.35	0.18	66.182	-215.719	-215.542
560514.89	904197.54	39.5485	8.1785004	2570.19	0.15	78.212	-210.812	-210.664
560516.25	903202.61	39.5485	8.1695004	2579.96	0.1	74.255	-215.858	-215.755

560517.6	902207.69	39.5485	8.1605004	2568.07	0.13	73.114	-215.673	-215.538
560518.95	901212.76	39.5485	8.1515004	2598.2	0.14	80.04	-212.108	-211.967
560520.3	900217.83	39.5485	8.1425004	2626.4	0.1	83.27	-212.023	-211.925
560521.65	899222.91	39.5485	8.1335004	2641.01	0.11	81.506	-215.416	-215.308
560523	898227.98	39.5485	8.1245004	2675	0.14	85.922	-214.789	-214.648
560524.34	897233.06	39.5485	8.1155004	2695.9	0.21	83.798	-219.242	-219.035
560525.69	896238.13	39.5485	8.1065004	2745.92	0.19	89.061	-219.553	-219.362
560527.03	895243.21	39.5485	8.0975004	2756.4	0.11	88.921	-220.861	-220.749
560528.37	894248.28	39.5485	8.0885004	2752.81	0.13	88.24	-221.142	-221.015
560529.71	893253.36	39.5485	8.0795004	2750.63	0.21	87.493	-221.646	-221.437
560531.05	892258.44	39.5485	8.0705004	2741.67	0.72	84.253	-223.887	-223.166
560532.38	891263.51	39.5485	8.0615004	2912.4	1.77	122.265	-204.889	-203.118
560533.72	890268.59	39.5485	8.0525004	2818.05	0.39	91.674	-224.975	-224.582
560535.05	889273.67	39.5485	8.0435004	2821.8	0.37	95.957	-221.11	-220.742
560536.38	888278.75	39.5485	8.0345004	2810.6	0.46	86.725	-229.095	-228.633
560537.71	887283.83	39.5485	8.0255004	2806.93	0.76	99.517	-215.894	-215.131
560539.04	886288.91	39.5485	8.0165004	2740.09	1.07	84.214	-223.75	-222.678
560540.37	885293.99	39.5485	8.0075004	2726	0.9	82.99	-223.405	-222.505
561441.36	949966.13	39.5575	8.5925004	1360.25	0.65	-5.737	-159.281	-158.629
561442.8	948971.18	39.5575	8.5835004	1359.95	0.55	-6.79	-160.301	-159.75
561444.25	947976.23	39.5575	8.5745004	1363.25	0.67	-10.633	-164.514	-163.843
561445.69	946981.28	39.5575	8.5655004	1450.2	0.79	2.239	-161.413	-160.623
561447.13	945986.34	39.5575	8.5565004	1478.15	1.21	11.603	-155.188	-153.98
561448.57	944991.39	39.5575	8.5475004	1316.25	1.63	-17.12	-165.718	-164.086
561450.01	943996.44	39.5575	8.5385004	1334	0.97	-9.204	-159.798	-158.832
561451.45	943001.49	39.5575	8.5295004	1354.75	0.81	-5.863	-158.789	-157.975
561452.88	942006.55	39.5575	8.5205004	1310.85	0.76	-20.172	-168.163	-167.403
561454.32	941011.6	39.5575	8.5115004	1278.55	0.49	-29.502	-173.861	-173.376
561455.75	940016.65	39.5575	8.5025004	1261.75	0.32	-35.55	-178.019	-177.697
561457.18	939021.71	39.5575	8.4935004	1275.95	0.23	-36.73	-180.797	-180.562
561458.61	938026.76	39.5575	8.4845004	1278.4	0.25	-38.737	-183.079	-182.828
561460.04	937031.82	39.5575	8.4755004	1296.55	0.14	-38.2	-184.583	-184.445
561461.46	936036.87	39.5575	8.4665004	1306.7	0.15	-39.531	-187.055	-186.902